A Precise Measurement of $\Gamma_{Z^0 \rightarrow b\bar{b}} / \Gamma_{Z^0 \rightarrow hadrons}$

Anna Margaret Stacey
Imperial College, London
November 1996

A thesis submitted for the degree of
Doctor of Philosophy
of the University of London
and the
Diploma of Imperial College

Abstract

The ratio $R_b = \Gamma_{Z^0 \to b\bar{b}} / \Gamma_{Z^0 \to hadrons}$ has been measured using about 3.8 million hadronic Z^0 decays recorded by the ALEPH detector at LEP during the period 1992-95. A new high-purity b-tag was developed, relying on both the large impact parameters of tracks from B hadrons and on the large mass of the b quark compared to the c quark. A new primary vertex finder reduced systematic uncertainty due to hemisphere-hemisphere correlation in tagging efficiency. Improved understanding of the silicon vertex detector efficiency and its simulation in the Monte Carlo helped to reduce systematic errors due to uncertainties in the detector simulation.

With the aid of these developments, the value of $\Gamma_{Z^0 \to b\bar{b}} / \Gamma_{Z^0 \to hadrons}$ was measured to be:

$$R_b = (21.72 \pm 0.11(stat.) \pm 0.17(syst.) - 0.037[R_c - 17.1])\,\%\,.$$

This is compared to the Standard Model prediction of $R_b = 21.58\,\%$ and to other recent experimental results.

Acknowledgements

I am grateful to my supervisor, Jordan Nash, for his help and for being there to give me advice and to sign endless forms. I would also like to thank Prof. Peter Dornan for the opportunity of working in the group, for his help and support and for suggesting I work on R_b in the first place.

When I started at IC, I was lucky to be working on the VDET upgrade project with Nikos (who introduced me to ALEPH and later terrified me with his demonstrations of authentic Greek driving), Geoff, Dave and Dave. Then when I began my analysis, I was lucky again to find the ALEPH R_b group — Duccio (who took me ski-ing, coped with my panic attacks and was always there to help), Lorenzo (who helped me get started on the project and patiently looked at my plots), Ian (who answered all my questions and laughed at my jokes), Fabrizio, Andrew and Jack. I also got to meet Manoj, who forgave me for mispronouncing his name and spent ages introducing me to the mysteries of the VDET simulation, Gary, Stefan, Alain and Francesco. It was great fun to work with all these people.

In the course of carrying out my ITC duties, Bill, Ann and Marco taught me the idiosyncracies of that unique chamber. Ann kindly responded to my pleas for help even when she was trying to write up her thesis and Bill made sure I never felt abandoned. Life in CERN wasn't all work though — Mike, Andy, Matt, Ed, Lizzie, Dave and Jane all ensured there was plenty to distract me (usually ski-ing). Many thanks to Ainsley on that front too, as well as for always being around for an ice-cream or an extended chat.

Back at IC, Jo refused to let me shirk my duties to the coffee industry (how will they survive now you're in Hamburg, Jo?), Luciano expanded my linguistic skills and Pete, Gav, Nikolai and Peter M. put up with my terminal scrounging habits. Thanks also to Barry for his unique outlook on life, to Alex for introducing me to Zed and Bunjy's and to Nevin, Suzy and Phil for being great office-mates.

Special thanks should go to my flatmates, Jo, Kate and Eleanor, for putting up with my stress and responding in kind, to Rajiv for all those emails and for being a great friend, to Nadine for always being understanding, to Debs for a lot of fun times and to all my other friends.

I owe a lot of thanks to everybody who helped me by proof-reading this thesis and answering my questions — Jordan, Duccio, Peter, Bill, Ian, Ann, Rajiv, Manoj, Alain, Gerret and Mark. Any mistakes which remain are all mine!

Finally, I would like to thank Tony and my family for their love and support and for helping me get through this writing-up period with my sanity still (mainly) intact. This thesis is dedicated to them.

Contents

List of Figures

List of Tables

Introduction

In the ratio $R_b = \Gamma_{Z^0 \to b\bar{b}} / \Gamma_{Z^0 \to hadrons}$, the fraction of hadronic Z^0 decays to b quarks, most electroweak and QCD corrections to the partial widths cancel. This means that R_b is relatively unaffected by the strong coupling constant, α_s, or by the mass of the Higgs boson. At the same time, it is sensitive to the mass of the top quark through the large coupling of top to the b quarks. It would also be affected by new physics that coupled preferentially to b quarks.

In 1995, the average value of R_b measured by the LEP experiments and SLD [1] was (22.05±0.16) %, assuming the Standard Model value for R_c. This differed by 3.1σ from the Standard Model prediction of 21.56 % [2]. Figure 0.1 shows the measurements at the time of the 1995 summer conferences. Because of the large discrepancy between the predicted and observed values of R_b, there was much interest and effort invested in updating the measurements for the 1996 summer conferences, to confirm or deny the deviation from the Standard Model.

The work presented in this thesis covers one of two ALEPH R_b analyses contributed to the 1996 ICHEP conference in Warsaw as preliminary results [3,4]. It was developed by a small team at CERN, in which the author played an integral part. Her particular contribution focussed on the study of uncertainties in the accuracy with which tracking, in particular the silicon vertex detector, was simulated in the Monte Carlo. As part of this study she uncovered a fault in the algorithm used to process the data collected in 1993 and worked on improving the Monte Carlo simulation of vertex detector efficiency for the 1994 production. She also worked on the correction of Monte Carlo so that it more accurately reflected the tracking resolution and efficiency of the data. As part of this, she studied the possibility of applying corrections to Monte Carlo tracks before reconstructing the primary vertex.

As a member of ALEPH, the author contributed towards the operation of the detector by taking part in data-collecting shifts and the running of the inner tracking chamber (ITC). In addition, she was involved in the upgrade of the silicon vertex

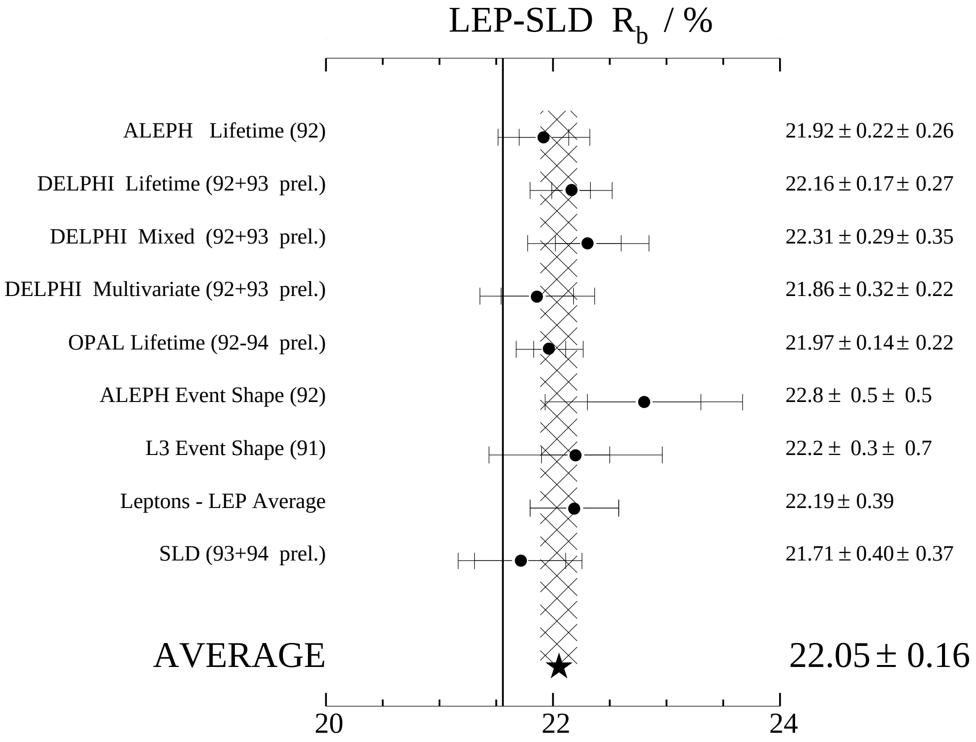

Figure 0.1: *Measurements of R_b (dark circles) at the time of the 1995 summer conferences, including some preliminary measurements. The world average is marked by a star and the shaded area shows the region within one standard deviation of the average. The vertical line indicates the Standard Model prediction. Where two errors are given, the first is statistical and the second systematic. R_c has been fixed to the value predicted by the Standard Model.*

detector, beginning with her participation in the first beam test at CERN. At Imperial College, she developed algorithms for automating part of the assembly procedure for detector modules. She co-operated in the design, implementation and operation of a laser testing station for completed modules. In particular, she was responsible for the LabView program which made up the Macintosh component of the station.

Chapter 1 of this thesis gives the theoretical background to the work presented. A brief overview of the Standard Model leads to a discussion of the role of R_b in making precision tests of electroweak physics. In Chapter 2, the experimental apparatus is described, with emphasis on the aspect most important for the work presented here, the tracking system. Chapter 3 describes the most relevant component of the tracking system, the silicon vertex detector (VDET). The simulation of the vertex detector in Monte Carlo, which has a significant impact on the systematic uncertainty in the measurement of R_b, is discussed. The project to upgrade the vertex detector is also described in Chapter 3. The new VDET was installed in October 1995, in time for the increase in LEP energy. Compared to the first vertex detector, it provides increased angular coverage, increased radiation tolerance and a more uniform distribution of material. Much of the design and testing of the new VDET took place at Imperial College, and some of this process is described.

In Chapter 4, the double tag method used for measuring R_b is described. This method eliminates the greatest potential systematic uncertainty in the measurement, by removing the need to predict the absolute efficiency for tagging b events from the Monte Carlo. The remaining sources of uncertainty in the method, in particular the need to predict the backgrounds and the hemisphere-hemisphere correlation of tagging efficiency are discussed. Finally, the hemisphere-hemisphere correlation, the source of one of the largest systematic uncertainties in the measurement, is described in more detail.

Chapter 5 sets out the method used to tag b events. This is a new method, developed for the analysis presented here with the aim of reducing the effects of charm background and hemisphere-hemisphere correlation on R_b. To obtain very high purities, it combines the established ALEPH impact parameter tag with a new tag, based on the high invariant mass of B hadrons. To reduce the uncertainties introduced by the correlation, one of its main sources — a primary vertex shared by the two hemispheres — was eliminated. Two separate primary vertices were reconstructed for every event, one in each hemisphere, significantly reducing the systematic error in the measurement of R_b due to uncertainties in the size of the correlation.

Chapter 6 gives the result of the analysis: a measurement of R_b with a relative precision of 0.9%. In Chapter 7, the estimation of systematic errors in the measurement is discussed. The most significant of these arise from uncertainties in the simulation of tracking and uncertainties in the prediction of the correlation. Finally, Chapter 8 compares the result to the Standard Model prediction, other measurements and the new world average from the 1996 summer conferences.

Chapter 1

Theoretical overview

Over the past 60 years, a series of experimental and theoretical discoveries has led to the Standard Model of particle physics. To date, it has been able to survive all of the tests made of it.

This chapter outlines the theoretical background to the measurement of R_b. Section 1.1 describes the central themes of the Standard Model, with emphasis on those aspects most relevant to R_b. More complete and detailed explanations can be found in references such as [5–8]. Section 1.2 discusses the motivation behind precision tests of the Standard Model. It describes how the measurement of R_b can be used to probe the Standard Model and to place constraints on the theories proposed for its extension.

1.1 The Standard Model

1.1.1 Forces and matter

The Standard Model of particle physics uses quantum field theories to describe three of the four forces by which fundamental particles interact. The most familiar of these forces, gravity, is not included. A consistent quantum theory of gravity does not yet exist, but it is by far the weakest of the four and has negligible effect at the subatomic scale. The other forces are the electromagnetic, strong and weak forces.

The theory of electromagnetism was first formulated by Maxwell. All electrically charged particles act as sources of electromagnetic fields, which hold electrons and nuclei together to form atoms and atoms together in larger structures. The application of relativistic quantum mechanics to the electromagnetic field gave rise to Quantum

Electrodynamics, or QED [5]. This describes the interactions of electrically charged particles, mediated by a massless boson, the photon. It was the original quantum field theory.

The weak force is responsible for nuclear beta decay. It affects all particles and is short-range, being mediated by the massive vector bosons $W^{\pm}$ and Z^{0}. In the 1960's, Glashow, Salam and Weinberg showed that electromagnetism and the weak force were in fact two aspects of a single electroweak theory [8]. This symmetry is manifest at high energies where the masses of the $W^{\pm}$ and Z^{0} are negligible. The Higgs mechanism gives the bosons their masses and thus breaks the symmetry at low energies. It also predicts the existence of a further scalar particle, the Higgs boson, which has not yet been observed.

The strong force binds the constituent particles of the nucleons and holds the nucleus together. Particles experiencing the strong force are said to have a colour charge. Such particles interact via a massless boson, the gluon. However, unlike the photon, which is electrically neutral, the gluons themselves carry colour charge and can therefore interact with one another. The field theory which describes the strong interaction is Quantum Chromodynamics, or QCD [5].

Fundamental particles within the Standard Model are divided up into the spin-$\frac{1}{2}$ fermions which make up matter and the spin-1 bosons which mediate the fundamental forces. In addition, as mentioned above, the mechanism for electroweak symmetry breaking predicts a Higgs boson with spin 0. The Standard Model fermions are shown in Table 1.1. They are divided into two groups — the quarks, which have colour charge and interact via the strong force, and the leptons which do not. Both groups undergo electroweak interactions. Most familiar of the leptons is the electron (e). The up and down quarks (u and d) are the building blocks of protons and neutrons, which combine with electrons to make up atoms. The electron is accompanied by another lepton, the electron neutrino (ν_e). Neutrinos are massless, or very light, carry no electric or colour charge and interact only via the weak force.

Together, the u and d quarks, the electron and the electron neutrino form a generation of particles. There are two further generations, each made up of two quarks, a charged lepton and a neutrino. Each particle has identical quantum numbers to its partners in the other generations, apart from flavour (defining the generation to which it belongs) and mass (each generation being heavier than the last). In the second generation are the strange (s) and charm (c) quarks, the muon (μ) and the muon neutrino (ν_{μ}). Finally, the third generation contains the tau (τ) and the tau

Leptons		Quarks	
Particle	Charge/e	Particle	Charge/e
e	-1	u	$+\frac{2}{3}$
ν_e	0	d	$-\frac{1}{3}$
μ	-1	c	$+\frac{2}{3}$
ν_μ	0	s	$-\frac{1}{3}$
τ	-1	t	$+\frac{2}{3}$
ν_τ	0	b	$-\frac{1}{3}$

Table 1.1: *Matter units within the Standard Model. Charge is given in units of e, the magnitude of the charge carried by the electron.*

neutrino (ν_τ) along with the top (t) and bottom (b) quarks.

The Standard Model does not explain why there are three, and only three, generations. However, if any further generations contained a light or massless neutrino, it would be observed as part of the invisible width of the Z^0 — events which contribute to the observed width of the mass peak but cannot be detected. Measurements of the invisible width at LEP and SLC [9] suggest that there are 2.991 ± 0.016 generations with light neutrinos.

1.1.2 Perturbation theory

In QED, the strength of the interaction between two charged objects depends on the product of their charges (in units of e, the charge carried by the electron) and on the intrinsic strength of the force. This last quantity is

$$\alpha = \frac{e^2}{4\pi}\,, \tag{1.1}$$

the electromagnetic coupling constant. As throughout this thesis, natural units ($\hbar = c = 1$) and the Heaviside-Lorentz electromagnetic units ($\epsilon_0 = \mu_0 = 1$) have been used.

The particles in a quantum field theory interact through the exchange of field quanta — in the case of QED, the photon. The simplest such interaction is shown as a schematic picture in Figure 1.1 a, which is a Feynman diagram. The Feynman rules can be used to calculate the amplitude, $\mathcal{M}$, of any such diagram, from which the cross-

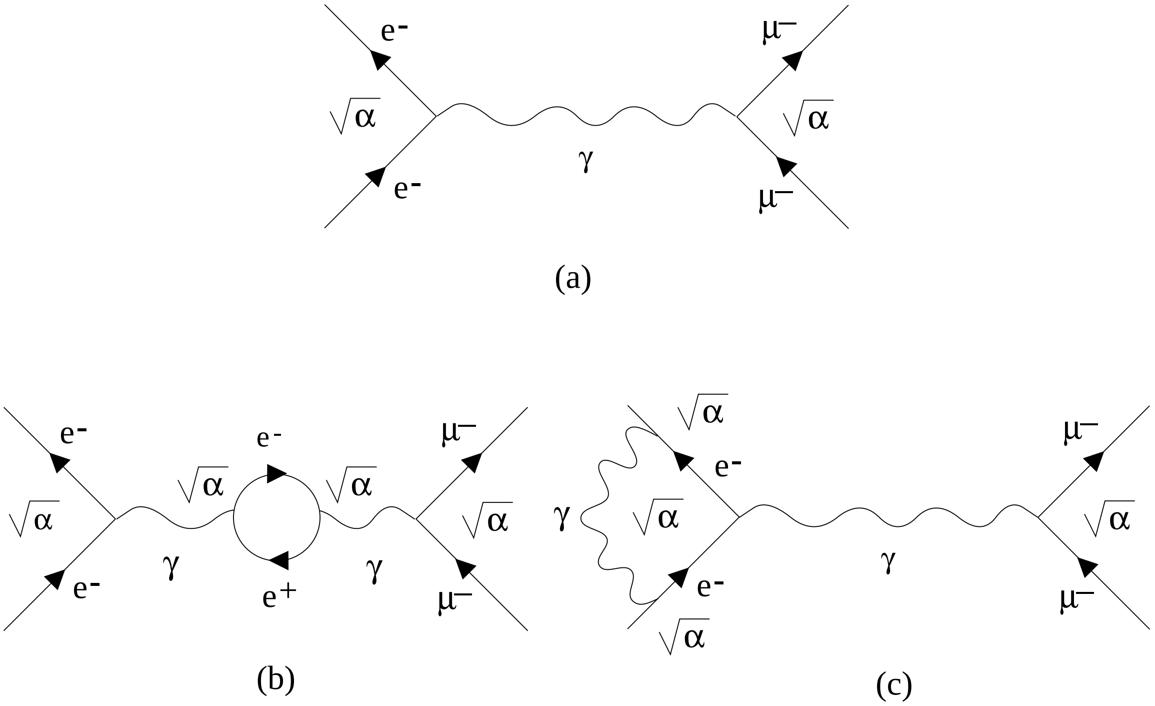

Figure 1.1: *Electromagnetic interaction between an electron and a muon (a) by exchange of a single photon (b) and (c) with 1-loop corrections.*

section for the interaction can be derived. In Figure 1.1 a, a factor $\sqrt{\alpha}$ is introduced into $\mathcal{M}$ at every vertex where a charged particle interacts with a photon. In other quantum field theories, similar diagrams represent the fundamental interactions, with coupling constants determined by the intrinsic strength of each force. Figure 1.1 b shows a correction to the simplest case, where the virtual photon disintegrates into an electron-positron pair which then annihilate to form a photon once more. This is an example of a loop diagram. Figure 1.1 c shows another loop correction, in which a photon is exchanged between the incoming and outgoing electrons.

In Figures 1.1 b and 1.1 c, the two extra vertices introduce a factor α into $\mathcal{M}$, compared to the simplest diagram. In fact, all of the diagrams whose contributions must be summed to give the total amplitude for the interaction can be arranged to form a power series in α. When the coupling constant is less than 1, as with QED and electroweak theory and in some circumstances with QCD, each power of α is smaller than the preceeding one. Hence, it appears that each term can be considered as a small correction to the series up to that point, the basis of perturbation theory.

Unfortunately, the amplitudes calculated for some of the loop diagrams turn out to be infinite. To deal with this, one must apply the technique of renormalization. Here, the loop corrections are split into infinite and finite parts. It turns out that for field theories with local gauge invariance, such as those within the Standard Model, the infinite parts of the corrections cancel to all orders in α.

Renormalization involves redefining the parameters of the theory, such as the charge and mass of an electron in QED. For example, to measure the charge on an electron, one would observe its behaviour in the presence of an electromagnetic field. Yet, since this behaviour is affected by loop corrections, it is impossible to observe the 'bare', uncorrected charge. After renormalization, the electric charge appearing in an expression for $\mathcal{M}$ is the one that is physically measured at low energy [6].

The finite parts of the corrections still remain. Some of these can be summed to all orders in α to give a finite, momentum-dependent correction to the effective coupling constant. In QED, this can be viewed as the result of a cloud of virtual electron-positron pairs created by processes such as Figure 1.1 b. The positrons in this cloud are attracted towards the electron, screening its charge. The measured charge then depends on the scale at which the electron and its cloud are probed. As the energy increases and the distance scale decreases, the observed charge increases. This variation with energy scale means that α is referred to as a running coupling constant.

After renormalization, calculations are based on an experimentally measured value of α, taken at some reference energy scale μ. It is clear that physical quantities, such as $\mathcal{M}$, should not depend on the value of μ. Thus, the dependence of $\mathcal{M}$ on μ must cancel the dependence of α on μ. This leads to the Renormalization Group Equation [6].

The theory of strong interactions, QCD, can be partly treated using perturbation theory. As with QED, the observed value of the coupling constant, α_s, depends on energy scale. However, gluon self-coupling causes α_s to *decrease* for small distances and high energies. This leads to the phenomena of asymptotic freedom and quark confinement at small and large distances respectively. For high-energy interactions, such as when quarks are probed inside a hadron, they can be treated almost as free particles and calculations can be made using perturbation theory. As the energy scale falls, α_s approaches and exceeds unity and perturbation theory no longer applies. Exact calculations are not possible in this non-perturbative region, where one instead relies on phenomenological models such as that described in Section 1.1.4.

1.1.3 The electroweak model

The electroweak model of Glashow, Salam and Weinberg is based on the group $SU(2)_L \times U(1)$. The underlying gauge fields are $W_i^\mu (i = 1, 2, 3)$ for the $SU(2)_L$ factor and B^μ for the $U(1)$ factor, with fundamental coupling constants g and g' respectively. The physical weak and electromagnetic vector bosons are expressed as linear combinations of these fields:

$$\begin{aligned} W^{\mu\pm} &= \frac{1}{\sqrt{2}}(W_1^\mu \mp iW_2^\mu) && (1.2) \\ Z^\mu &= W_3^\mu \cos\theta_W - B^\mu \sin\theta_W && (1.3) \\ A^\mu &= W_3^\mu \sin\theta_W + B^\mu \cos\theta_W && (1.4) \end{aligned}$$

respectively, where

$$\begin{aligned} \sin\theta_W &= \frac{g'}{\sqrt{g^2 + g'^2}} && (1.5) \\ \cos\theta_W &= \frac{g}{\sqrt{g^2 + g'^2}} . && (1.6) \end{aligned}$$

The Fermi constant for weak decay can be deduced:

$$G_F = \frac{\sqrt{2}g^2}{8M_W^2} . \tag{1.7}$$

The $W^\pm$ and Z^0 are given masses (M_W and M_Z respectively) via the Higgs mechanism [6]. It is these masses which cause the apparent weakness of the weak force — at low energies, interactions are highly suppressed by the need to produce a virtual weak vector boson.

The $SU(2)_L$ field couples only to left-handed fermions. These transform as weak isospin doublets, with a weak isospin quantum number $t = 1/2$. The up-type member of each doublet is assigned a third component of isospin $t_3 = +1/2$, whilst the down-type member has $t_3 = -1/2$:

$$t = 1/2, \quad t_3 = \left\{ \begin{array}{c} +1/2 \\ -1/2 \end{array} \right. \quad \begin{pmatrix} u \\ d' \end{pmatrix}_L \quad \begin{pmatrix} c \\ s' \end{pmatrix}_L \quad \begin{pmatrix} t \\ b' \end{pmatrix}_L$$

$$t = 1/2, \quad t_3 = \left\{ \begin{array}{c} +1/2 \\ -1/2 \end{array} \right. \quad \begin{pmatrix} \nu_e \\ e^- \end{pmatrix}_L \quad \begin{pmatrix} \nu_\mu \\ \mu^- \end{pmatrix}_L \quad \begin{pmatrix} \nu_\tau \\ \tau^- \end{pmatrix}_L$$

In the case of the quarks, the eigenstates with which the weak force interacts are not quite the same as the mass eigenstates. Instead, the down-type quarks, d, s and b undergo mixing under the operation of a matrix (the CKM matrix) into d', s' and b':

$$\begin{pmatrix} d' \\ s' \\ b' \end{pmatrix} = \begin{pmatrix} V_{ud} & V_{us} & V_{ub} \\ V_{cd} & V_{cs} & V_{cb} \\ V_{td} & V_{ts} & V_{tb} \end{pmatrix} \begin{pmatrix} d \\ s \\ b \end{pmatrix}$$

As a result of this mixing, b quarks are able to decay to c quarks via the charged weak interaction:

$$b \rightarrow c + W^- .$$

The W subsequently decays semileptonically, to a charged lepton and a neutrino, or hadronically to a pair of quarks. (As throughout this thesis, the mention of a particular state or reaction also implies its charge conjugate).

The $b \rightarrow c$ transition is possible because the s' weak eigenstate, which appears in the same doublet as the c quark, contains a fraction V_{cb} of the b mass eigenstate. The transition takes place between the elements of the $(c, s')_L$ doublet. It is also possible for the b to decay via the $(u, d')_L$ doublet, but since it is lighter than the top quark it cannot do so via $(t, b')_L$. Because the decay of the b quark can only proceed through the intrinsically slow weak force and because it is further inhibited by the factor $V_{cb} = 0.036$–0.046 (or the even smaller factor $V_{ub} = 0.002$–0.005), it has a long lifetime compared to other quarks (around 1.5 ps [9]). No flavour mixing has been observed amongst leptons, so that it appears that lepton number is conserved separately for each flavour.

1.1.4 The process $Z^0 \rightarrow$ *hadrons*

This thesis is concerned with interactions of the form $Z^0 \rightarrow$ *hadrons* at the LEP collider. (Although $Z^0 \rightarrow \tau^+\tau^-$ events can also produce hadrons, throughout this thesis, the notation $Z^0 \rightarrow$ *hadrons* refers only to events of the type $Z^0 \rightarrow q\bar{q}$). At LEP during the LEP I phase of operations, electrons and positrons were collided with a centre of mass energy around the Z^0 mass peak, in the reaction $e^+e^- \rightarrow Z^0 \rightarrow f\bar{f}$. The fermion, f, is any from Table 1.1 except t, which is too heavy to be directly produced at this energy. The lowest order 'tree level' diagrams for this process are the photon and Z^0 exchanges shown in Figure 1.2. The Born approximation to the Standard Model gives the cross-section when only these diagrams are considered. (In

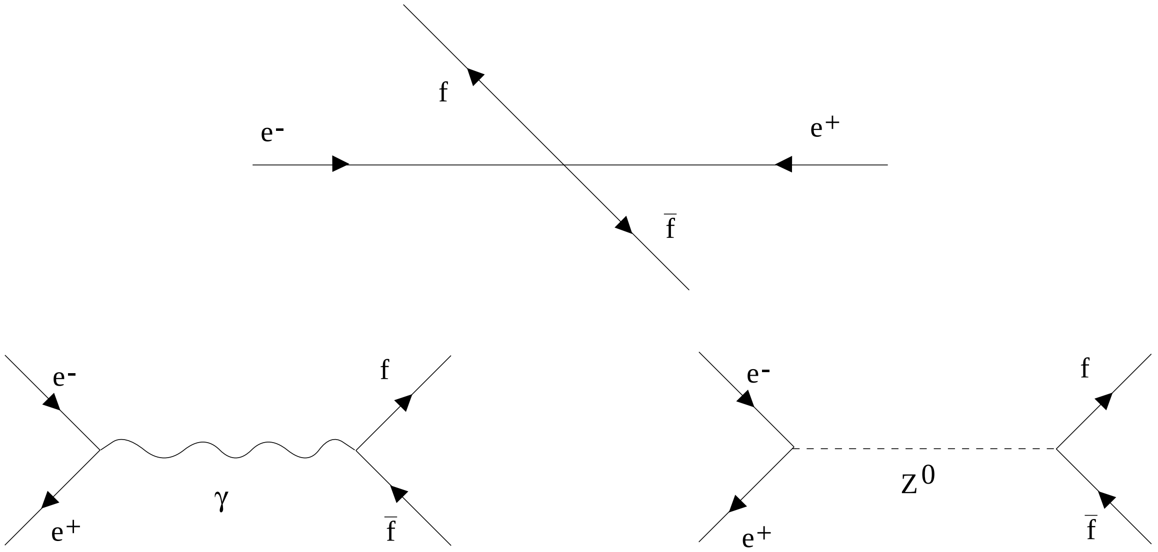

Figure 1.2: *Kinematics and lowest order diagrams in* $e^+e^- \to f\bar{f}$.

the case where f is an electron, tree-level diagrams corresponding to the scattering of the incoming electron and positron, without annihilation, must also be included).

In the Born approximation, the amplitude can be expressed in terms of fermion currents and vector boson propagators so that

$$\mathcal{M} = \mathcal{M}_\gamma + \mathcal{M}_{NC}\,, \tag{1.8}$$

where $\mathcal{M}_\gamma$ and $\mathcal{M}_{NC}$ are the contributions from photon and Z^0 exchange respectively:

$$\mathcal{M}_\gamma = -e^2(\bar{u}_f Q_f \gamma^\mu v_f)(\frac{g_{\mu\nu}}{k^2})(\bar{v}_e \gamma^\nu u_e) \tag{1.9}$$

and

$$\mathcal{M}_{NC} = \frac{-e^2}{4\sin^2\theta_W \cos^2\theta_W}(\bar{u}_f \gamma^\mu (c_v^f - c_a^f \gamma_5) v_f)(\frac{g_{\mu\nu} - k_\mu k_\nu / M_Z^2}{k^2 - M_Z^2 + i\Gamma_Z M_Z})(\bar{v}_e \gamma^\nu (c_v^e - c_a^e \gamma_5) u_e) \tag{1.10}$$

where k is the sum of the ingoing 4-momenta, u_f and v_f denote the fermion spinors and Q_f is the fermion charge. The contribution from Z^0 exchange also depends on $c_v^f = (t_3^f - 2\sin^2\theta_W Q_f)$ and $c_a^f = t_3^f$, the vector and axial vector coupling to the fermions, where t_3^f is the third component of weak isospin for f.

From the $Z^0 f\bar{f}$ vertex, the decay rate $\Gamma(Z^0 \rightarrow f\bar{f})$ can be calculated in the Born approximation as a sum of vector (V) and axial (A) terms:

$$\Gamma(Z^0 \rightarrow f\bar{f}) = \Gamma_0^V + \Gamma_0^A \,, \tag{1.11}$$

where these terms are given by the expression

$$\Gamma_0^{V(A)} = \frac{N_c e^2 M_Z}{48\pi \sin^2\theta_W \cos^2\theta_W}(c^f_{v(a)})^2 \,. \tag{1.12}$$

Here N_c is the number of colours possible — 3 in the case of quarks. A correction for the finite mass, m_f, of the final state fermions can also be applied [10]:

$$\Gamma(Z^0 \rightarrow f\bar{f}) = \frac{1}{2}\beta(3-\beta^2)\Gamma_0^V + \beta^3\Gamma_0^A \,, \tag{1.13}$$

where the mass dependence is included in $\beta = \sqrt{1-\mu^2}$, $\mu = 4m_f^2/k^2$. For b quarks, this correction corresponds to $\mathcal{O}(10^{-2})$ in the axial term and $\mathcal{O}(10^{-4})$ in the vector term.

An event of the type $Z^0 \rightarrow$ *hadrons* occurs when the Z^0 decays to a quark-antiquark ($q\bar{q}$) pair. Unlike a Z^0 decay to muons or electrons, the final-state fermions cannot be directly observed in the final state of a hadronic event. This is due to quark confinement. As the primary quarks move away from each other, the colour field between them increases. This energy allows more $q\bar{q}$ pairs to be pulled from the vacuum, until eventually all the quarks are bound inside colourless hadrons. The final state of a $Z^0 \rightarrow$ *hadrons* event thus contains jets of hadrons. Usually there are two jets, each originating from one of the primary quarks, or three jets, where one originates from a hard gluon emitted from a primary quark before hadronization took place.

Unfortunately, although perturbation theory can be applied at the energy where the primary quarks are produced, their subsequent confinement within hadrons occurs at a scale which falls into the non-perturbative region of QCD. Because of this, one must rely on approximations and phenomenological methods. Some of these have been implemented within Monte Carlo event generator packages such as JETSET [11,12], which is used for the ALEPH event simulation.

JETSET makes use of the parton shower model to produce a quark-gluon cascade from the original $q\bar{q}$ pair. This is an iterative branching scheme where quarks (q) and gluons (g) split $q \rightarrow qg$, $g \rightarrow q\bar{q}$ and $g \rightarrow gg$. The probability of the first branchings from the primary quarks is determined by the first order perturbative QCD matrix element. Subsequent branching probabilities are taken from the Leading Logarithm Approximation of perturbative QCD. The process is terminated by an infrared cut-off of $\sim 1\,\mathrm{GeV}$ on the invariant mass of the two parton system produced in a branching. A second approach is the Matrix Element method. This uses exact calculations based on the strong interaction matrix elements in perturbative QCD up to second order and allows a maximum of four partons in the final state.

The hadronization process is approached within JETSET by the Lund string fragmentation model. This supposes that colour strings with constant energy per unit length are stretched between the partons created in the parton shower. When the energy present is sufficient to create a $q\bar{q}$ pair, this is done and the string is broken in two. The process continues until there is no longer enough energy to produce new pairs, at which point in the simplest model the adjacent quarks and antiquarks pair off to form mesons. Baryon production is not well understood. A model is used where occasionally a diquark-antidiquark pair $qq'\overline{qq'}$ is produced, which combines with other quarks from $q\bar{q}$ pairs to form baryons instead of mesons. Parameters such as the relative rates of scalar to vector mesons and of mesons to baryons are empirically set.

It is useful to define the variable $z = (E + p_{||})_{\mathrm{hadron}}/(E + p)_{\mathrm{quark}}$, which gives the fraction of the primary quark's energy and longitudinal momentum carried by the hadron. For heavy flavours, the probability distribution of z gives a harder energy spectrum than for light quarks. The ALEPH event simulation makes use of the Peterson fragmentation model [13], which is found to give good agreement with the spectrum observed in the experimental data.

1.1.5 Beyond the Standard Model

Despite its success to date, it is generally thought that the Standard Model as it stands must be a low-energy approximation to some more general theory. Certainly, it is believed to break down at or before energies corresponding to the Planck scale, the point where quantum gravity becomes significant. Even before this scale, the model in its present form causes problems to arise in the Higgs sector. The mass of the Higgs gains large radiative corrections which turn out to be linearly dependent on the cutoff point where the Standard Model ceases to be valid [14]. If this was as large as the Planck scale, the mass would become so great that the self-coupling of the

Higgs would violate unitarity (ie. the probability of this interaction would exceed 1). In order to generate a Higgs mass suitable for use in electroweak symmetry breaking either the parameters of the region above the cut-off scale must be fine-tuned to an extreme degree, or the cut-off scale must be of the order of a TeV.

Several theories have been put forward as possible ways in which the Standard Model might be extended. One example of these is supersymmetry, or SUSY [15], a popular implementation of which is the Minimal Supersymmetric Standard Model (MSSM). In the MSSM, every Standard Model fermion has an associated supersymmetric boson partner and every boson a supersymmetric fermion partner. The latter (the photino, wino and zino) mix with one another and with an extended supersymmetric Higgs sector (higgsinos) to produce charginos and neutralinos. The supersymmetric counterparts to the quarks are stop and sbottom squarks and so on, whilst the lepton partners are the sleptons.

Supersymmetric theories have many attractive features. They solve the Higgs sector fine-tuning problem mentioned above, so long as the super-partners exist at or below the TeV scale. When they are incorporated into Grand Unified Theories, they allow unification of coupling constants at a level which is consistent with proton decay experiments, if the scale of supersymmetry breaking is order $\sim 1\,\mathrm{TeV}$. In addition, they provide a natural candidate for dark matter, in the shape of the lightest supersymmetric particle, so long as this is stable, neutral and colourless. Supersymmetric particles quickly decouple from Standard Model particles at energies below their production thresholds. Because of this, the predictions of the MSSM can easily conform to the precision electroweak measurements made at LEP, or to the limits on rare processes such as that placed by CLEO on $b \to s\gamma$. The disadvantage of supersymmetry is that it introduces a plethora of new particles, none of which have yet been observed.

1.2 Precision tests of the Standard Model

Because of the comparatively weak strength of the electroweak interaction, it is possible to use perturbation theory to predict experimental observables with very high precision. The Standard Model has 18 input parameters, which are: The coupling strengths α, α_s and G_F of the electromagnetic, strong and weak forces respectively, the masses M_Z and M_H of the Z^0 and Higgs bosons, the nine masses of the quarks and charged leptons and the three amplitudes and one phase needed to describe the

CKM matrix. Of these parameters, α, G_F, M_Z and the masses of the charged leptons are the best known. The top and bottom quark masses and the parameter of the CKM matrix that links the first two generations are less well known. The charm and light quark masses, α_s and the remaining CKM matrix parameters are poorly known. Finally, the mass of the Higgs boson is still unknown. However, limits have been placed on the possible value of the Higgs mass. For example, using the full data sample collected during the LEP I phase of operations, ALEPH achieves a 95 % confidence limit of 63.9 GeV [16].

1.2.1 The electroweak fit

At tree level, predictions for the observables included in the electroweak fit can be made solely in terms of the three best-known parameters: α, G_F and M_Z. Such observables include the total and partial widths of the Z^0 and the polarization of its decay products. They also include the forward-backward and left-right asymmetries for fermions produced in Z^0 decay. The forward-backward asymmetry measures the difference between the angular distributions of outgoing fermions and anti-fermions, whilst the left-right asymmetry measures the difference in cross-section for initial right and left-handed electrons.

Beyond tree level, it is necessary to take account of loop corrections which depend on α_s and the fermion and Higgs masses. When these corrections have been made, the theoretical predictions can be compared to the measured values. By making a fit to the experimental results, constraints on the remaining input parameters of the prediction are obtained, most notably the Higgs and top quark masses and α_s. In addition, the mutual consistency of the observed results, as measured by the χ^2 of the fit, gives an indication of the validity of the Standard Model predictions.

Any element of the electroweak fit whose experimental value cannot be accommodated may be an indication of physics beyond the Standard Model. Measurements at the LEP experiments and SLD are precise enough that the loop corrections must be included in the fit. This means that it is possible to observe the effects of new physics which enters the loops but cannot otherwise be seen. An example of this would be new particles which were too heavy to be directly produced. Conversely, the extent to which any proposed theory would alter the electroweak observables is an important constraint on extensions to the Standard Model. Thus, it is possible to probe physics at the TeV scale with a machine operating at the Z^0 mass peak.

1.2.2 The role of R_b

Most of the variables in the electroweak fit depend on the square of the top quark mass, m_t^2, and the logarithm of the Higgs mass, $\ln(M_H)$. In the case of $\Gamma_{Z^0 \to b\bar{b}}$, the coupling between the top and b quarks has a particularly large impact. The other loop corrections, dependent on $\ln(M_H)$ and α_s, are the same for all quark flavours, so that they factor out when the ratio $R_b = \Gamma_{Z^0 \to b\bar{b}}/\Gamma_{Z^0 \to hadrons}$ is taken. Hence, an indirect measurement of the top mass is possible which complements the information from other elements in the fit. The value of the top mass extracted from the fit can be compared to the direct measurements made at CDF and D0.

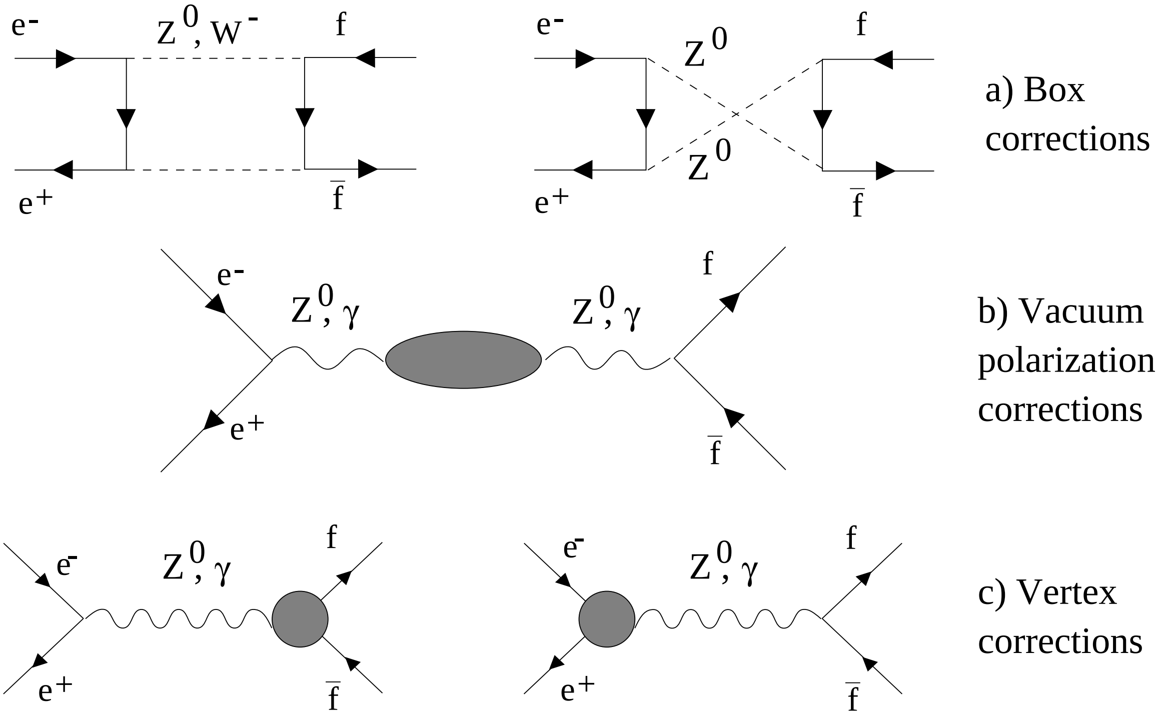

Figure 1.3: *Corrections to the $e^+e^- \to f\bar{f}$ process.*

Figure 1.3 shows the one-loop and higher order corrections to the Born approximation of the amplitude for $e^+e^- \to Z^0 \to f\bar{f}$. They can be divided into three categories [17]:

Box: The corrections due to box diagrams (Figure 1.3 a) are very small, typically $\Delta_{\mathrm{BOX}} \leq 0.1\,\%$ near the Z^0 peak, due to their non-resonant nature.

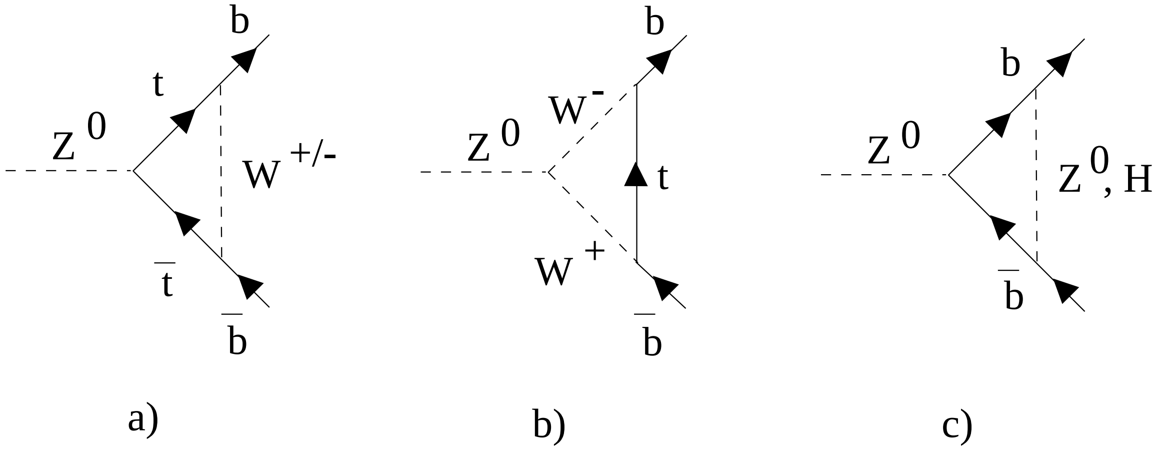

Figure 1.4: *One-loop vertex corrections for* $Z^0 \to b\bar{b}$.

Vacuum polarization: These corrections to the propagator (Figure 1.3 b) are the largest, typically $\Delta_{\mathrm{VACUUM}} \leq 10\,\%$. However, they are the same for all quark flavours and hence cancel in the ratio R_b.

Vertex: These corrections (Figure 1.3 c) are of the order $\Delta_{\mathrm{VERTEX}} \leq 1\,\%$ for particles other than b quarks. For the b quark the situation is different, because of its large coupling to the top quark. The size of the correction varies according to the value of m_t^2, reaching $\Delta^b_{\mathrm{VERTEX}} = 2.4\,\%$ if $m_t = 175\,\mathrm{GeV}$.

The one-loop diagrams contributing to $\Delta^b_{\mathrm{VERTEX}}$ are shown in Figure 1.4. This correction has the form [17]:

$$\Delta^b_{\mathrm{VERTEX}} = -\frac{20\alpha}{13\pi}\left(\frac{m_t^2}{M_Z^2} + 136 \log \frac{m_t^2}{M_Z^2}\right) + \cdots \tag{1.14}$$

1.2.3 The effect of new physics on R_b

Any new physics which preferentially affected the $Z^0 b\bar{b}$ vertex might be detected as a discrepancy between the measured value of R_b and the Standard Model prediction. There are many extensions to the Standard Model in which the third generation, with the heavy top quark, attracts unique vertex corrections. As an example, it is useful to examine the predictions for R_b within the framework of the Minimal Supersymmetric Standard Model. The MSSM might be able to explain a discrepancy between the Standard Model prediction and the measured value of R_b. If it was then assumed

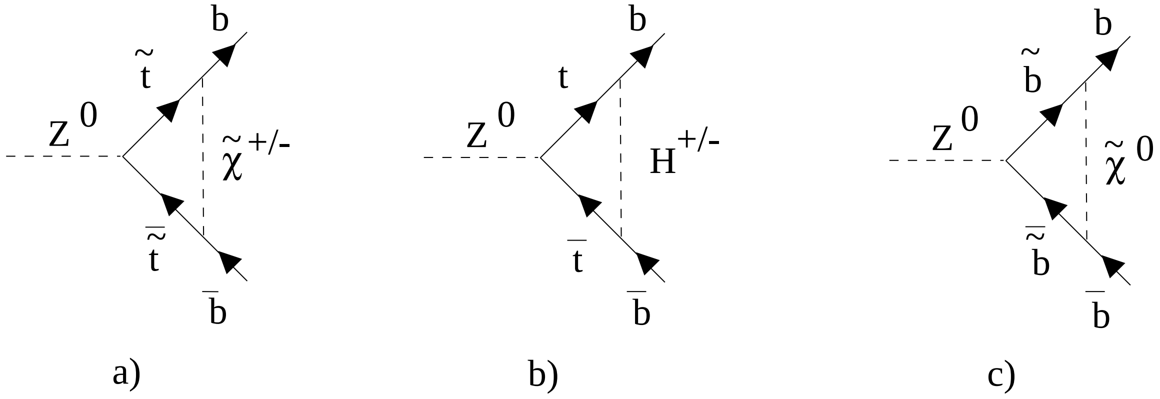

Figure 1.5: *Vertex corrections for* $Z^0 \to b\bar{b}$ *in the MSSM.*

that any discrepancy seen was due to supersymmetry, its magnitude and direction could provide some constraints on the parameter space of the theory.

Figure 1.5 shows some of the corrections to the $Z^0 b\bar{b}$ vertex in the MSSM. Figure 1.5 a contains stop squarks and a chargino. The chargino mass eigenstate is a mixture of wino and charged higgsino, making this the supersymmetric equivalent of Figure 1.4 a. Figure 1.5 b involves a charged Higgs boson. Finally, Figure 1.5 c contains a neutralino and is the supersymmetric equivalent of the b-neutral Higgs correction which is shown in Figure 1.4 c.

When making and testing predictions for R_b within the framework of the MSSM, it is necessary to fix the various free parameters of the model. Those parameters which affect R_b [18] include $\tan\beta$ (the ratio of the vacuum expectation values for the two Higgs fields), the sign of μ (the Higgs mass mixing parameter) and the masses of the stop squark and the chargino. Given the large discrepancy between the experimental measurement of R_b and the Standard Model prediction at the time of the 1995 summer conferences [1, 2], many recent examinations of supersymmetric corrections to R_b [18–20] have focussed on whether and with what parameters it is possible to explain such a deviation.

One such analysis is described in [20], where a large number of points in the parameter space of the MSSM were sampled. Any points which contradicted the experimental bounds for such observables as the rate of $b \to s\gamma$ or the lower limit on the mass of the lightest Higgs boson were discarded. The size of the supersymmetric correction to the value of R_b was then examined. The maximum possible correction obtained is shown in Figure 1.6 as $(R_b^{susy})_{max}$, plotted against the mass of the stop squark. This value should be compared to, for example, $R_b = 0.2172 \pm 0.0020$, the result of the analysis presented in this thesis. The most stringent of the constraints placed by the various experimental observables was found to be due to the limit on the chargino mass obtained from the LEP 1.5 run at 130 GeV.

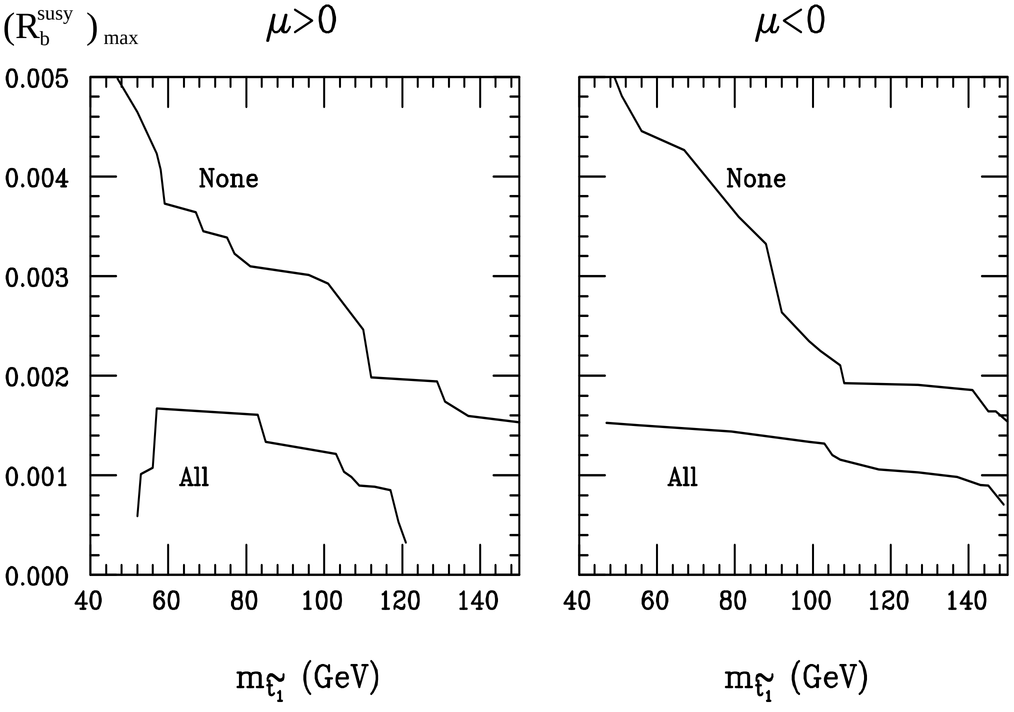

Figure 1.6: *The maximum supersymmetric contribution to R_b, plotted against the stop squark mass for both signs of μ. For comparison, the value of R_b from the analysis presented in this thesis is 0.2172 ± 0.0020. Two cases are shown — 'All', where constraints from experimental observables are imposed and 'None', where no such constraints are used. This figure is taken from [20].*

1.3 Summary

The Standard Model description of the process $Z^0 \to hadrons$ provides a theoretical framework for predicting of the value of R_b. In the fit to precision electroweak measurements, R_b plays a special role. It is relatively insensitive to such parameters as

α_s or the mass of the Higgs, whilst having a strong dependence on the square of the top quark mass. Thus, R_b can be used to provide an indirect determination of m_t. This can then be compared to the direct top mass measurement from CDF and D0.

Many of the proposed extensions to the Standard Model, such as supersymmetry, would lead to new corrections to the $Z^0b\bar{b}$ vertex. Hence, a precision measurement of R_b can give hints as to the form such physics may take and may also be used to place limits on such models.

The corrections to the $Z^0b\bar{b}$ vertex are of the order of a few percent. For discrepancies of this size between the measured and predicted value to become significant, it is thus necessary to measure R_b with a relative accuracy of around 1 %.

Chapter 2

The ALEPH detector at LEP

The analysis presented in this thesis was carried out at CERN, the European Laboratory for Particle Physics, using data produced by LEP, the Large Electron-Positron collider, and collected by the ALEPH experiment during the years 1992–95. This chapter gives an overview of LEP and the ALEPH detector, with emphasis on those elements most important to the analysis. Chapter 3 will describe the ALEPH silicon vertex detector in more detail. Further information on LEP and ALEPH can be found in [21] and [22–24] respectively.

2.1 The LEP collider

The discovery in 1983 of the electroweak gauge bosons, Z^0 and $W^\pm$, was striking evidence in support of the Standard Model. The Large Electron Positron collider, LEP, was constructed to enable these particles to be studied in detail and to test the parameters of the Standard Model to very high precision. Electron-positron annihilation provides a clean environment for these studies.

The LEP operation was divided into two phases:

- LEP I, designed for the study of the Z^0, with a centre of mass energy around 91 GeV. The analysis presented here used data that was collected during this phase.

- LEP II, designed for the study of $W^\pm$ pairs, with a centre of mass energy around 175 GeV. This phase began at an energy of 130 GeV in October 1995 and is forseen to rise to 175 GeV over the next year.

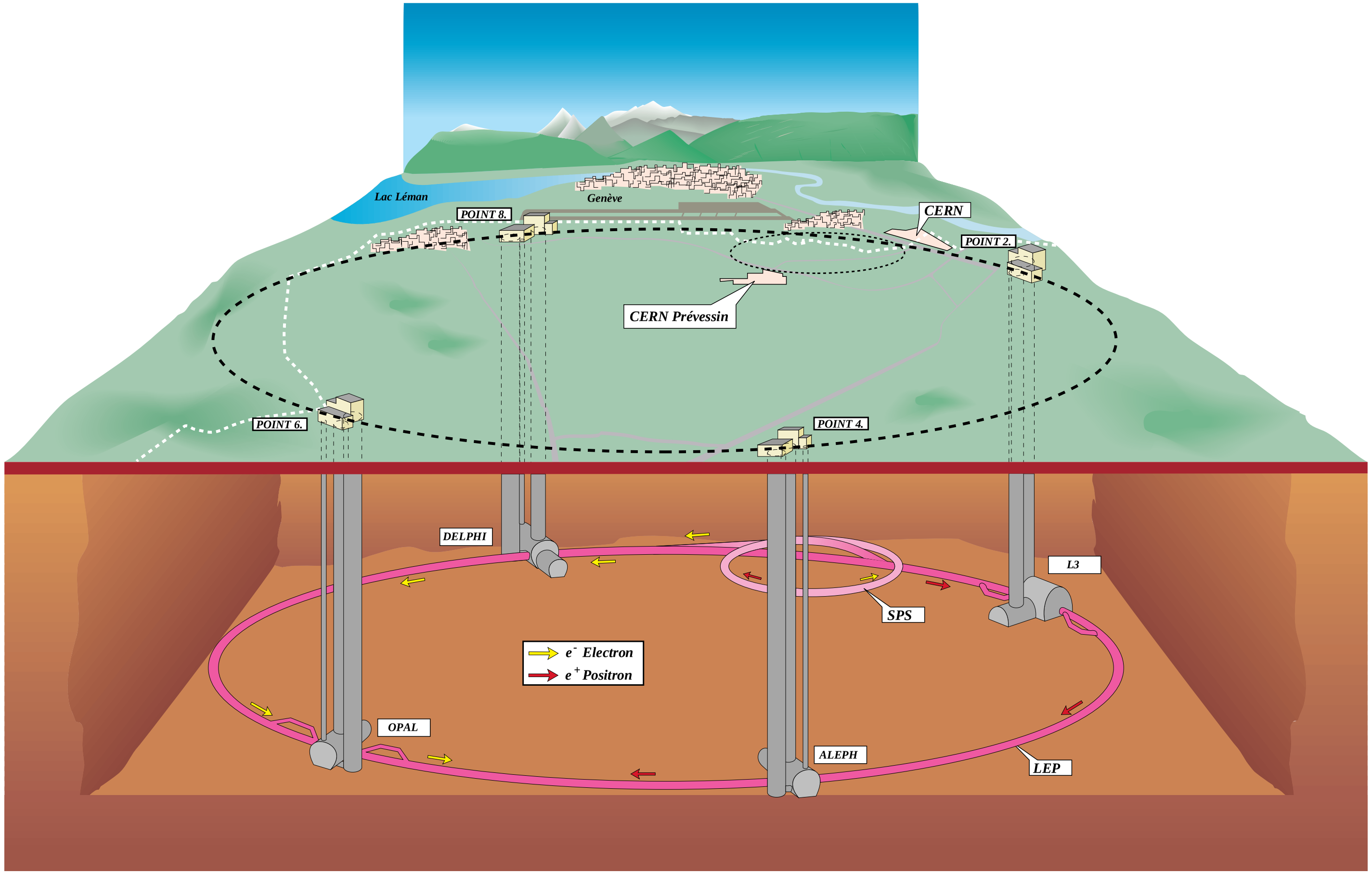

Figure 2.1: *Schematic view of LEP and the surrounding area.*

LEP is one of the accelerators at CERN, situated on the French-Swiss border near Geneva. It is a nearly circular ring almost 27 km in circumference, housed in a tunnel 50–175 m below ground (shown in Figure 2.1). The reason for the large scale of the collider is the effect of synchrotron radiation: A charged particle moving along a curved path will radiate photons with an energy proportional to E^4/R where E is the particle energy and R is the radius of curvature. It is worth noting that the accelerator was constructed with a precision better than 1 cm.

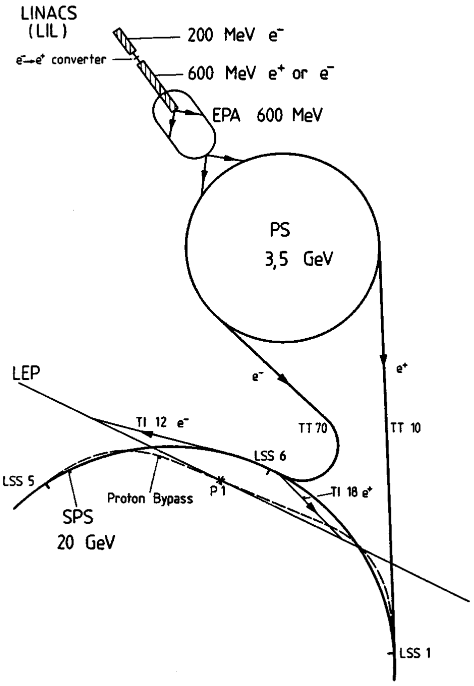

Figure 2.2: *The LEP injection system.*

The stages by which the electrons and positrons are injected into LEP are shown in Figure 2.2 . Electrons from a high-intensity electron gun are accelerated to 200 MeV in a linear accelerator, or LINAC, after which some of them are fed through a tungsten convertor to produce positrons. Both electrons and positrons are then accelerated by a second LINAC to an energy of 600 MeV. These leptons are formed into packets and accumulated in the Electron Positron Accumulator (EPA) before being injected into the Proton Synchrotron (PS) which accelerates the packets to 3.5 GeV. From here, they move to the Super Proton Synchrotron (SPS) to be accelerated to 20 GeV and finally to LEP, where they are brought to the target energy.

The beams inside LEP circulate in bunches, which are typically $\sim 1.5\,\mathrm{cm}$ long, with horizontal and vertical dimensions in the transverse plane of $\sim 250\,\mu\mathrm{m}$ and $\sim 15\,\mu\mathrm{m}$ respectively. Until October 1992, there were four equally spaced bunches per beam, increased to eight for the 1993–94 running periods. From 1995 onwards, the beams have been divided into four bunch trains, each containing up to three bunch wagons. Most of the data used in this analysis was collected in the 8-bunch mode, in which the beams collided once every $11\,\mu\mathrm{s}$. The mean luminosity achieved at LEP I was about $10^{31}\,\mathrm{cm}^{-2}\mathrm{s}^{-1}$, with an average beam lifetime of more than 11 hours.

2.2 The ALEPH detector

2.2.1 General overview

ALEPH (Apparatus for LEP PHysics) is one of four detectors around the LEP ring and is described in detail elsewhere [22–24]. It was constructed as a general purpose detector for e^+e^- collisions, to study all areas of physics accessible at LEP. Such a detector would ideally be able to detect all particles, identify them and measure their momentum, energy and trajectories.

Aiming for the best compromise between these objectives, ALEPH was designed to have good track momentum resolution, fine granularity of the calorimeters and as near to full coverage of the 4π solid angle as possible. This enables it to measure the momenta of charged particles in three dimensions and the energy deposited in calorimeters by charged and neutral particles, to identify the three lepton flavours and to measure the distance travelled by weakly decaying particles such as the tau and hadrons containing b and c quarks.

A schematic view of the ALEPH detector is given in Figure 2.3. It shows the arrangement of the detector in concentric shells, with tracking detectors at the centre, surrounded by the calorimeters. The ends of the cylindrical barrel of the detector are closed by end-caps, allowing for very good hermeticity and solid angle coverage. The detector is about 11 m long and 10 m in diameter.

The conventional coordinate system used by ALEPH and throughout this thesis is defined with its origin at the nominal interaction point. The z axis points along the beam direction, the x axis towards the centre of the LEP ring and the y axis

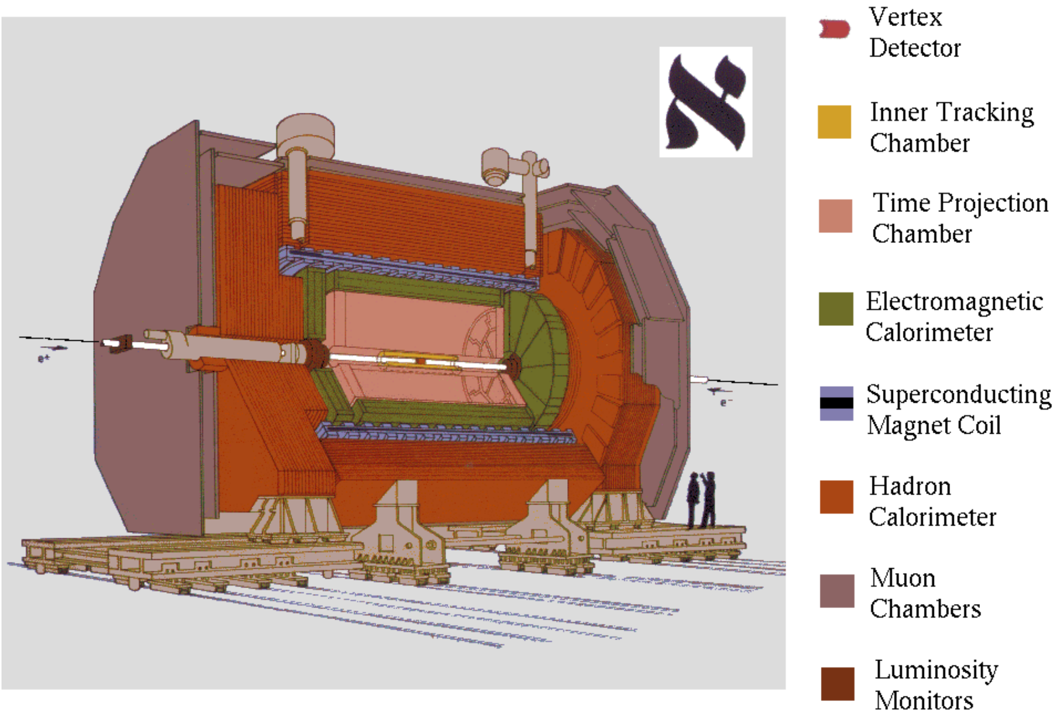

Figure 2.3: *The ALEPH detector.*

vertically upwards. The cylindrical coordinates r and ϕ and the polar angle θ are then defined with respect to the z axis in the standard manner.

Each functional unit of the detector is referred to as a subdetector, the most important of these being listed below:

- A silicon vertex detector (VDET), described in Chapter 3. It consists of two layers of double-sided silicon microstrip detectors which give very good resolution of track impact parameters and vertex positions close to the interaction point.

- An inner tracking chamber (ITC), which performs fast tracking and provides trigger information.

- A time projection chamber (TPC), providing accurate 3-dimensional tracking of charged particles. The magnetic field permits measurement of track momenta and dE/dx information allows particle identification.

- A finely grained electromagnetic calorimeter (ECAL), which detects and reconstructs electrons and photons.

- A superconducting coil which provides a uniform magnetic field of 1.5 T.
- A hadron calorimeter (HCAL), which measures the energy of hadrons and identifies muons.
- Two layers of muon chambers, for muon detection.
- Some luminosity detectors (LCAL, SICAL and BCAL), which measure the luminosity delivered by LEP.

2.2.2 Measuring the trajectories and momenta of charged particles

A charged particle moving through matter will interact with and possibly ionise the surrounding atoms. The electrons and ions can then be prevented from recombining by the presence of an electric field, pulling them apart towards the electrodes that create the field. The charge collected in this way provides an electrical signal that a charged particle has passed and further information can be gained from the size and timing of the signal. The technique of observing the ionisation produced by charged particles in matter is used by gas detectors and solid state detectors. The latter are discussed in Chapter 3; a brief discussion of the former is given here.

Gas detectors rely on the principle of avalanche. This occurs when the electric field through which the ionised atoms and electrons drift is sufficiently strong that on their way to the electrodes, they ionise more atoms. These new electrons and ions are accelerated by the field in their turn and can ionise more atoms, creating an avalanche and large amplification of the initial charge. In practice, this effect is only significant with electrons, as ions are too heavy to be easily accelerated, so that the avalanche takes place close to the anode. This leads to the classic design of a gas detector — a gas-filled cylinder whose surface forms a cathode, with a sense wire at its centre that acts as an anode. A refinement of this is the so-called multiwire design. Here, many anode wires are sandwiched between two cathode plates to form a flat chamber, or else cathode wires are arranged around each anode wire. In these configurations, the position of the particle is known from the position of the wire on which the signal pulse is detected.

Once the trajectory of a charged particle can be measured, its momentum can be deduced if the detector is inside a magnetic field. A charged particle moving in a magnetic field describes a circle whose radius is proportional to the component of its momentum perpendicular to the magnetic field and inversely proportional to its charge. Since all charged particles that can be directly observed with the ALEPH detector have charge of magnitude 1, the size and sign of the radius of curvature is all that is necessary to give the momentum and charge of the particle.

The measurement of charged particle direction and momentum, or tracking, is performed in ALEPH by three different sub-detectors — the large-volume TPC, the fast ITC and the very precise, solid-state VDET. This region is immersed in a 1.5T magnetic field parallel to the beampipe, provided by a superconducting solenoid. The longitudinal component of this field is uniform to better than 0.2 % inside the volume of the tracking system.

2.2.3 Trajectories, momenta and dE/dx: the TPC

The time projection chamber, or TPC, (shown in Figure 2.4) is the main tracking device in ALEPH, providing accurate 3-dimensional tracking and good momentum resolution for charged tracks. It consists of a large cylinder of gas, the axis of which is parallel to the beam-pipe and the magnetic field. There is also an electric field, directed from the chamber end-plates towards a central membrane held at −27 kV. This membrane and a set of annular electrodes on the cylinder wall together create a uniform field of 11 kV/m. Electrons from ionisation drift in tight spirals to the end-plates where their arrival positions and times are measured by wire chambers.

The TPC cylinder is 4.7 m long, with inner and outer radii of 0.31 m and 1.8 m respectively. It is filled with gas at atmospheric pressure that consists of a mixture of 91 % argon, chosen for its desirable ionisation properties, and 9 % methane, which allows the avalanche to be stopped before it gets out of control.

Once the drifting electrons reach the end-plates, they are detected by wire chambers (shown in Figure 2.5). Cathode wires shape the electric field around the anode sense wires, which collect electrons from avalanches created by the ionisation electrons. Cathode pads underneath the sense wires collect an induced signal and an accurate measurement of the $r\phi$ coordinate of the track is achieved by interpolation between the signals on different pads. The z coordinate is deduced from the arrival time of the pulse and knowledge of the electron drift velocity. Since there are 21

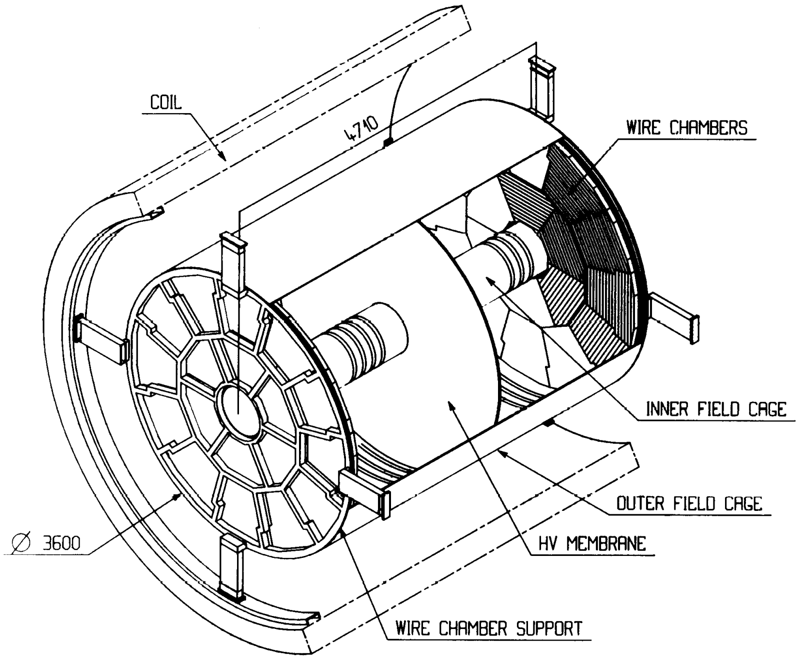

Figure 2.4: *The ALEPH time projection chamber.*

concentric rings of cathode pads, the TPC can provide up to 21 3-dimensional points for each track.

Between the cathode wires and the chamber lies a plane of gating wires. The purpose of this is to prevent positive ions produced in the avalanche near the sense wires from entering the main chamber, where any build-up of charge would distort the electric field. When the gate is closed, the potential on the wires creates a barrier that prevents charged particles from crossing. When a beam crossing is due, the gate is opened. This means that the wires are held at a constant potential at a value which makes it transparent to the drifting electrons. If the first level trigger is positive, indicating that the TPC information will be read out, the gate is held open for 45μs to allow the electrons to drift in, otherwise it is closed again.

The TPC is equipped with a laser calibration system that provides information on the distortion of particle tracks and provides a check on the electron drift velocity (which is first measured using the constraint that tracks on either side of the central

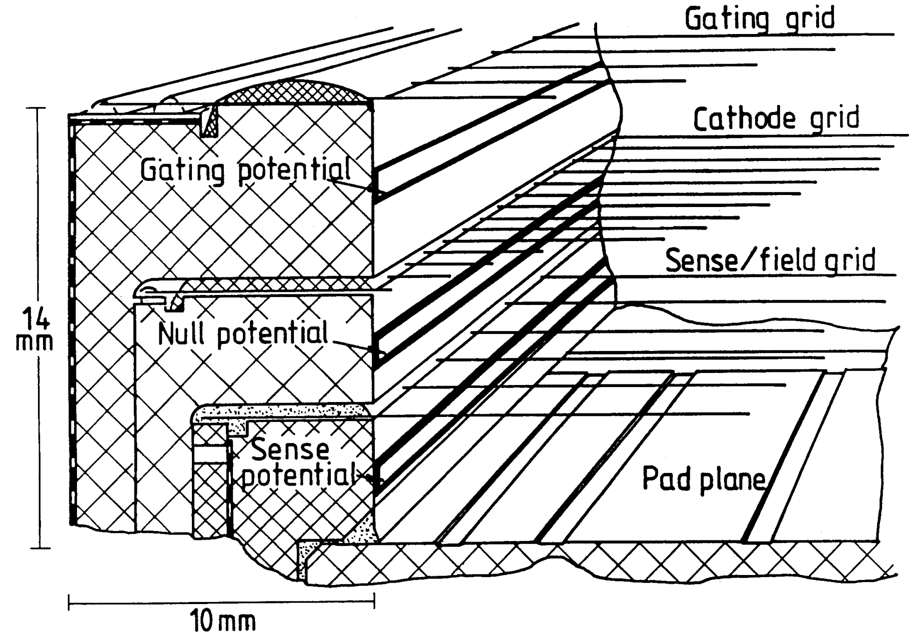

Figure 2.5: *A section through a TPC wire chamber, showing the arrangement of the sense wires, cathode pads and gating grid.*

membrane should originate from the same point). Beams from the laser cause tracks of ionisation in the chamber. When these tracks are then detected, any deviations from straightness indicate inhomogeneities of the electric and magnetic fields which can cause a systematic displacement of the measured coordinates.

After all corrections, a value of $\sigma_{r\phi} = 173\,\mu$m is measured for the azimuthal coordinate resolution. The longitudinal resolution is $\sigma_z = 740\,\mu$m for tracks making an angle greater than 80° to the beampipe. In general, the coordinate resolution depends on the drift length and the polar angle of the track in a manner which has been parameterised and is incorporated into the track fit errors.

The magnitude of the signals measured by the wire chambers can be used for particle identification, since they are proportional to the ionisation caused by the particle which in turn is proportional to its energy. Because the rate of energy loss, dE/dx, by a particle passing through a given material depends only on its velocity, this quantity combined with knowledge of its momentum can be used to deduce the particle mass and hence identify it. This method is used to identify electrons, pions, kaons and protons.

2.2.4 Fast tracking: the ITC

Inside the TPC lies the inner tracking chamber (ITC), a cylindrical multiwire drift chamber 2 m in length and with inner and outer radii of 13 cm and 29 cm respectively. It provides up to 8 accurate points in the $r\phi$ plane for tracking and the only tracking information to be used by the first level trigger (Section 2.2.11). It is filled with a gas mixture consisting of 80 % argon, 20 % carbon dioxide (performing the same function as methane in the TPC) and a small amount of alcohol, which has been found to retard the ageing process of the chamber.

The ITC contains 960 sense wires, which run parallel to the beam direction. They are held at a voltage of about 1.8 kV and surrounded by six earthed field wires forming a hexagonal drift cell (Figure 2.6). These cells are arranged into eight layers, the inner four containing 96 cells each and the outer layers 144. The time taken for the ionisation charge to drift to the sense wire gives an $r\phi$ coordinate, with a precision

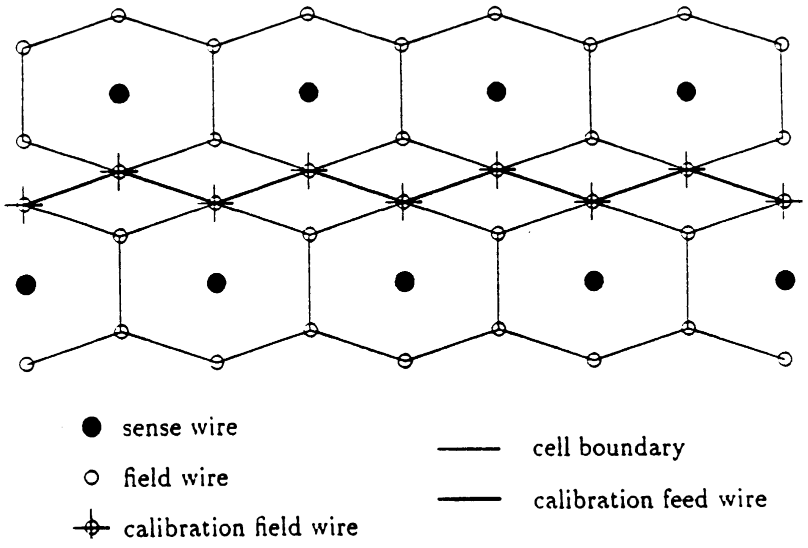

Figure 2.6: *Schematic diagram of ITC drift cells, showing the arrangement of the wires.*

that depends on the drift distance but on average is about 150 μm. The z coordinate is measured with an accuracy of a few cm by taking the difference in arrival times of the signals at either end of the sense wire, but this information is not used by the standard tracking procedure.

The trigger information provided by the ITC is based on track multiplicity, hit multiplicity per layer and detection of back-to-back topologies. The decision from the $r\phi$ trigger is available within 500 ns of the beam crossing, the fast response being due to the small size of the drift cells (about 1 cm). Information including the z coordinate is used by a spacepoint trigger, whose output is available after 2.5 μs.

2.2.5 High precision tracking: the VDET

The main purpose of the silicon vertex detector, or VDET, is to allow high precision measurement of charged tracks close to the interaction point, so that long-lived particles such as hadrons containing b quarks can be identified by the displaced vertices of their decay products.

The VDET consists of two layers at the centre of ALEPH, one at an average radius of 6.5 cm, the other at 11.3 cm. In each layer, 300 μm thick silicon wafers are joined together into faces, which lie parallel to the beampipe. The wafers have readout strips on both sides. On one side, the strips lie parallel to the beampipe and provide a coordinate in ϕ; on the other they are perpendicular and provide a coordinate in z. The known radius of the detector provides the r coordinate, completing the 3-dimensional measurement of the hit. In the first VDET, with which the data used by this analysis was collected, hit positions could be reconstructed with an accuracy of 12 μm in both $r\phi$ and z views.

The ALEPH silicon vertex detector is discussed further in Chapter 3.

2.2.6 Track reconstruction and determination of momentum

Using a combination of these three sub-detectors, each charged particle track can be traced by a string of points measured in three dimensions. Nearby hits in the TPC are connected by requiring that they be consistent with the expected helix trajectory, then extrapolated to the ITC and VDET and fitted with hits there. The parameters by which each track is defined are shown in Figure 2.7. They are: R, the radius of curvature of the track, $\tan\lambda$, where λ is the angle of the track to the xy plane ($\lambda = 90° - \theta$), d_0, the distance of closest approach in the xy plane of the track to the

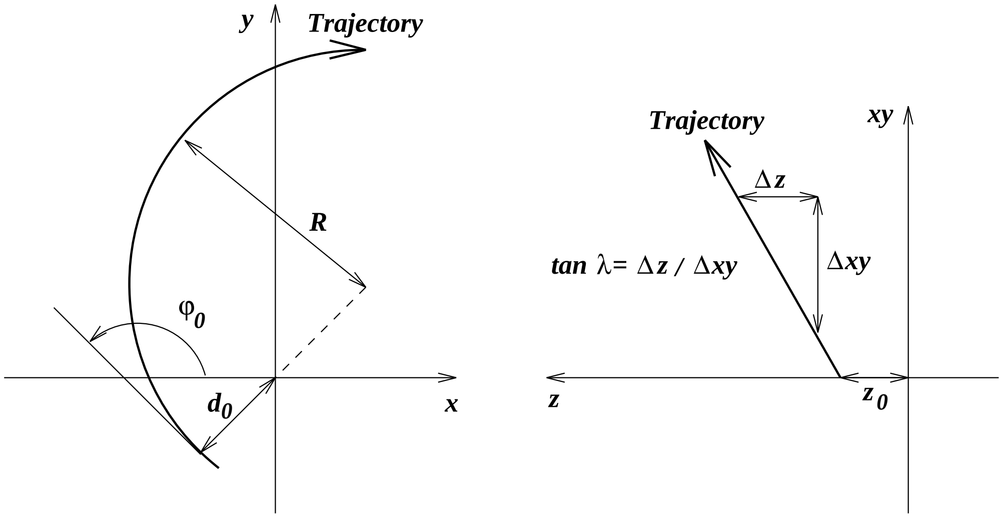

Figure 2.7: *Definition of the parameters of a charged track.*

primary vertex, z_0, the z coordinate of the track at the point of closest approach and ϕ_0, the azimuthal angle of the track at this point.

The performance of the reconstruction process is studied using $Z^0 \to \mu^+\mu^-$ decays. Table 2.1 shows the impact parameter resolution that can be achieved for these high-momentum tracks as each subsequent tracking detector is included in the fit. The great improvement contributed by the VDET is particularly evident.

Detectors	$(r\phi)/\mu$m	z/μm
TPC	310	808
TPC+ITC	107	808
TPC+ITC+VDET	23	28

Table 2.1: *Impact parameter resolution in $Z^0 \to \mu^+\mu^-$ events [24].*

For tracks in hadronic events, the impact parameter resolution in both ϕ and z as a function of momentum, p, is found to be [24]:

$$\sigma(\text{impact parameter}) = 25\,\mu\text{m} + \frac{95\,\mu\text{m}}{p/(\text{GeV})}\,, \tag{2.1}$$

where the poorer resolution at low momentum is due to multiple scattering.

Once the parameters of a charged track have been measured, it is possible to deduce its momentum. For 45 GeV muons, the resolution of this measurement is shown in Table 2.2. The gain from including the VDET is less valuable than in the case of impact parameter resolution, but is by no means negligible.

Detectors	$\sigma(1/p)/(\mathrm{GeV})^{-1}$
TPC	1.2×10^{-3}
TPC+ITC	0.8×10^{-3}
TPC+ITC+VDET	0.6×10^{-3}

Table 2.2: *Momentum resolution in $Z^0 \to \mu^+\mu^-$ events [24].*

2.2.7 Energy measurement and neutral particles

It is clear that the particle tracking system described so far is only able to detect charged particles. Neutral particles are detected with the calorimeters, which are also used for measuring the energies of charged and neutral particles. The neutral particles present and directly detectable in ALEPH are the photon and two types of hadron — K^0_L mesons and neutrons/anti-neutrons. Neutrinos are also present, but cannot be detected.

Neutral hadrons are detected by means of the strong force. As they pass through matter, they interact and produce more hadrons — mainly charged and neutral pions, protons and neutrons. These interact in their turn, creating a shower of hadrons. The charged particles so produced can be detected and used as a signal that a neutral hadron was present.

Photons, although neutral, can interact via the electromagnetic force. In the presence of matter, they can split into an electron-positron pair, with a probability proportional to the density of the medium. These in their turn, if sufficiently energetic, emit Bremsstrahlung photons which can convert to more pairs of electrons and positrons, creating a shower of electromagnetically interacting particles. Thus for detection of photons, a sufficiently dense material is required to convert the photon into charged particles which can then be detected. Such a detector can also be used to identify and measure the energy of electrons or positrons, since a shower can be initiated by a Bremsstrahlung photon.

The measurement of particle energy works on the same principle as the identification of neutral particles. A particle is brought to rest inside the detector by means of an electromagnetic or hadronic shower and the total energy of its decay products is measured. For this reason, such detectors are known as calorimeters.

The ALEPH calorimeters are located in a barrel around the TPC and in two endcaps. The electromagnetic calorimeter is designed to stop and detect photons and electrons but not hadrons, which are stopped by the hadron calorimeter.

2.2.8 Electrons and photons: ECAL

The barrel section of the electromagnetic calorimeter, ECAL, is situated inside the superconducting coil and is a 4.8 m long cylinder with inner and outer radii of 1.85 m and 2.25 m respectively. The endcaps complete the solid angle coverage of 3.9π. The calorimeter is made up of 45 layers of lead and proportional wire chambers which together have a thickness of 22 radiation lengths. The wire chambers contain a gas mixture of 80 % xenon and 20 % carbon dioxide.

Signals from the anode sense wires are used for triggering, whilst position information is taken from the signals induced on the pads into which one cathode plane of each wire chamber is segmented. Pads from consecutive layers are connected into towers that point towards the interaction point, each with an angular coverage of about $0.9^\circ \times 0.9^\circ$. Every tower is further divided into three storeys, covering four, nine and nine radiation lengths each. The fine granularity of ECAL allows an angular resolution [24] of:

$$\sigma_\phi = \frac{\sigma_\theta}{\sin\theta} = (0.25 + \frac{2.5}{\sqrt{E/\mathrm{GeV}}})\,\mathrm{mrad}\,. \tag{2.2}$$

The energy resolution is estimated by comparing the measured energy to the momentum of the track and parameterised [24] as:

$$\frac{\sigma_E}{E} = 0.009 + \frac{0.18}{\sqrt{E/\mathrm{GeV}}}\,. \tag{2.3}$$

2.2.9 Hadrons and muons: HCAL and the muon chambers

The structure of the hadron calorimeter, HCAL, is similar to ECAL, with iron in place of lead and streamer tubes in place of multiwire proportional chambers. The barrel section is outside the superconducting coil and the iron provides a return path for the lines of magnetic flux. It is 7.3 m long with inner and outer radii of 3 m and

4.7 m respectively. This cylinder also acts as the mechanical support structure for ALEPH.

As with the electromagnetic calorimeter, the streamer tubes, filled with a gas mixture of 13 % Ar, 57 % CO_2 and 30 % C_4H_{10}, have cathode pads above the anode wires. These are again connected into projective towers pointing towards the interaction point, which give a granularity of about 3.7° × 3.7°. The energy resolution achieved is [24]:

$$\frac{\sigma_E}{E} = \frac{0.85}{\sqrt{E/\mathrm{GeV}}} \tag{2.4}$$

On the cathode plane opposite to the pads, a strip runs parallel to each wire so that the induced signals give a 2-dimensional picture in the $r\phi$ plane of the development of a shower. These patterns are very useful for identifying muons, which pass through the ECAL relatively undisturbed, being too heavy to emit much Bremsstrahlung, and yet do not interact strongly to produce showers in the HCAL.

Muon identification is completed by the muon chambers — two planes of double-layer streamer tubes lying outside ALEPH, 40–50 cm beyond the last layer of HCAL. They do not provide an energy measurement but give x and y coordinates for tracks, by means of strips on the two cathode planes.

2.2.10 Luminosity: LCAL, SICAL and BCAL

Determination of the luminosity is essential for some precision electroweak measurements. At LEP, this is done using elastic e^+e^- scattering at small angle (Bhabha scattering), the cross-section for which is known theoretically to high precision. The rate of such events is determined by simultaneous detection of the e^+ and e^- on opposite sides of the event and the luminosity is given by the ratio of the measured rate to the cross-section.

ALEPH has three luminosity monitors for detecting Bhabha events, situated close to the beam-pipe at either end of the detector. The most accurate of these is the silicon-tungsten luminosity calorimeter, or SICAL. Installed in 1992, it consists of two cylindrical units, situated 2.5 m outside ALEPH on either side. Each is made up of 12 alternating layers of silicon detectors and tungsten, covering the polar angle range $\theta = 24$–58 mrad. Use of SICAL data has permitted an experimental systematic below 0.1 % on the luminosity measurement.

Behind SICAL lies the LCAL, a lead/wire chamber device similar in design and operation to the electromagnetic calorimeter. It has a less accurate angular resolution than SICAL, which affects the luminosity measurement because the Bhabha cross-section is strongly dependent on angle. Thus, it was of lesser importance during the later part of the LEP I phase.

Finally, there is a very small angle luminosity calorimeter, BCAL, about 7.7 m from the centre of ALEPH on either side, beyond the LEP magnetic quadrupoles. It covers the polar angle region 5–9 mrad, where the Bhabha rate is 20 times higher than that seen by LCAL. However, since the field of the quadrupoles changes during LEP operation, the polar angles of the electrons are not precisely known and BCAL cannot be used for the offline luminosity. Instead, the observed rate is compared to that of SICAL or LCAL for calibration and is used for an online luminosity measurement.

2.2.11 Selection of events: the trigger system

In order to make use of a detector, information from all its components must be collected and stored, then combined to make a complete picture of each event. In most cases, timing constraints dictate that not every collision can be recorded, so that a trigger system is necessary to select which will be chosen.

The ALEPH trigger was designed to accept any Z^0 decay, whilst reducing background to a manageable level. It is important to do this with the minimum amount of dead time — the time during which a new event cannot be recorded because the detector is being read out. Thus, the trigger design was influenced by two timescales: the interval between bunch crossings ($11\,\mu$s for eight-bunch operation) and the time taken to read out the detector (determined in ALEPH by the time taken for ionisation electrons in the TPC to drift from the centre to the endplates).

In order to achieve these aims, the trigger is organised in three levels. The first is based on information from the ITC, ECAL and HCAL and its decision is available within about $5\,\mu$s so that a rejection at the first level does not introduce any dead time. Acceptance of an event initiates its digitisation and prevents the TPC gating grid from closing, so that the ionisation electrons which are already drifting towards it (as described in Section 2.2.3) will be accepted. Hadronic events, used by the analysis presented here, are selected by one or more of the following triggers:

- Total-energy trigger: ECAL energy greater than 6.5 GeV in the barrel region or greater than 3.8 GeV in either endcap or greater than 1.6 GeV in both endcaps simultaneously.

- ECAL-ITC coincidence: energy greater than 1.3 GeV in an ECAL module in the same azimuthal region as an ITC track candidate.

- HCAL-ITC coincidence: a particle penetrating HCAL consistent with an ITC track candidate in the same azimuthal region.

The second level trigger replaces ITC track information with that from the TPC, analysing the signals during the drift time itself so that a decision is made within $60\,\mu$s. If the event is rejected, the detector is reset and ready to accept data five bunch crossings (two in four-bunch operation) after the one which triggered at the first level. If the event is accepted by the second level trigger, full readout of the detector is initiated.

By this stage, the event rate has been reduced to less than 10 Hz. The third level trigger performs a partial reconstruction of the event and reduces the event rate to about 1 Hz, acceptable for data storage. The redundancy of the trigger types allows the total efficiency for hadronic events to be calculated. It is found to be greater than 99.99 % with an uncertainty of less than 0.01 % [24].

2.2.12 Collecting the data: the data acquisition system

After an event has been accepted by the trigger (in ALEPH, by the second level trigger), the detector information must be read out and stored. The ALEPH data acquisition system was designed to make each subdetector autonomous during development and running. A hierarchical structure was adopted so that information is fed downstream or upstream from each readout component, without communication between components at the same level.

After data acquisition is initiated, data flows from the front-end electronics to a subdetector Event Builder and thence to the Main Event Builder, or MEB. Each subdetector reads out at a different speed, so that data-flow is asynchronous to the MEB, which synchronises the event information and checks that it is complete. It is then passed to the third level trigger, which performs data reduction as well as functioning as a trigger. Finally, data is passed to the Main Host computer where it is stored and held available for online analysis and monitoring of detector performance.

This system means that whilst a given stage is analysing data from one event, the component downstream can be reading out the next event and the component upstream is still processing the previous event. Thus, dead time is minimised, allowing the ALEPH detector to record a total of around 4.9 million Z^0 events during the 1992–95 period of LEP I running.

2.2.13 Reconstructing the events: JULIA

The raw information collected by the data acquisition system must be processed to provide a picture of the tracks and energy depositions in an event. In ALEPH, this task is performed by a dedicated computer system (FALCON), using a package known as JULIA which carries out the following:

- Reconstruction of charged tracks, described in section 2.2.2.
- Analysis of the dE/dx associated with these tracks using information from the TPC wires.
- Reconstruction of the primary vertex and V^0 candidates (a V^0 is a neutral particle decaying into two charged ones).
- Clustering of energy deposited in the calorimeters and performance of an energy flow analysis.
- An analysis to identify muons, electrons and photons.

This event reconstruction takes place quasi-online, within a few hours of the time when the event occurred.

Figure 2.8 shows a hadronic event collected by ALEPH. On one side, a B_S decay into $\psi'\phi$ has been reconstructed. The main picture shows all of the detector components with the reconstructed tracks in the TPC and the energy deposits in the calorimeters (shown as histograms). The hits in the muon chambers are shown as stars. The right-hand picture shows a close-up around the interaction point (IP). The displaced secondary vertex where the B_S decayed can be clearly seen.

2.2.14 Event simulation

The production of simulated Monte Carlo events is necessary for many analyses, including the one presented in this thesis. A brief description of the ALEPH simulation procedure for hadronic events is given here. It is a two-stage process. First, the Z^0 decay is generated, including the production and decays of all the particles involved. Then, the response of the detector to those particles must be simulated.

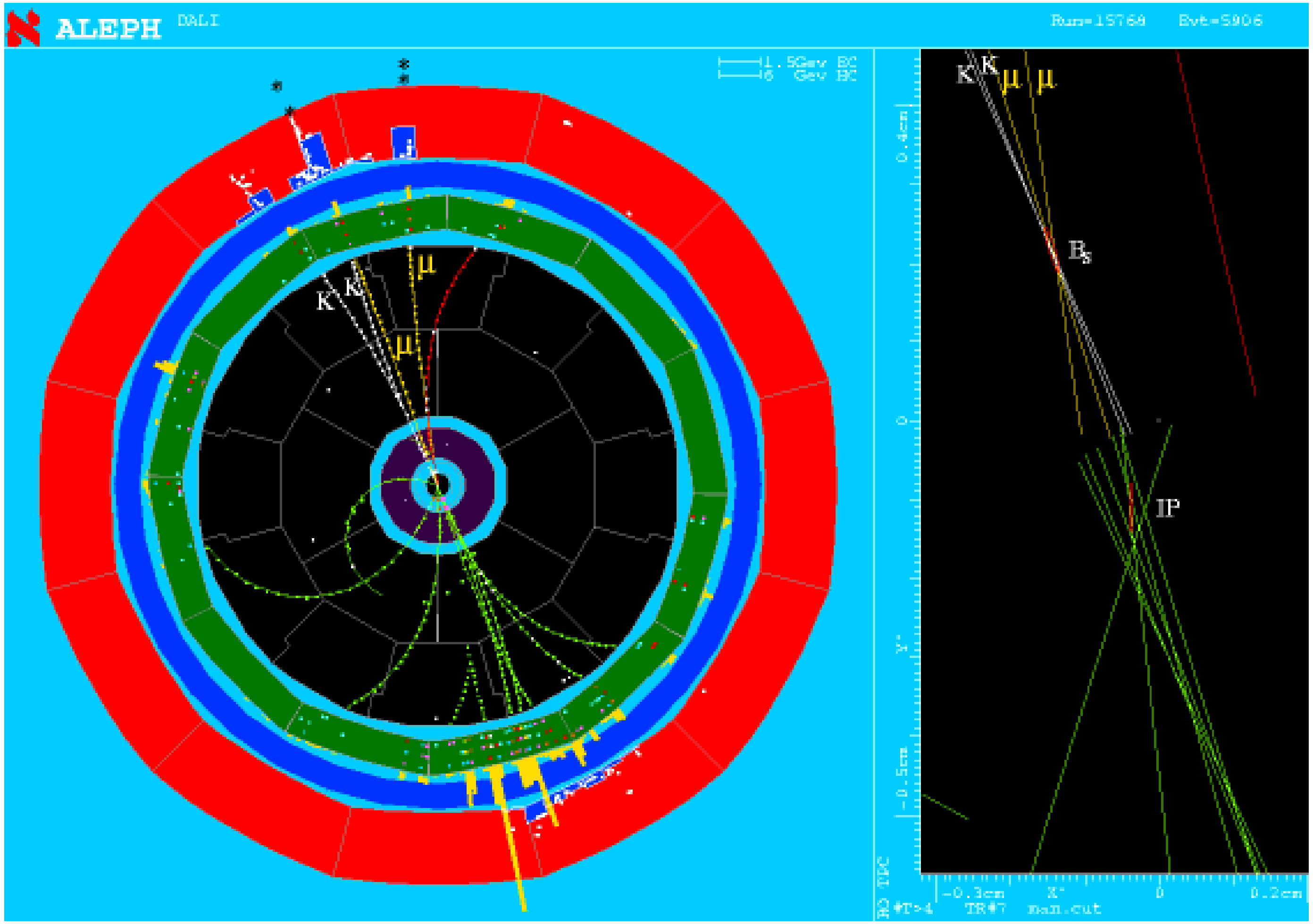

Figure 2.8: *A* $b\bar{b}$ *event collected by ALEPH. The decay of a* B_s *meson has been reconstructed in one hemisphere. The picture on the right shows a close-up view of this, with the displaced secondary vertex (marked* B_s*) and the primary vertex (marked IP) shown as red ellipses.*

Hadronic event generation in ALEPH is based on the Lund package JETSET 7.3 [11,12] (JETSET 7.4 was used to produce Monte Carlo simulating the 1994 data), with parameters tuned to fit event-shape variables [25]. The means by which this package simulates hadronic Z^0 decays is described in Section 1.1.4. The DYMU2 generator [26] is interfaced with JETSET to give a more accurate simulation of the $e^+e^- \rightarrow q\bar{q}$ process. The simulation of initial state radiation in this package has been optimised for electroweak physics. ALEPH has also developed a set of modifications to the basic JETSET package which are designed for heavy flavour studies. Several of JETSET's heavy flavour parameters, such as the decay rates of charmed hadrons, are altered to conform to more recent measurements. These modifications are known as HVFL and are described in [27].

Once a Z^0 decay has been generated, the charged and neutral particles are followed through the ALEPH detector, producing an output with the same formal structure as real data events. This is done using a program known as GALEPH, which is based around the GEANT package [28] and simulates the interactions of the particles with the detector material, taking into account detector geometry and magnetic fields. The responses and efficiencies of the different subdetectors are tuned to match the data. An example of such tuning, used in the simulation of the VDET, is given in Section 3.2.

The simulated events are reconstructed with the same packages as are used for the real data. Since features of the detector change from year to year, new Monte Carlo is produced for each year of data taking, simulating the detector as it was during that period. The latest measurements of tuned parameters such as branching ratios are also incorporated into each year's Monte Carlo production.

2.3 Summary

The LEP accelerator was designed to study the electroweak gauge bosons, $W^\pm$ and Z^0. The data analysed in this thesis was collected during the first phase of operation, when electrons and positrons were collided with a centre of mass energy around the mass of the Z^0. Studying these collisions are four experiments, of which ALEPH is one.

The ALEPH detector was designed to study e^+e^- collisions up to centre-of-mass energies of 200 GeV. Its main features are the hermeticity and fine angular granularity of the calorimeters and the accurate momentum and vertex resolution of the tracking detectors. This tracking system includes the world's largest time projection chamber and until 1995 contained the world's first double-sided silicon vertex detector. Lepton identification, using information from the TPC, the calorimeters and the muon chambers is also very efficient. The comparatively weak point of ALEPH is hadron identification and the separation of pions, kaons and protons. Nevertheless, an accuracy is achieved which is sufficient for many analyses.

The analysis presented in this thesis makes use of the strongest point of ALEPH, the tracking system. In particular, the excellent impact parameter resolution made possible by the vertex detector is used in the identification of $Z^0 \to b\bar{b}$ events.

Chapter 3

The ALEPH vertex detector

The analysis presented in this thesis relies heavily on the silicon vertex detector, or VDET, which permits accurate determination of track impact parameters. The long lifetime and hard fragmentation of b quarks means that the decay products of B hadrons tend to have large impact parameters. Thus, b events can be separated from charm and light quark events by the use of lifetime tags such as those described in Chapter 5. The first ALEPH vertex detector is described in Section 3.1 .

Section 3.2 discusses the Monte Carlo simulation of the vertex detector. Accurate understanding and simulation of the VDET and its efficiency is crucial to the control of systematic errors in the measurement of R_b, as demonstrated in Chapter 7. Whilst studying the simulation of vertex detector efficiency, a fault was found in the reconstruction algorithm used for data collected during 1993. When this fault was rectified, by repeating the reconstruction with a new version of the algorithm, the efficiency to tag $Z^0 \to b\bar{b}$ events rose significantly and agreement between data and Monte Carlo improved. Care was taken to ensure that the 1994 production of Monte Carlo included an accurate simulation of the vertex detector efficiency. Although it did not prove possible to reproduce the average efficiency perfectly, the simulation of defects and dead regions in the detector was improved.

The upgrade of the ALEPH vertex detector was undertaken in order to improve the efficiency for tagging hadrons containing b quarks. Although the analysis described in this thesis used data collected with the first VDET, which was in use from 1991 to 1995, a substantial part of the author's work has been directed towards the vertex detector upgrade. Section 3.3 describes this work, outlining the aims of the upgrade and the contributions made by the author, then concluding with a brief summary of the performance of the new detector since it was installed in ALEPH, in October 1995.

3.1 The first ALEPH vertex detector

A silicon detector is essentially a reverse-biased diode. When a charged particle passes through, electrons and holes are released into the conduction band and drift with the biasing field to the surfaces of the detector. Here, metallic readout strips allow the charge pulses to be observed. The positions of the strips on which the charge was deposited indicate the place where the track passed through the detector.

The original ALEPH vertex detector was the world's first double-sided silicon detector. Both sides of the silicon had readout strips. On one side, these ran parallel to the beam-pipe, providing a ϕ coordinate for the track, whilst on the other they were tangential, providing a z coordinate for the track. The third dimension, r, was provided by the known radial position of the silicon. With a length of 20 cm, the VDET inner layer could be hit by tracks making an angle θ to the beampipe such that $|\cos\theta| < 0.85$ and the outer layer by tracks for which $|\cos\theta| < 0.69$.

Figure 3.1 shows a schematic diagram of the first VDET. It was arranged in two concentric, coaxial layers. The inner layer had nine faces and an average radius of 6.5 cm, while the outer lay at an average radius of 11.3 cm and contained 15 faces. Each face was made up of two modules placed end to end. A module consisted of two silicon wafers with dimensions 51.2×51.2 mm and thickness $300\,\mu$m. Each strip running parallel to the beam-pipe (the $r\phi$ strips) was connected to the equivalent strip on the other wafer of the module. This arrangement, known as daisy-chain bonding, gave the effect of long strips running the full length of the module. The readout chips for the $r\phi$ strips were situated at the outside end of each module. For the z strips, the readout chips were glued on top of the silicon wafers and lay along the length of the detector.

The separation of the readout strips on both sides of the detector was $100\,\mu$m. A position resolution of $12\,\mu$m could be obtained in both $r\phi$ and z views by interpolating the charge distribution found on adjacent strips.

3.2 Simulation of vertex detector efficiency

The simulation of the ALEPH detector response, described in Section 2.2.14, includes effects such as noise and the presence of inactive areas at the edges of VDET wafers. It is then necessary to simulate the effects of dead, inefficient and misbonded strips, which in the data may prevent a hit from being recorded. This is done by randomly

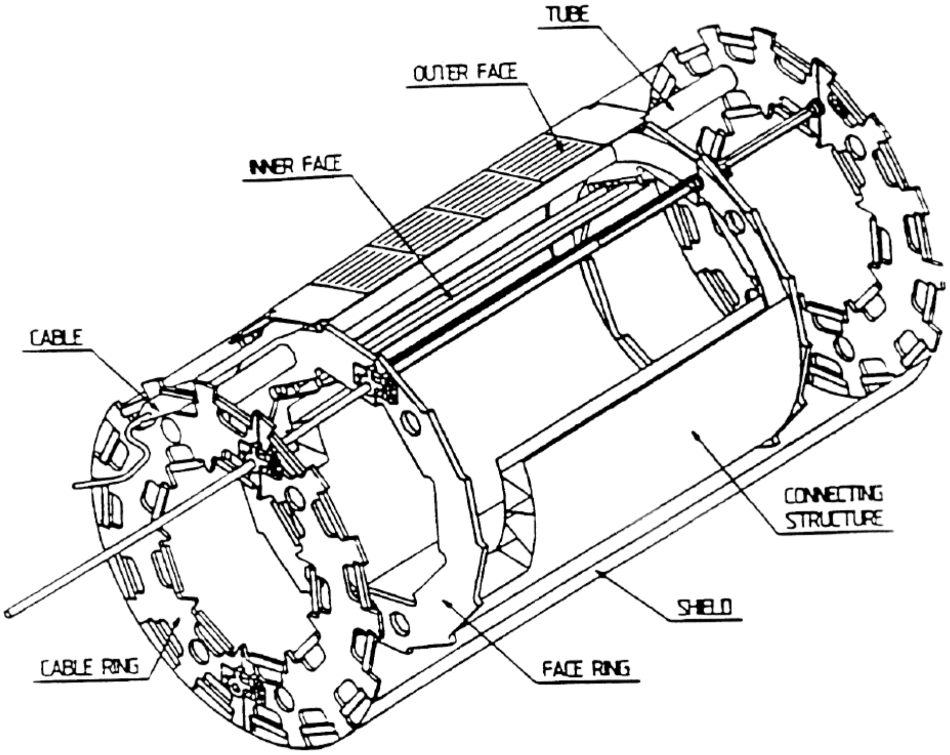

Figure 3.1: *Schematic representation of the first ALEPH VDET.*

ignoring a proportion of hits according to their position in the vertex detector, using a map derived from the data. This map is produced as a function of position in the VDET and time, as modules become defective and are repaired during the data taking period. Monte Carlo events are produced for each time period in the same proportions as are found in the data.

The philosophy behind the production of the efficiency maps changed between the production of Monte Carlo simulating the 1992 and 1993 data taking periods and the production of the 1994 Monte Carlo. Before 1994, discrepancies between module efficiencies in data and Monte Carlo were assumed to derive from dead readout chips. Every VDET module had six line drivers — two for the $r\phi$ readout and four for z. Since each line driver was connected to four readout chips, their efficiency was taken to be quantised ($0\,\%, 25\,\%, 50\,\%$ or $100\,\%$). Any remaining discrepancies after this quantisation were assumed to be due to dead or inefficient strips. This was accounted for by globally reducing the efficiency of a line driver connected to four functional readout chips, so that on average the Monte Carlo efficiency matched that found in the data. In contrast, after 1994 the first step in the process was to apply to the Monte Carlo a list of VDET strips known to be dead or inefficient and of readout chips known to be dead. After this, it was still necessary to apply a correction to the overall Monte Carlo efficiency so that it matched the data. This was performed on a wafer-by-wafer basis.

When the efficiency of a line driver is calculated for constructing the maps, a track is considered to have recorded a VDET hit if one is found within 2 mm ($r\phi$ view) or 8 mm (z view) of the track. However, the tracking procedure requires a hit to fall much closer than this to the track before the two can be associated. Thus, even though the efficiency map is derived from the data, there is usually a discrepancy between data and Monte Carlo in the number of tracks with which VDET hits have actually been associated.

As described in Chapter 7, one of the major contributions to the systematic error in the measurement of R_b is the simulation of the vertex detector. In particular, events in the Monte Carlo simulation tend to include too many tracks with which VDET hits have been associated. One reason for this is the non-Gaussian tails in the position resolution function of the VDET. These are hard to simulate exactly in the Monte Carlo, which in general has too few hits falling in the tails of the distribution, far away from the tracks which caused them. Thus, it is more often the case in data than in Monte Carlo that the distance between a track and a hit is too large to allow them to be associated by the tracking procedure but small enough to allow them to be matched when constructing the efficiency map. There are many other factors which can influence the probability that a VDET hit will be associated with the hit which caused it. For example, in addition to the intrinsic resolution of the VDET, the resolution of the TPC will have an effect.

Whilst investigating the probability that a track would be associated with a VDET hit in data and in Monte Carlo, a fault was discovered in the reconstruction algorithm used for data collected in 1993. This fault reduced the efficiency of track-hit association and affected Monte Carlo and data in different ways.

3.2.1 Fault in reconstructing 1993 data

When events from the 1993 data taking period were processed, there was a subtle problem in the reconstruction procedure. This affected the routine which associates

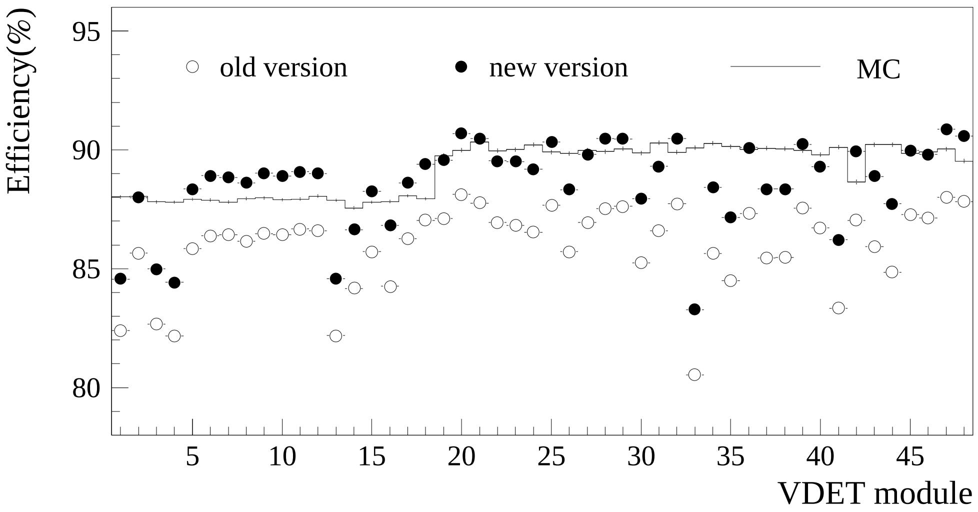

Figure 3.2: *Efficiency of associating a track with a hit in the VDET $r\phi$ view in 1993. Data points are shown with (old version) and without (new version) the fault in the reconstruction algorithm. Monte Carlo (MC) with the old version of the algorithm is shown as a histogram.*

hits in the VDET with tracks reconstructed from hits in the TPC and ITC. Parameters used in the association were incorrectly read from a data-base, with the net result that the probability of linking a track to a VDET hit was reduced. Figure 3.2 shows this for hits in the $r\phi$ view and there was a similar effect in the z view. This feature had been deliberately introduced into the reconstruction of the 1993 Monte Carlo simulation, in an attempt to compensate. The effect of the fault on the efficiency to tag b events can be seen from Figure 3.3. The improvement seen with the new version of the algorithm is due to the better impact parameter resolution for tracks with more VDET hits.

By its nature, the fault mostly affected tracks which fell into the non-Gaussian tails of the resolution distribution. Since these tails are poorly understood and hard to model, it might be expected that tracks from real and simulated events would be affected to different extents. Indeed, when a sample of Monte Carlo was reprocessed using a new version of the algorithm (without the fault), the increase in the number of tracks with associated VDET hits was much less marked than the corresponding increase in data (Table 3.1).

To rectify the fault, the affected data was reprocessed using the new version of the reconstruction algorithm. However, due to time constraints and the need to produce

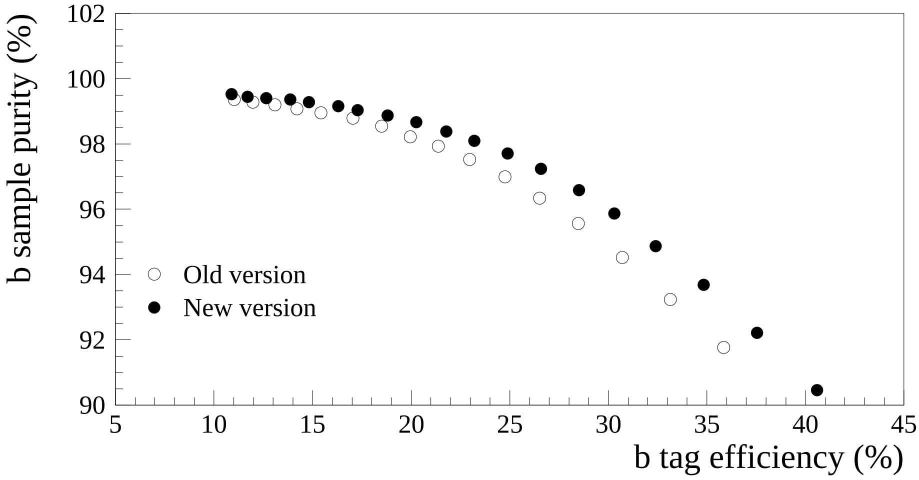

Figure 3.3: *b-tag purity as a function of efficiency, with (old version) and without (new version) the fault in event reconstruction.*

Monte Carlo simulation of the 1994 data, the 1993 Monte Carlo sample has not yet been reprocessed. Nonetheless, as can be seen from Figure 3.2, the data reprocessed with the new version of the algorithm (shown as dark circles) and the Monte Carlo processed with the old version (shown as a histogram) are in good agreement, at least in the respect of average module efficiency.

The reasons for reprocessing the data with a new version of the reconstruction algorithm were two-fold. Firstly, the improvement in the purity of the b-tag at a given efficiency reduces the background from charm and light quark events. This

Average probability			
		Data	Monte Carlo
VDET inner layer	old version	0.797 ± 0.001	0.831 ± 0.001
	new version	0.833 ± 0.001	0.853 ± 0.001
	Δ	$(4.5 \pm 0.05)\,\%$	$(2.6 \pm 0.05)\,\%$
VDET outer layer	old version	0.780 ± 0.001	0.826 ± 0.001
	new version	0.820 ± 0.001	0.848 ± 0.001
	Δ	$(5.1 \pm 0.06)\,\%$	$(2.6 \pm 0.05)\,\%$

Table 3.1: *Average probability for a track to have a spacepoint hit in 1993 data and Monte Carlo test samples, with old and new versions of the reconstruction algorithm. The difference between the versions is shown as Δ.*

reduces the systematic errors due to uncertainties which propagate through these backgrounds to give an error on R_b. Secondly, the improved agreement between data and Monte Carlo reduces the systematic error originating from uncertainties in detector simulation. One of these uncertainties is in the number of tracks which are associated with hits in the VDET. It is estimated from the discrepancy between data and Monte Carlo, before correcting the Monte Carlo so that the two agree. Thus, improving the agreement between data and Monte Carlo can lead directly to a reduction in the systematic error.

3.2.2 Improvements in simulation

After discovering the fault in the 1993 data reconstruction, it was natural to examine how the production of Monte Carlo to simulate the 1994 data could be improved. There were two aspects of the simulation of VDET efficiency in the Monte Carlo which needed to be taken into consideration. The overall normalization of the distribution is given by the average efficiency in data or Monte Carlo. This determines the total number of tracks associated with VDET hits. The comparative shapes of the efficiency distributions in the data and Monte Carlo (regardless of overall normalization) show how well efficiency fluctuations are reproduced. This indicates how well dead or inefficient modules are modelled in the VDET simulation.

Figure 3.4 compares the probability in data and Monte Carlo that a track passing through a given VDET wafer will record a hit in the $r\phi$ view, for 1994. It can be seen that although the efficiency normalization is overestimated in the Monte Carlo, reproduction of the shape of the efficiency distribution is good. This contrasts with the situation in 1993, shown in Figure 3.2, where the reprocessed data (dark circles) should be compared to the Monte Carlo (histogram). It can be seen that, although the average efficiency found in the data was reproduced by the Monte Carlo, the shape of the efficiency distribution was not well simulated. This improvement in the simulation of dead and inefficient regions of the VDET is due to the changes to the mapping process described at the beginning of Section 3.2.

The agreement between 1994 data and Monte Carlo for the overall efficiency normalization in the z view is much better than in the $r\phi$ view. It did not prove possible in the timescale available to find an explanation for the overestimation of the $r\phi$ efficiency. Interestingly, the probability that a VDET hit was matched to a track for creating the efficiency map agreed well between data and Monte Carlo. As men-

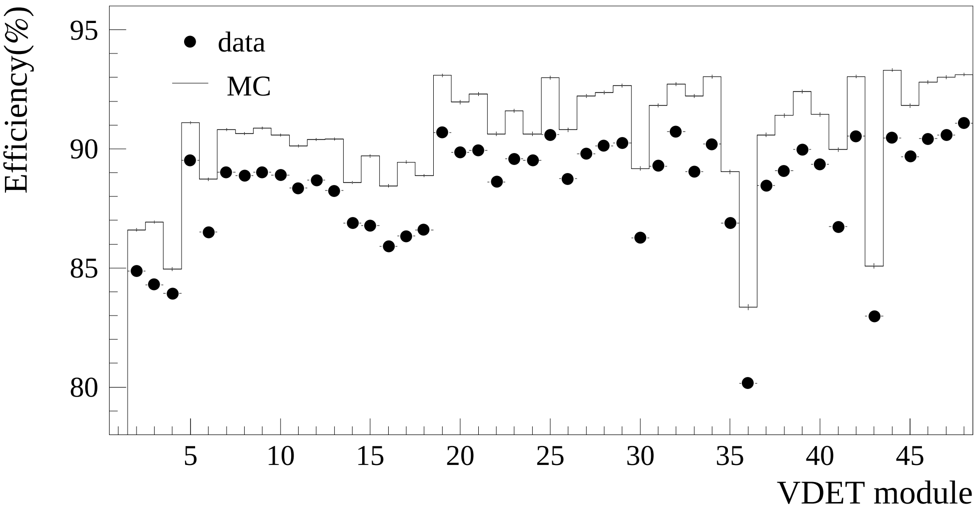

Figure 3.4: *Efficiency of associating a track with a hit in the VDET $r\phi$ view in 1994. Data is shown as points and Monte Carlo (MC) as a histogram.*

tioned in above, this matching has much looser requirements than those of the track reconstruction algorithm. One possible explanation for the discrepancy found when the tighter cuts for tracking are applied is that there are problems in the simulation of other parts of the detector. Alternatively, the problem could be linked to the non-Gaussian tails of the VDET resolution function.

3.3 The vertex detector upgrade

The aim of the ALEPH vertex detector upgrade [29,30] was to improve the efficiency for detecting particles containing b quarks. The first vertex detector, described in Section 3.1, performed well but had several limitations:

- Restricted angular coverage. Only tracks at more than 46° to the beam-pipe crossed both layers of the detector. The new detector has the same geometrical layout as the old, with two layers made up of several faces where a face consists of two modules laid end to end. However, the number of silicon wafers in a module has been increased to three and the length of each face is now about 40 cm, so that tracks with a polar angle greater than 29° pass through both layers.

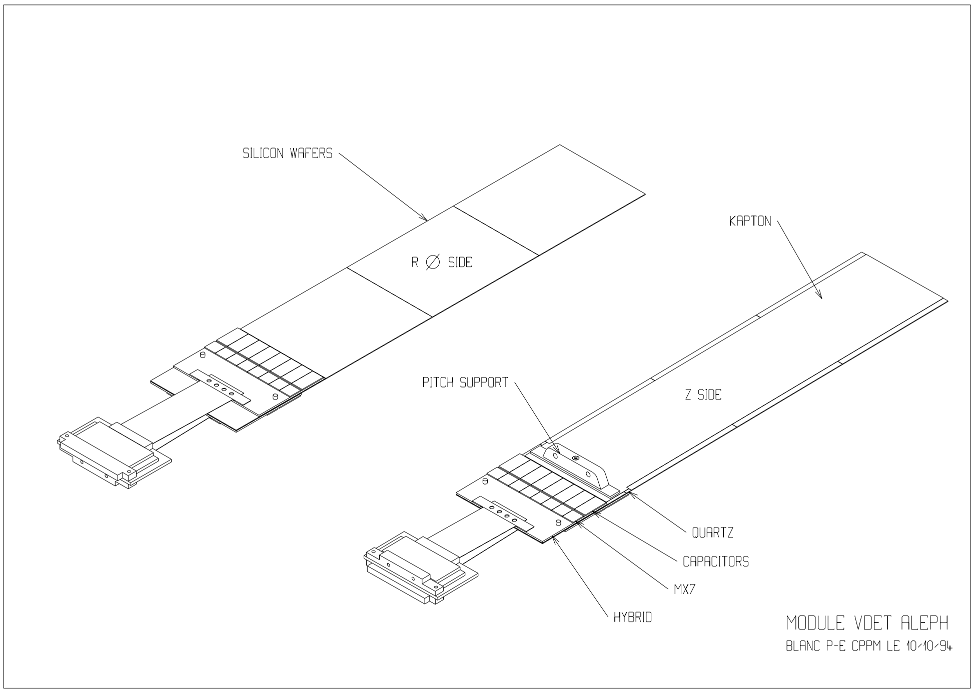

Figure 3.5: *Schematic representation of a module from the new VDET.*

- The readout electronics for the z side were situated along the length of the detector. This extra material in the sensitive region of the detector, along with its non-uniform distribution, degraded the impact parameter resolution. In the new detector the z readout electronics have been moved to the ends of the detector, close to the $r\phi$ readout.

  The new arrangement is made possible by the fanout: metallic tracks on a piece of kapton which is glued to the z side of the module. The strips are bonded to these tracks, which are in turn bonded to the readout chip. In order to allow 1920 strips in the z view to be read out by a chip of reasonable size, a multiplexing system is used. This maps two strips, 10 cm apart, onto each readout channel.

- The lack of radiation tolerance in some components. Some parts of the readout electronics were vulnerable to the radiation bursts which can occur when LEP beams are lost. Thus, the upgraded detector makes use of radiation-hard electronics. Radiation damage studies have indicated that the lifetimes of the new electronics will be in excess of the LEP period of operation.

It was planned that one third of the modules for the new vertex detector would be assembled and tested at Imperial College. Automation of the major stages in this procedure was important in order to maximise efficiency and reproducibility and to minimise the potential for human errors. For this purpose, two programs were written following algorithms described here. The first was to automate the alignment of silicon wafers for gluing. The second was to run on a Macintosh computer and control a light-spot testing station for the completed modules.

3.3.1 Module assembly

Each module of the new vertex detector consists of three silicon wafers, attached to a quartz substrate and glued together with edges parallel to within $5\,\mu$m in $5\,$cm (approximately the length of one wafer). For gluing, the wafers were to be mounted on XY stages that allowed independent rotation and translation for each wafer. The position of each centre of rotation relative to the wafer was unknown.

The equipment used for the alignment is shown in Figure 3.6 . The silicon wafers were mounted on XY stages and were moved under the microscope, which remained fixed. Each corner of the wafer had a fiducial mark, whose positions relative to one another and to the rest of the wafer were accurately known. The stages were moved with an accuracy of about $7\,\mu$m using a stepper motor and their position relative to a preset origin was indicated with the same accuracy. Control was either manual, via buttons on the front panel of the controller, or remote, via a Macintosh computer running the LabView package.

The first step in the procedure was to align the central wafer. The stage was rotated by hand to about 0° and the position of the fiducial marks measured. The positions of the marks were estimated by the Macintosh, from the known dimensions of the wafer and its approximate angle. The stages were then driven to bring each of these points in turn under the microscope. For each, the operator was asked to move the mark under the cross-hairs and the resulting accurate position was stored.

The stage was then rotated to approximately 45° and the new positions of the marks measured in the same manner. This gave two measured positions for each fiducial mark, one at each angle. From these and the known dimensions of the wafer, it is possible to deduce a set of conversion factors between the coordinate frame of the stages and that of the wafer. The position of the centre of rotation can then be deduced from the same data; four marks in fact allow it to be calculated several

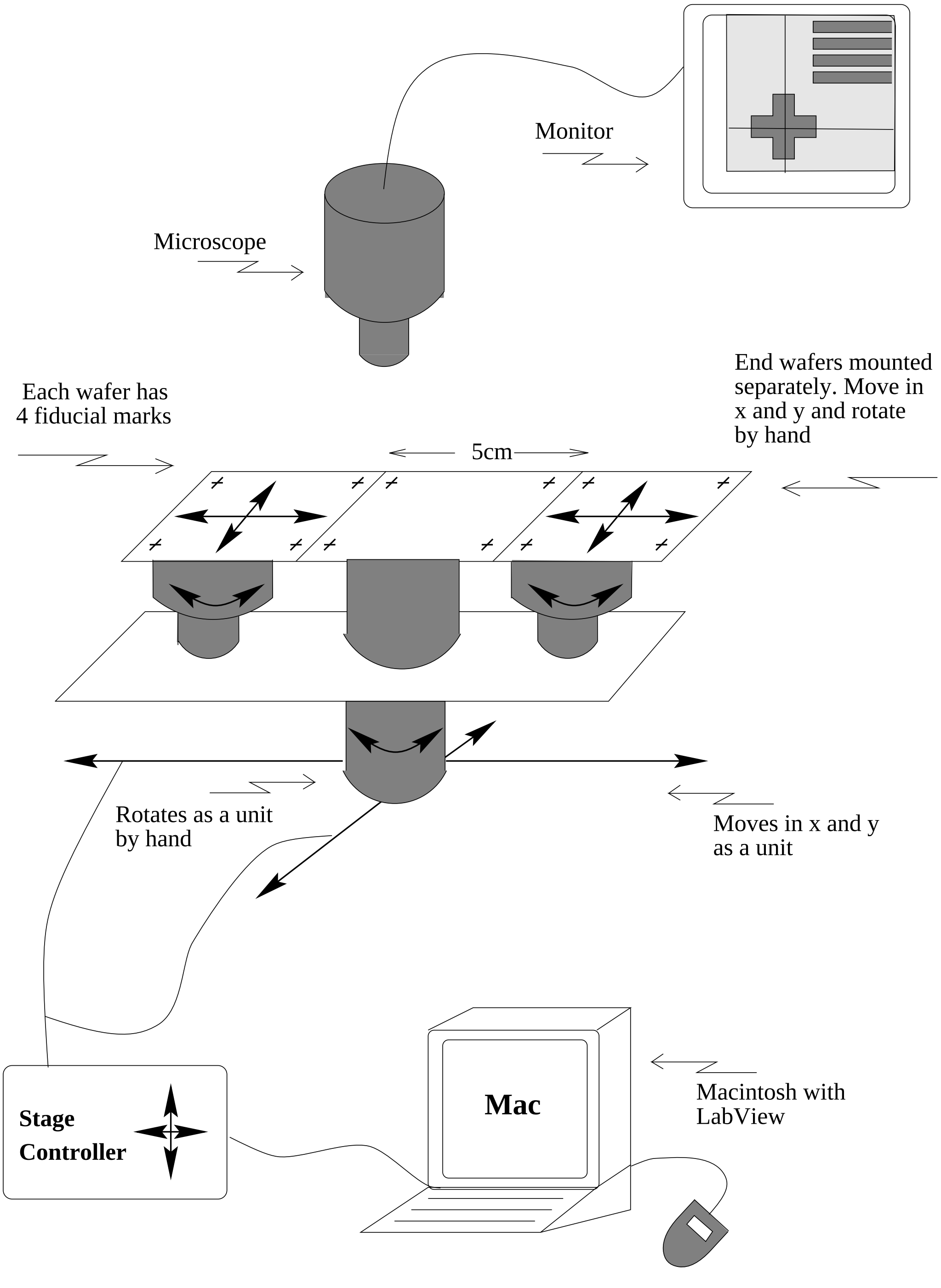

Figure 3.6: *Set-up for alignment of silicon wafers.*

times, providing an automatic check for error. If the values differed by too much (a standard deviation greater than 0.02 mm), the operator was asked to repeat the measurements. The angle of the wafer to the X stage was also calculated and the stages driven so that when the operator rotated the stage to bring the bottom left fiducial mark under the cross-hairs, the wafer was aligned at exactly 0°.

The procedure could then be repeated for the outer wafers. First the small stage on which the wafer was mounted (Figure 3.6) was wound out to its furthest extent. This did not leave enough gap between the edges for the small stage to be rotated through 45°, so instead the measurements were made at ±5°. The wafer was aligned to 0° on the small stage, which was then wound in so that the fiducial marks on the outer and central wafers were at a preset separation. This was done on the same principle as the rotation to 0°: the stages were driven to the calculated position under remote control and the operator was asked to wind the stage in until the mark is under the cross-hairs.

This algorithm worked consistently to the design specification (5 μm over 5 cm). It minimised the possibility of operator error and limited the number of stage movements necessary. In the event, however, no gluing of modules took place at Imperial College so that whilst this algorithm was fully tested, it was not possible to implement it in a production phase.

3.3.2 Module testing

Once the modules had been assembled, it was necessary to test them. An automated system of light-spot testing was used to map the bonding and to find shorted and noisy strips. This section describes a LabView program that was written to form part of such a testing system. It worked together with a set of routines running on a VME based microprocessor (FIC) to control and read out data from the hardware involved.

The experimental set-up is shown in Figure 3.7 . A pulsed infra-red laser spot was focussed through a microscope lens onto one or two strips of a silicon detector that was mounted on XY stages. Photons created electron-hole pairs in the silicon, which could be detected as charge pulses on the illuminated strips and read out using a VME Sirocco and the FIC. The detector readout was synchronised with the signal by using the same pulse for the laser and the sequencer. In order to prevent unnecessary noise, the microscope, detector and stages were enclosed in a light-tight box. The FIC and the XY stages were controlled by a Macintosh computer running the LabView

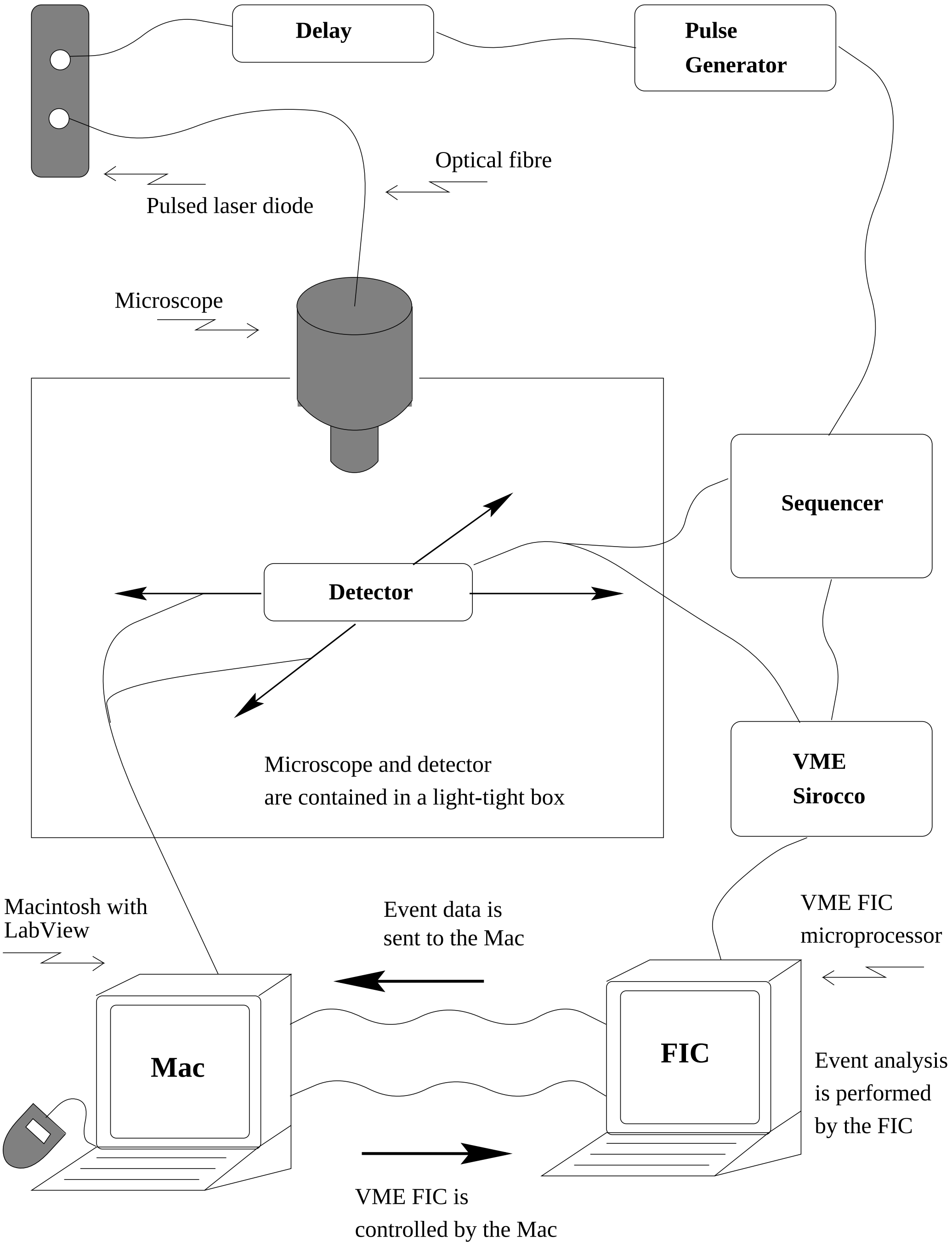

Figure 3.7: *Set-up for module testing.*

package.

When instructed by the Macintosh, the FIC read out all the strips on the detector, made corrections for possible common mode fluctuations and searched for the strip with the highest signal to noise ratio. It then sent the Macintosh an array containing the strip numbers of this strip and the two on either side, followed by the signal to noise ratio for each of the five. These numbers, along with the position of the stages were written to a file for later offline analysis. The stages were then moved under remote control to a new position and the process repeated.

To check this procedure, it was repeated for 1000 iterations, using a small test detector and a step size of $7\,\mu$m for the stage movement. The results of the offline analysis are shown in Figure 3.8. For each step, the hit position was reconstructed. This was done by averaging the positions of the hit strips, weighting each by the charge deposited. The expected hit position was also deduced, from the position of the stages. A graph of hit position versus stage position is linear, showing that the routine worked successfully.

The residual was defined as the difference between the actual and expected hit positions and a histogram was plotted of residuals from all the steps. The width of the Gaussian fitted to this histogram gave the resolution of the testing station, which was found to be $8\,\mu$m.

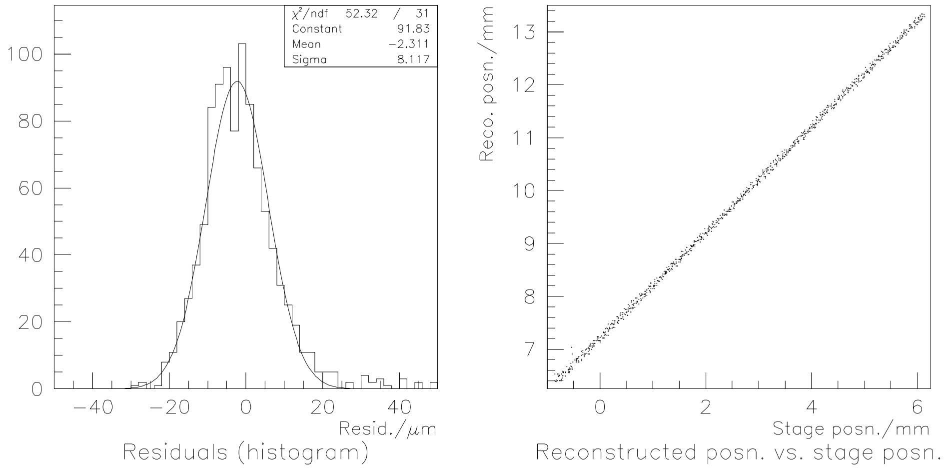

Residuals (histogram)

Reconstructed posn. vs. stage posn.

Figure 3.8: *Results from the light-spot testing station.*

Once the testing procedure had been developed, it was implemented to test the modules as they were produced. For this, both sides of the detector were tested and each strip on each wafer was scanned. Thus, every daisy-chain bond on the $r\phi$ side and silicon-kapton bond on the z side was tested, as well as the bonds to the capacitor and readout chips. The light-spot was scanned across the detector and the reconstructed and actual position at each point was recorded. Comparison of the two allowed noisy, dead, shorted or misbonded strips to be detected. This information was written to a data bank for use when the module was installed in ALEPH.

The procedure enabled 26 modules to be tested at Imperial College, at a rate of 2–3 a week. In addition, the system was duplicated at Glasgow and used to test modules there.

3.3.3 Performance of the upgraded detector

The upgraded vertex detector was installed in October 1995, at the end of the LEP I phase of operations. The resolution measured with $e^+e^- \to Z^0$ data taken for calibrations was found to be $10\,\mu$m in $r\phi$ and $15\,\mu$m in z, as shown in Figure 3.9.

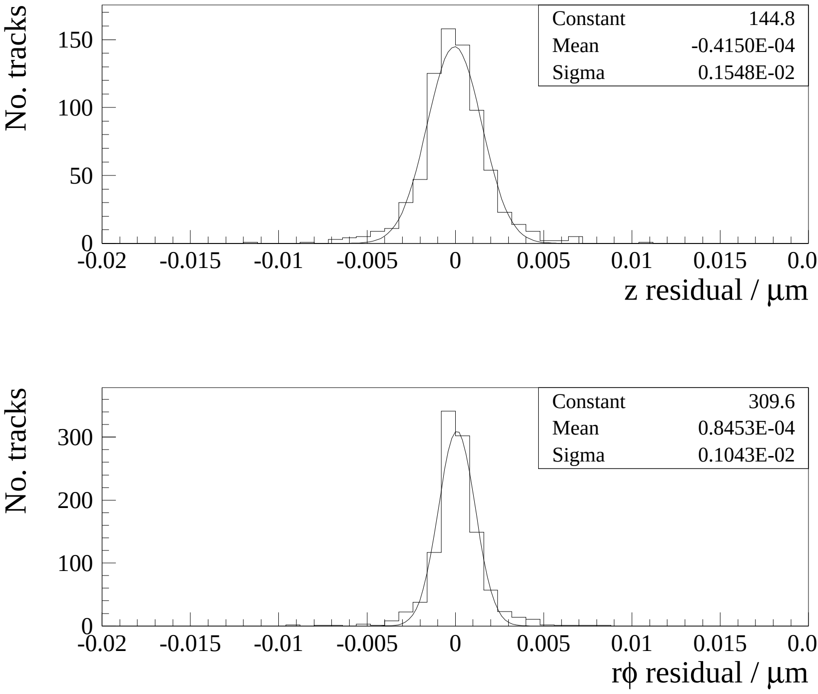

Figure 3.9: *VDET resolution in z (top) and $r\phi$ (bottom).*

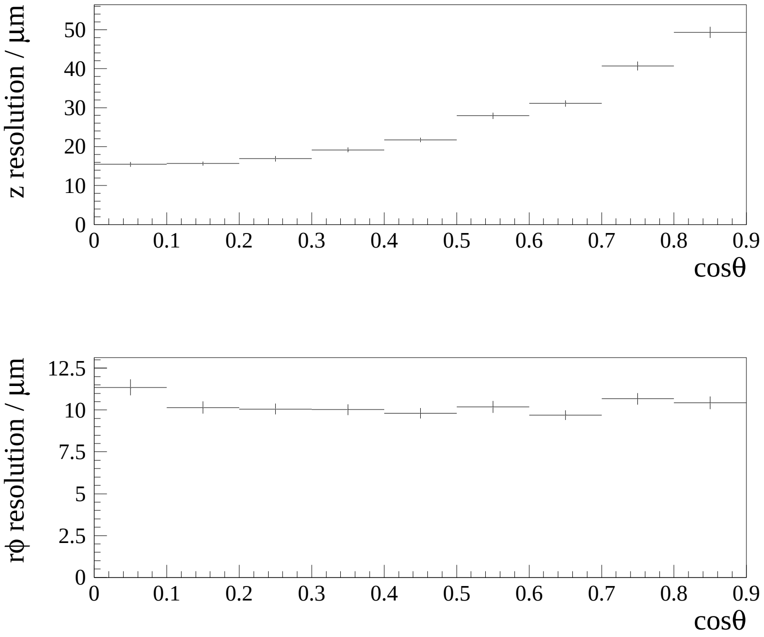

Figure 3.10: *VDET resolution versus* $\cos\theta$ *in* z *(top) and* $r\phi$ *(bottom).*

This measurement was made using tracks passing through the overlap regions between wafers, so that they record more than one hit in a single layer. The tracks were required to have a momentum greater than 2 GeV and for the z measurement to be perpendicular to the z axis. The resolution in z deteriorates rapidly as a function of $\cos\theta$, as can be seen from Figure 3.10. This is because at large polar angles, charge from the track is deposited on several adjacent strips and reconstructing the hit position becomes more difficult.

The equivalent resolutions with the old vertex detector were $12\,\mu$m in both $r\phi$ and z. The improvement in the $r\phi$ resolution is thought to be due to an improved signal-to-noise ratio and a better procedure for deducing the alignment of the VDET with respect to the rest of the ALEPH detector. The poorer resolution in z is thought to be due to a degraded signal-to-noise ratio, which is partly due to the presence of the kapton fanout.

3.4 Summary

The data analysed in this thesis was collected using the first ALEPH vertex detector (VDET), a double-sided silicon microstrip detector. In the Monte Carlo simulation of the VDET, a good understanding of its efficiency is necessary. This affects the estimation of systematic errors in the measurement of R_b. In the course of investigating the simulation of the vertex detector efficiency, a fault in the algorithm used to process the 1993 data was uncovered. When this fault was rectified by reprocessing the data with a new version of the algorithm, both the efficiency to tag b events and the agreement between data and Monte Carlo improved. Meanwhile, better simulation of dead and inefficient regions of the vertex detector was achieved for the Monte Carlo simulation of 1994 data. However, the simulation overestimates the efficiency for a track to be associated with a VDET hit in the $r\phi$ view.

In October 1995, an upgraded vertex detector was installed in ALEPH. Imperial College played a part in the upgrade project, including the development of some automated routines for assembly and testing of modules. The new VDET was designed to improve the efficiency to tag B hadrons by means of an improved angular coverage, a reduction of material in the sensitive regions of the detector and the use of radiation hard electronics.

Chapter 4

Measurement of R_b

This chapter describes the method by which a measurement of R_b, the branching fraction $\Gamma_{Z^0\to b\bar{b}}/\Gamma_{Z^0\to hadrons}$, is made. Section 4.1 outlines the double tag technique, which is used to derive both R_b and the efficiency for tagging b events from the data. Section 4.2 considers the statistical and systematic sources of uncertainty in the measurement. Finally, Section 4.3 discusses in more detail the hemisphere-hemisphere correlation in tagging efficiency, which is one of the largest sources of systematic uncertainty in the measurement of R_b.

4.1 The double tag technique

The method of measuring R_b in the analysis presented here makes use of the double tag technique. In this, hadronic events are selected and each is divided into two hemispheres by a plane perpendicular to the thrust axis. A b-tag is then applied to both hemispheres, so that each event has the potential to tag twice. The number of tagged hemispheres, N_s, the number of events in which both hemispheres have been tagged, N_d, and the total number of hadronic events, N_h, are used as inputs to the equations:

$$\frac{N_s}{2N_h} = R_b\epsilon_b + R_c\epsilon_c + (1 - R_b - R_c)\epsilon_{uds} \tag{4.1}$$

$$\frac{N_d}{N_h} = R_b\epsilon_b^2(1+\rho_b) + R_c\epsilon_c^2 + (1 - R_b - R_c)\epsilon_{uds}^2 \,. \tag{4.2}$$

Here, ϵ_b, ϵ_c and ϵ_{uds} are the probabilities of tagging hemispheres from b, c or uds events respectively, R_c is the ratio $\Gamma_{Z^0\to c\bar{c}}/\Gamma_{Z^0\to hadrons}$ and ρ_b is the correlation of tagging efficiency between hemispheres. This last is needed to correct for the fact that the probability of tagging both hemispheres of an event is not exactly ϵ_b^2. It is defined as:

$$\rho_b = \frac{\epsilon_b^d - \epsilon_b^2}{\epsilon_b^2} , \tag{4.3}$$

where ϵ_b^d is the fraction of b events in which both hemispheres are tagged. In principle, similar parameters should be included in the terms containing ϵ_c^2 and ϵ_{uds}^2, but as these are strongly suppressed by the small efficiencies to tag non-b events, such corrections are negligible.

All high-precision measurements of R_b now rely on the double tag technique, which avoids the need to know the absolute value of ϵ_b. The use of two equations allows both R_b and the efficiency, ϵ_b, to be derived from the data, thus removing what would have been the most significant component of systematic uncertainty in the measurement.

Small corrections must be made for the flavour dependence of the event selection cuts and the non-hadronic background. In addition, a small correction must be made to remove the contribution to the measured value of R_b from photon exchange. The expression:

$$R_b = R_b^{meas.} + 0.0003 \tag{4.4}$$

can be used to derive the pure Z^0 contribution [37].

4.2 Sources of uncertainty

With the double tag technique, the major potential contribution to the systematic error can be avoided, since there is no need to use Monte Carlo simulation for predicting the absolute efficiency to tag b hemispheres. The statistical error is increased, since it is dominated by the number of events in which both hemispheres have been tagged. Even so, using the LEP I data sample collected during 1992–95 by ALEPH, the statistical error in the measurement of R_b is significantly smaller than the systematic uncertainty.

The systematic errors involved in the measurement of R_b with the double-tag technique are almost entirely due to the need to predict the background efficiencies, ϵ_c and ϵ_{uds}, and the correlation, ρ_b, from Monte Carlo. Other errors arise from imperfect knowledge of the flavour bias in the selection of hadronic events and of the non-hadronic background, but these are small in comparison with the other uncertainties. R_c can be taken either from the Standard Model predicted value or an experimentally determined one.

The uncertainties in the values of ϵ_c, ϵ_{uds} and ρ_b propagate to uncertainties in the measurement of R_b as shown below. The variation of the measured value of R_b with the value assumed for R_c is also shown.

$$\Delta R_b = \frac{-2R_c(\epsilon_b - \epsilon_c)}{(\epsilon_b - \epsilon_{uds})^2} \cdot \Delta\epsilon_c \tag{4.5}$$

$$\Delta R_b = \frac{-2(1 - R_b - R_c)}{(\epsilon_b - \epsilon_{uds})} \cdot \Delta\epsilon_{uds} \tag{4.6}$$

$$\Delta R_b = \frac{R_b\epsilon_b^2}{(\epsilon_b - \epsilon_{uds})^2} \cdot \Delta\rho_b \tag{4.7}$$

$$\Delta R_b = \frac{-2(\epsilon_b - \epsilon_{uds})(\epsilon_c - \epsilon_{uds}) + (\epsilon_c - \epsilon_{uds})^2}{(\epsilon_b - \epsilon_{uds})} \cdot \Delta R_c \tag{4.8}$$

One of the largest sources of systematic error in the measurement of R_b is imperfect simulation of the detector resolution and efficiency. This propagates mainly through uncertainty in the value of ϵ_c, but also has an effect through the prediction of ϵ_{uds} and ρ_b. Less important is the effect of imperfectly known physics input parameters needed for the Monte Carlo simulation. This again propagates mainly through its effect on ϵ_c and to a lesser extent through its effect on ϵ_{uds}. In addition, the choice of the physics parameters in b events changes ρ_b due to its dependence on ϵ_b, so that the uncertainty propagates through to R_b.

Finally, as discussed in Section 4.3, the hemisphere-hemisphere efficiency correlation, ρ_b, depends on factors such as the orientation of the event within the detector and the reconstruction of the primary vertex. These effects and the interplay between them may be different between data and Monte Carlo and it is important to allow for such discrepancies when calculating the systematic error on ρ_b. This approach accounts for factors not covered by varying the physics input parameters for b events in the Monte Carlo. The error is then propagated through Equation 4.7 to give a systematic uncertainty in the value of R_b. In the analysis described here, this uncertainty in the value of the correlation contributes one of the largest sources of systematic error in the measurement of R_b.

All of these sources of uncertainty and the estimation of their effects on the value of R_b are discussed in detail in Chapter 7. The hemisphere-hemisphere correlation in b-tagging efficiency is considered in the following section.

4.3 Correlation

The hemisphere-hemisphere correlation, ρ_b, is the extent to which tagging an event in one hemisphere affects the likelihood that it will tag in the other. As an input to the measurement of R_b which must be predicted from Monte Carlo simulation, it is important to understand and to control as far as possible any systematic uncertainties in its value. In order to do this, the sources of correlation must be understood.

Naively, one might expect the probability of tagging an event twice to be ϵ_b^2. The reasons why this is not so fall into 3 categories:

- Geometrical acceptance.

  In the majority of events, the B hadrons are produced back-to-back, due to conservation of momentum. Since most detectors are cylindrically symmetrical, this means that if one B jet falls in a region where tracking is comparatively poor, then on average the other will do so as well. This introduces a positive correlation between tagging efficiencies in the two hemispheres.

- QCD effects.

  There are two principal sources of correlation due to gluon emission. In the first, a soft gluon is radiated, reducing the momentum of both B jets. This increases the multiple scattering of tracks in the jet and results in a positive correlation, since the poorer tracking resolution reduces the tag probability. Alternatively, in about 2 % of events, a hard gluon is emitted which forces both B hadrons into one hemisphere. The event is thus likely to tag in the hemisphere containing both B's but not in the other, introducing a negative correlation.

- Shared primary vertex.

  The primary vertex is the only means by which the two hemispheres can directly affect one another, if tracks from both hemispheres are used in its reconstruction. A long-lived B hadron in one hemisphere will tag, but will also bias the position of the reconstructed primary vertex and increase its error. This reduces the significance of displaced vertices in the other hemisphere, which is therefore less likely to be tagged. Thus there is a source of negative correlation.

  As discussed in Section 5.3, the algorithm used in the analysis presented here reconstructs two primary vertices in each event, in order to reduce the correlation from this source. Nevertheless, a residual correlation remains, due to the beam-spot constraint used in the fit to the primary vertex. Uncertainty in the size of this correlation was one of the most intractable systematic errors in the measurement of R_b.

The absolute uncertainty in the value of ρ_b propagates directly through to a relative error in the measurement of R_b. This results in a significant contribution to the systematic error in the value of R_b.

4.4 Summary

Using the double tag technique, a very high-precision measurement of R_b is possible. The statistical error depends mainly on the number of events in which both hemispheres satisfy the b-tag. The systematic errors principally derive from the use of Monte Carlo simulation to predict the hemisphere-hemisphere correlation in tagging efficiency and the efficiency to mistakenly tag hemispheres from c and uds events. Using the ALEPH LEP I data sample collected from 1992–95, R_b is a systematics-limited measurement.

Chapter 5

Tagging $b\bar{b}$ events

In order to make a measurement of $R_b = \Gamma_{Z^0 \to b\bar{b}} / \Gamma_{Z^0 \to hadrons}$, it is necessary to identify hadronic events and $Z^0 \to b\bar{b}$ events. This chapter describes that process, outlining in Section 5.1 the algorithm by which hadronic events are selected. Section 5.2 briefly discusses different methods of tagging b events, along with the most important considerations when choosing a tag for a high-precision measurement of R_b.

Next, the b-tagging algorithm used for the analysis presented here is described. Reconstruction of the primary vertex, discussed in Section 5.3, is an important preliminary to the algorithm. Section 5.4 describes the tag itself.

5.1 Hadronic event selection

The first stage in a measurement of R_b is the selection of hadronic events, which in ALEPH uses information from charged tracks. There must be at least five charged tracks reconstructed in the TPC that satisfy the following requirements:

- The fit to the track helix must use at least four 3-dimensional points in the TPC. This eliminates most fake and badly fitted tracks.

- The track must pass through a cylinder centred around the fitted average interaction point, with a radius of 2 cm and a length of 20 cm. This rejects badly fitted tracks or particles originating far from the interaction point, as well as cosmic background.

- The angle between the track and the beam axis must be greater than $18.2°$. This ensures that at least six of the TPC pad rows are traversed by the track.

In addition, the total energy of all charged tracks which satisfy these selection criteria is required to be greater than 10 % of the centre of mass energy of the collision, to remove two-photon events and beam-gas interactions.

This selection procedure was designed for measuring the cross-section $\Gamma_{Z^0 \to hadrons}$. The efficiency of the selection is 97.5 %, with the main background contamination coming from two-photon and $Z^0 \to \tau^+\tau^-$ events and forming less than 0.7 % of the event sample [31, 32].

In order to ensure that most of the tracks in the event fall inside the acceptance of the vertex detector, the angle between the thrust axis and the beam axis is required to satisfy $|\cos\theta| < 0.7$. The thrust axis is determined for each event on the basis of an energy flow algorithm [24] which combines charged track information with the energy deposited in the calorimeter. After the full selection procedure, including the angular cut and the cuts implicit in the tag (which, for example, ignores events where no tracks pass its selection criteria), about 2.3 million hadronic events were retained from the data taking period 1992–95. The non-hadronic background was estimated to be 0.3 % of the sample and to consist mostly of $Z^0 \to \tau^+\tau^-$ events.

As a whole, the selection procedure could potentially introduce a flavour bias, which was estimated from Monte Carlo simulation. The acceptance efficiencies were 61.97 ± 0.02 %, 61.99 ± 0.04 % and 61.88 ± 0.03 % for b, c and uds events respectively.

5.2 Introduction to b-tagging

Many different tags have been used to measure R_b, falling into 3 general categories:

- Leptons with high momentum transverse to the jet.

  Historically, this was the first b-tag to be used at LEP. It identifies leptons from semileptonic decays of b quarks, as described in [27]. However, the branching ratios of the b quark to muons and electrons are only about 10 % each, so that the statistical error on R_b is large when this tag is used.

- Event shape tags.

  Event shape tags, such as that described in [33], rely on the distinctive distributions of event shape variables in b events. These result from the large masses of B hadrons and the hard fragmentation of the b quark. Often the variables are combined by means of neural nets, which give a single output variable that behaves differently for b events than for other flavours. Such tags have small statistical errors, but reliance on Monte Carlo to estimate the backgrounds leads to systematic errors that can be hard to quantify.

- Lifetime tags.

  These methods depend on the long lifetime and hard fragmentation of b quarks. Lifetime tags fall into two categories — those which reconstruct a secondary vertex, such as that used by OPAL [34] and those which rely on impact parameter, such as that described in Section 5.4.1. At LEP and SLC, typical B hadron decay lengths are of order 3 mm and the impact parameters of their decay products are around 450 μm.

  Lifetime tags have high statistics, as in principle any b event may be tagged. Since the installation of silicon vertex detectors at the LEP experiments and SLD has allowed very accurate determinations of secondary vertex positions and impact parameters (Section 2.2.6), the most precise measurements of R_b have made use of this technique.

As discussed in Chapter 4, precision measurements of R_b are now dominated by systematic errors. Thus, it is essential to design a tag which will minimise the sources of systematic uncertainty and will allow those remaining to be reliably estimated. The factors that contribute most to the systematic error are the efficiency for tagging hemispheres of c events and the correlation between tagging probabilities in the two hemispheres of b events.

5.3 Reconstruction of the primary vertex

Before beginning the b-tagging process, it is necessary to reconstruct the interaction point, or primary vertex. The region of beam overlap at LEP produces a beam-spot which extends about 250 μm in x, 15 μm in y and 1.5 cm along the beam axis. For each event, information from charged tracks is combined with this beam-spot constraint to reconstruct a primary vertex.

In an event containing heavy quarks, many tracks do not originate from the primary vertex, but from a secondary or tertiary vertex where the heavy hadron decayed. Nonetheless, they can still be used in the reconstruction process by projecting tracks into a plane perpendicular to the flight path of the parent hadron, as shown in Fig-

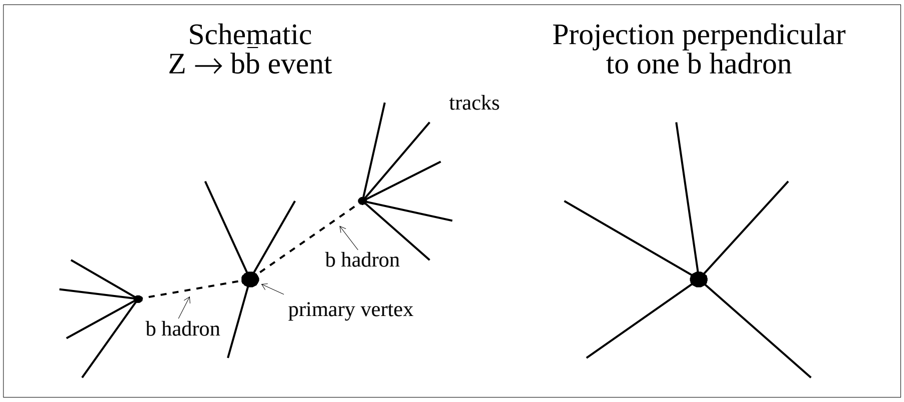

Figure 5.1: *Removal of the lifetime component of tracks by projection along the B hadron flight direction.*

ure 5.1 . In practice, this path is approximated by the direction of the jet containing the heavy hadron.

To identify jets, charged tracks and neutral objects reconstructed with the energy flow algorithm were clustered using the JADE algorithm [35] with $y_{cut} = 0.01$. As implemented in this analysis, the algorithm works as follows: The pair of tracks in the event with the smallest invariant mass, M, is found. If $(M/E_{beam})^2 < y_{cut}$, where E_{beam} is the LEP beam energy, the two tracks are merged by adding their 4-momenta, and are considered as one. The process is then repeated, using the remaining tracks and the new combined track, finding a new pair which are also merged. This continues until no pair of track combinations has a low enough invariant mass to be merged. The track combinations remaining at this stage are the jets. Only jets with momentum greater than 10 GeV are used in finding the primary vertex and events must have at least two such jets to be accepted.

Charged tracks are associated with their closest jet and projected onto the plane perpendicular to the jet axis, as described above. In addition, the event is divided into two hemispheres by a plane perpendicular to the thrust axis and tracks are associated with one of these hemispheres. The standard ALEPH primary vertex-finding algorithm uses tracks from both hemispheres. However, since the b-tag used in this analysis depends critically on the primary vertex position and the error on this quantity, a single primary vertex shared by the two hemispheres introduces a negative correlation of order 10 % between the tagging probabilities. As described

	standard PV finder		modified PV finder	
	rms/μm	bias/μm	rms/μm	bias/μm
uds events	47	0	62	2
c events	51	0	71	-2
b events	62	0	89	-4

Table 5.1: *Resolution (rms) and bias in microns of the primary vertex reconstruction, projected along the thrust axis direction for the standard ALEPH method and the modified method that finds the primary vertex separately in each hemisphere.*

in Chapters 4 and 7, the systematic uncertainties associated with the prediction of this correlation would be a major source of error in R_b. Uncertainties due to the hardness of the b fragmentation and the average B decay multiplicity each contribute a relative error of order 0.5 % to R_b when a single primary vertex is used. To limit this source of correlation and its associated errors, two primary vertices are reconstructed for every event, each using only the tracks in one hemisphere. When this method is used, the systematic uncertainties in the correlation due to b fragmentation and B decay multiplicity are greatly reduced.

For each hemisphere, a primary vertex is fitted using projected tracks and the beam-spot information. It is refined in further iterations by including the longitudinal component of any track with a point of closest approach to its jet that lies within 250 μm of the reconstructed primary vertex position.

The resolution of this algorithm is shown in Table 5.1 for uds, c and b events, projected along the thrust axis. In the standard primary vertex-finding algorithm, using tracks from both hemispheres, the separation along the thrust axis of the reconstructed and true primary vertices has a distribution with an rms of $62\,\mu m$ in b events. When separate primary vertices are constructed for each hemisphere, this resolution becomes $89\,\mu m$. The degraded resolution is due to loss of information — on average, the standard algorithm uses 15.7 track components transverse to the jet direction and 4.7 longitudinal components, whereas the separated hemispheres method uses 7.8 transverse and 4.4 longitudinal components.

The negative bias for c and b events indicates that the reconstructed primary vertex is pulled slightly along the thrust axis into the hemisphere being considered. However, the size of this bias is negligible, being approximately 4 μm in b events, compared to the overall resolution of $89\,\mu m$.

5.4 The *b*-tag algorithm

The *b*-tag used in the analysis described here is designed to reduce the charm background as far as possible. In order to do so, it combines information from two sources — a lifetime tag, based on impact parameter, and a tag that uses both event-shape and lifetime information, based on the high invariant mass of B hadrons as well as the large impact parameters of their decay products.

5.4.1 The impact parameter tag

The first component of the *b*-tag depends on the large impact parameters of tracks produced in B hadron decays. Although tags which reconstruct a secondary vertex might be considered to use more information from an event, in the case of ALEPH this seems to be outweighed by the advantages of an impact parameter tag. In particular, B hadrons typically decay to hadrons containing c quarks, which also have lifetime. A reconstructed secondary vertex can miss tracks from the tertiary vertex, whilst they are included in the impact parameter method and contribute to its statistical power.

The impact parameter tag described here is the ALEPH package QIPBTAG [36]. It begins by taking the jets created by the primary vertex finding algorithm described in Section 5.3. Each track is assigned to a jet and its closest point of approach to the

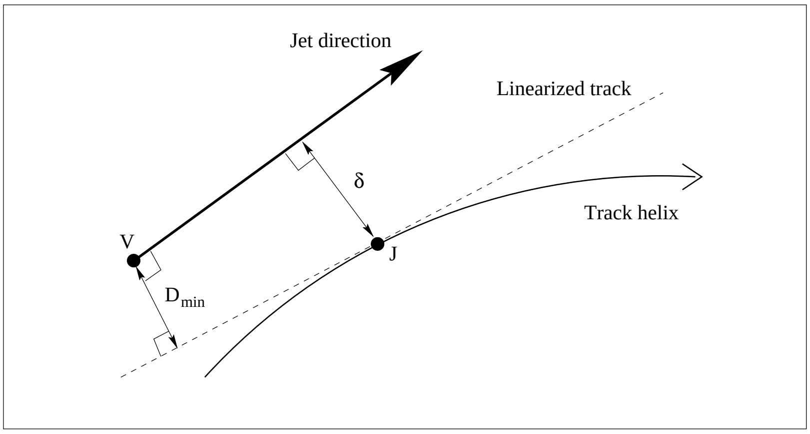

Figure 5.2: *Definition of impact parameter. V is the primary vertex, J is the point of closest approach of the track helix to the jet direction, at a distance* δ*, and* D_{min} *is the 3-dimensional impact parameter, which is positive for the track shown here. The jet direction and the track are not in the same plane.*

jet axis, J, is found (Figure 5.2). The track is linearized at this point and the impact parameter, D_{min}, is defined as the smallest distance in three dimensions between the linearized track and the primary vertex. If J falls in front of the primary vertex, so that the track is likely to have come from the decay of a long-lived hadron, D_{min} is defined to be positive. If it falls behind the primary vertex, as a result of imperfect detector resolution, D_{min} is defined to be negative. The error on the measured value of the impact parameter, $\sigma(D_{min})$, is calculated from the error matrix of the track fit, the primary vertex error and the correlation between the two. This correlation arises from the fact that the primary vertex position is calculated using the charged tracks in the hemisphere. The raw variable on which the tag is based is the impact parameter significance, $S_D = D_{min}/\sigma(D_{min})$.

Since tracks with negative S_D result from the imperfect resolution of the detector, they can be used to define a resolution function, $R(|S_D|)$, by a fit to their probability distribution. This probability distribution is shown in Figure 5.3 for tracks from the Monte Carlo with both positive and negative impact parameters, for different event flavours. It can be seen that for tracks from *uds* events, the distribution is largely symmetric about $S_D = 0$, whilst for b and c events there is a tail towards large positive

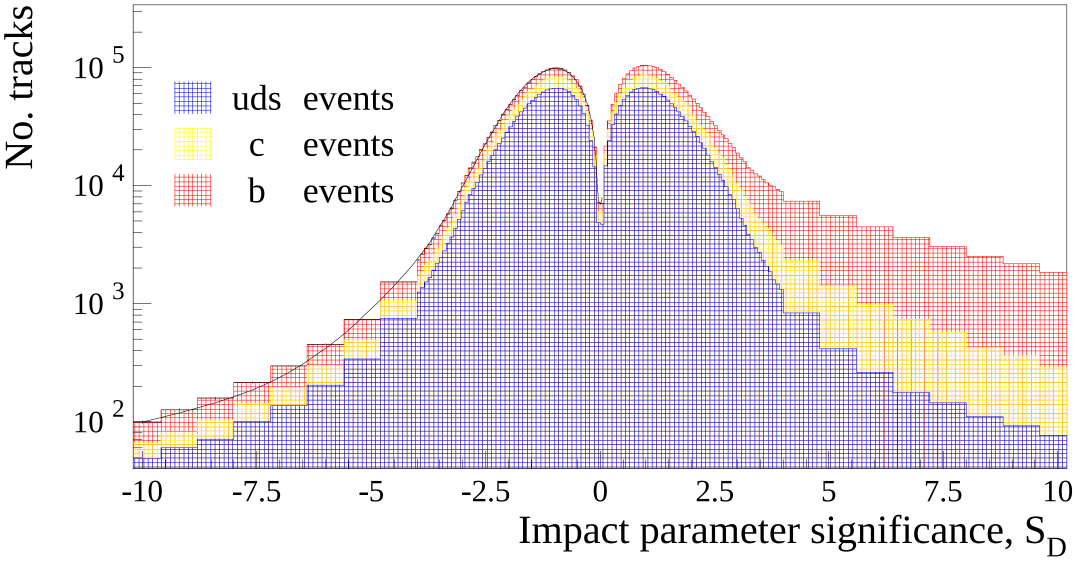

Figure 5.3: *Histogram of impact parameter significance, S_D, for different event flavours from Monte Carlo. The resolution function, $R(|S_D|)$, is obtained by a fit to the $S_D < 0$ region of this distribution for tracks from real data. The black curve gives the equivalent fit for the distribution shown here.*

values, resulting from the decay products of long-lived B and D hadrons. When fitting the resolution function, it is desirable to reduce the contribution of tracks with true lifetime but incorrectly signed S_D. For this reason, the tag is used to select mainly uds events by demanding $P_H > 0.5$ in the opposite hemisphere, where P_H, the impact parameter tag variable, is defined below in Equation 5.2. It should be noted that in practice the resolution function is derived using tracks from real, not simulated, data.

If all the errors were strictly Gaussian, $R(|S_D|)$ would take the form $|S_D|e^{-|S_D|^2/2\sigma^2}$. However, in practice there are substantial non-Gaussian tails in the errors, due the non-Gaussian behaviour of the tracking. A good fit is obtained by adding two independent, exponentially decreasing tails of the form $|S_D|e^{-|S_D|/\lambda}$ to the Gaussian component.

Separate resolution functions are used for tracks according to the number of VDET hits associated with them, since the impact parameter resolution depends critically on this. They are divided into several classes, of which the most important are tracks recording a spacepoint hit ($r\phi$ and z coordinates) in both VDET layers and tracks recording a spacepoint hit in one VDET layer only. There are also smaller classes containing tracks with only 2-dimensional information (one or two VDET hits in $r\phi$ or z only), tracks with no VDET hits but many hits recorded in the ITC and reconstructed V^0 tracks. Tracks which do not fall into any of these classes are not used in the tag. Of the tracks which are used by the tag, about 70 % have two spacepoint hits in the VDET and about 25 % have just one.

Using the resolution function, $R(|S_D|)$, the probability, P_T, that a track originating from the primary vertex would have the observed positive impact parameter significance, S_D, can be obtained. This is done by integrating the resolution function:

$$P_T(S_D) = \int_{S_D}^{\infty} R(x)\,dx\,. \tag{5.1}$$

For tracks which have negative S_D, P_T is defined to be $-P_T(-S_D)$. Because of the definition of $R(|S_D|)$, P_T acts like a confidence level. Thus, as shown in Figure 5.4, there is a flat distribution between -1 and +1, due to tracks coming from the primary vertex, along with a spike at small positive values, due to tracks originating from decays of long-lived particles.

The probabilities P_T for the tracks with positive impact parameter in a hemisphere are combined to give the probability, P_H, that a hemisphere containing no particles with lifetime would produce the observed set of P_T values or any less likely set. Given

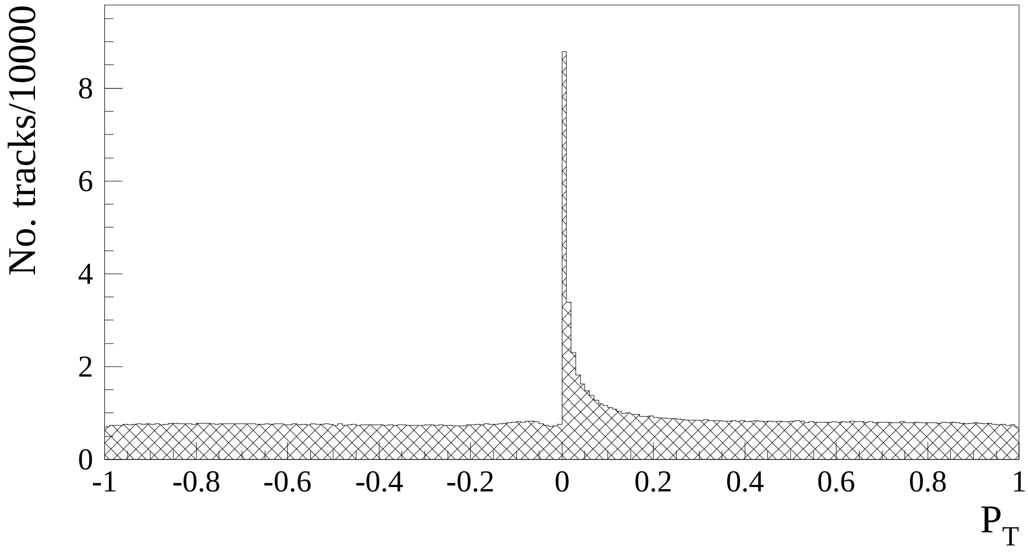

Figure 5.4: *Histogram of P_T, the probability that a track originates from the primary vertex.*

N such tracks, P_H is defined as:

$$P_H = \Pi \sum_{j=0}^{N-1} \frac{(-\ln \Pi)^j}{j!}\,, \tag{5.2}$$

where

$$\Pi \equiv \prod_{i=1}^{N} P_T(track\ i)\,. \tag{5.3}$$

Mathematically, this is the probability that N tracks from the primary vertex will combine to produce the observed value of Π or any less likely value.

As mentioned in Section 5.3, two separate primary vertices are reconstructed in each event, each using information from charged tracks in one hemisphere. In calculating P_H for a given hemisphere, the primary vertex constructed using tracks in that hemisphere is used.

Not all tracks from a hadronic event are useful for the calculation of P_H. In particular, it is important not to include badly-measured tracks or tracks from long-lived particles other than B hadrons, such as $\mathrm{K^0_S}$ or photon conversions. Thus, in addition to track cuts designed to eliminate badly-measured tracks, there are also cuts to remove tracks consistent with being daughters of a $\mathrm{V^0}$ and tracks not passing close enough to the estimated B flight direction (within 750 μm).

It is possible to tag hemispheres containing a b quark by requiring that P_H should be less than a certain cut value, as shown in Figure 5.6 . The purity and efficiency of this tag for b events is shown in Figure 5.7 .

5.4.2 The mass tag

The impact parameter tag described in Section 5.4.1 selects event hemispheres by requiring that they should be unlikely to contain zero lifetime. This proves to be very effective for rejecting uds events, which indeed contain no lifetime, but less good for rejecting c events. Thus, an additional tag depending on the fact that the b quark has a larger mass than the c quark was developed.

Figure 5.5 shows the invariant mass, M_H, of all the tracks in a hemisphere which share a jet and have a P_T value of less than 10 %. For b events, a distribution taking values up to the B hadron mass would be expected, whereas for c events M_H should not exceed the D hadron mass. Indeed, it can be seen that there are almost no c events with a value of M_H greater than 1.8 GeV, approximately the typical mass of a charm hadron.

This reasoning gives the rationale behind the mass tag. Tracks are selected as for the impact parameter tag described above and for each, the probability that it is consistent with the primary vertex is calculated. Tracks within each jet are combined one by one, in decreasing order of incompatibility with the primary vertex. When the invariant mass of one jet is brought above 1.8 GeV, the value of P_T for the last track added, $P_T(last)$, forms the mass tag variable. For b events, this probability can be very small, since the charm hadron mass can be exceeded using only tracks from the B hadron decay. For c events, it will be larger, since this mass can only be exceeded by including tracks from the primary vertex. A cut on $P_T(last)$ can be used to separate b events from c and uds events, as shown in Figures 5.6 and 5.7 .

5.4.3 The combined tag

Since the impact parameter tag and the mass tag have different sources of background, a combined tag where the cut is on a linear combination of the two variables could potentially perform better than either tag alone. The optimal combination for the two tags described above, maximising the efficiency to tag b events and the purity of

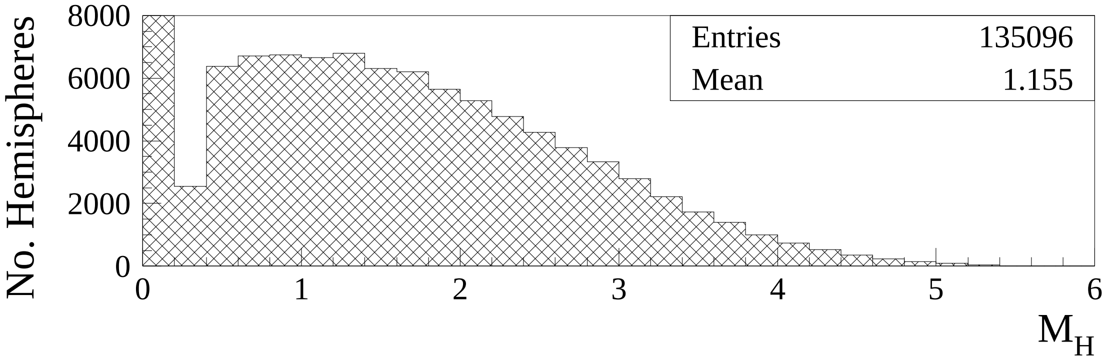

b hemispheres

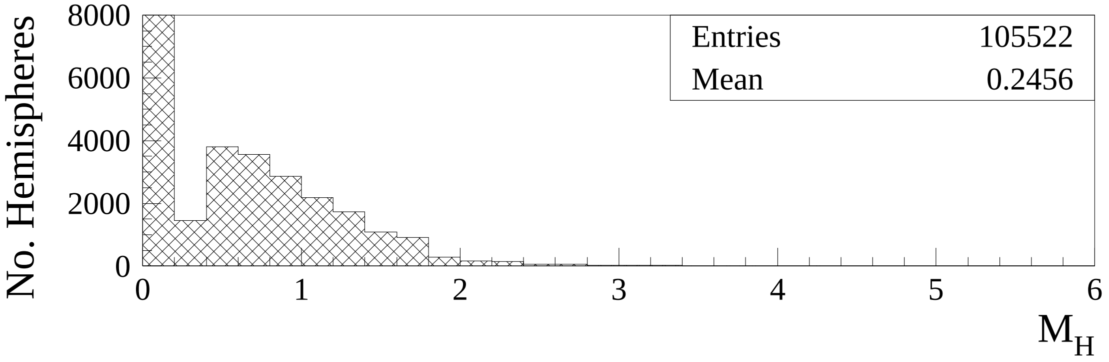

c hemispheres

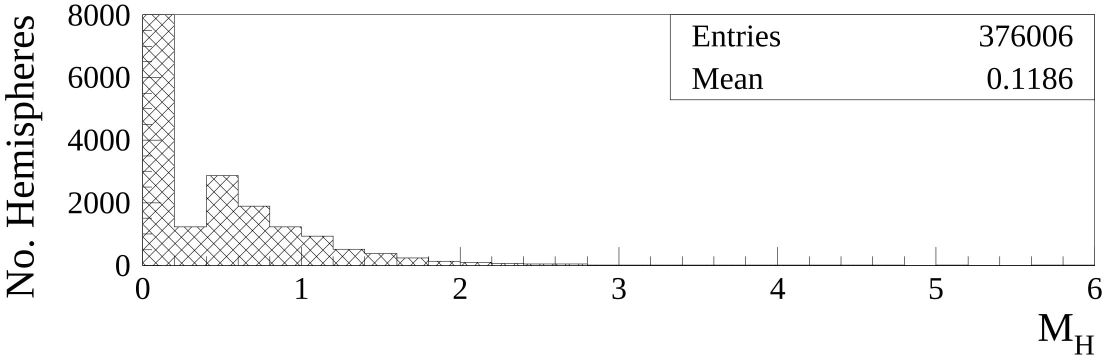

uds hemispheres

Figure 5.5: *Invariant mass of charged tracks in a hemisphere that are inconsistent with the primary vertex. The height of the bin at* $M_H = 0$ *has been truncated.*

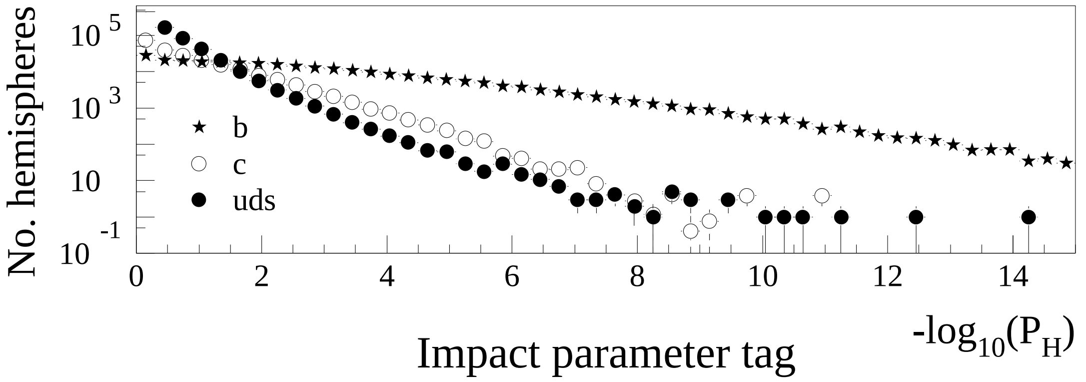

Impact parameter tag

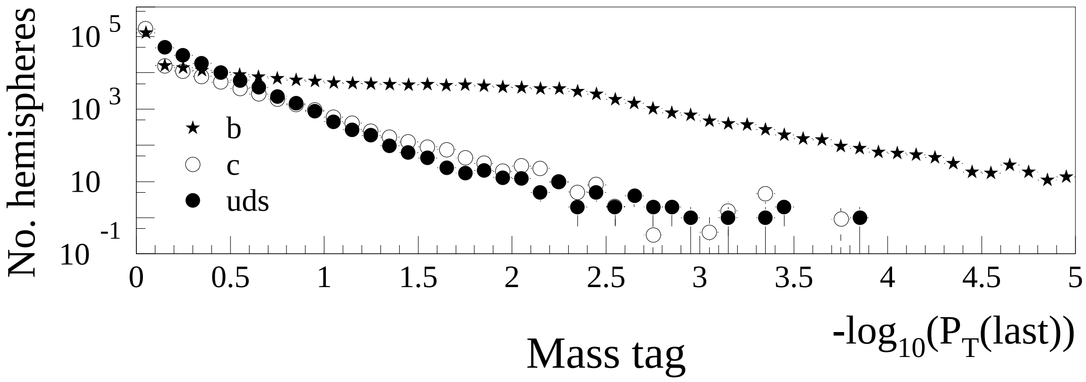

Mass tag

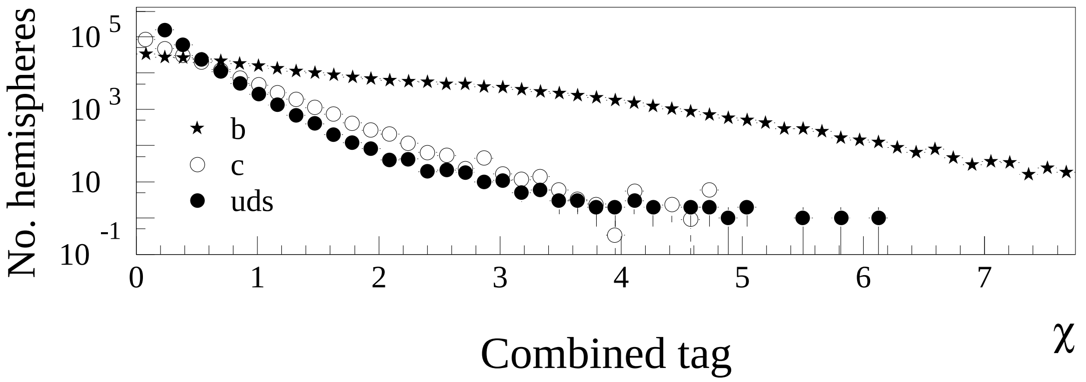

Combined tag

Figure 5.6: *Distribution of the tagging variable in b, c and uds events for the impact parameter, mass and combined tags.*

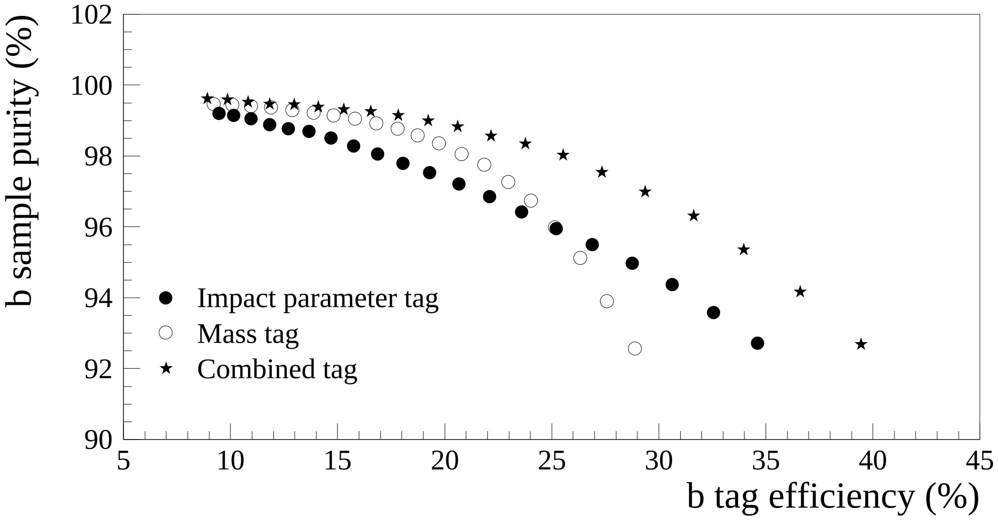

Figure 5.7: *Purity and efficiency of the impact parameter, mass and combined tags.*

the sample, is found with Monte Carlo simulation to be

$$\chi = -0.7\log_{10}(P_T(last)) - 0.3\log_{10}(P_H)\,. \tag{5.4}$$

The distribution of this variable according to event flavour can be seen in Figure 5.6.

Figure 5.7 compares the efficiency for tagging b hemispheres and the purity of the sample for the impact parameter and mass tags separately and for the combined tag. It can be seen that the performance of the combined tag is superior to either of its constituent parts alone. The impact parameter tag performs better at tagging hemispheres in which the secondary vertex is not well separated from the primary vertex, whilst the mass tag is better at rejecting charm hemispheres where the c quark has very long lifetime. With a cut on χ set to give an efficiency of 23 % for tagging b hemispheres, a purity of around 98 % is achieved.

5.5 Summary

Before calculating R_b, hadronic events were selected and the polar angle of the thrust axis was required to satisfy $|\cos\theta| < 0.7$. After this selection, the mainly $\tau^+\tau$ background formed about 0.3 % of the sample. Next, the primary vertex was reconstructed on an event-by-event basis and the b events were identified. Two primary vertices were constructed for every event, each using only tracks from one hemisphere. This technique reduces the hemisphere-hemisphere correlation, a major source of systematic uncertainty in R_b, but also degrades the position resolution of the algorithm.

The method used to select b events is formed from two parts — an impact parameter tag, similar to that used in the earlier ALEPH measurement of R_b with a lifetime tag, and a new tag based on the invariant mass of tracks inconsistent with the primary vertex. These two tags were combined to produce a sample of b hemispheres, with around 98 % purity for a 23 % tagging efficiency.

Chapter 6

Results

Using the method outlined in Chapter 4, the value of R_b was calculated at various cuts on the b-tag variable χ described in Chapter 5. At harder cuts, fewer hemispheres are selected, reducing the tagging efficiency. However, the proportion of hemispheres from b events is greater, so that the purity of the sample is increased. For each measurement, the systematic error was obtained using the methods described in Chapter 7.

The bottom plot in Figure 6.1 shows the variation of the error on the value of R_b as a function of the cut on χ. It can be seen that at small values of the cut, the measurement is dominated by tracking systematics, whilst at large values of the cut, it suffers from large statistical errors. A cut at $\chi = 1.9$ was found to be optimal. Table 6.1 summarises the efficiencies and correlation at this cut.

Parameter	(Value ± stat. error)/%
ϵ_c	0.425 ± 0.051
ϵ_{uds}	0.051 ± 0.010
ρ_b	3.74 ± 0.25
ϵ_b(MC)	22.86 ± 0.02
ϵ_b(data)	$22.7 \pm 0.12(stat.) \pm 0.14(syst.)$

Table 6.1: *Monte Carlo predictions for background efficiencies and correlation when a cut at $\chi = 1.9$ is used. The prediction for ϵ_b, not used in the calculation of R_b, is also shown, along with the value of ϵ_b extracted from the data.*

After the event selection cuts, 2.3 million events from the 1992–95 data-taking period remained. For a cut on the hemisphere tagging variable of $\chi > 1.9$, efficiencies of $\epsilon_c = (0.425 \pm 0.051(stat.))\,\%$ and $\epsilon_{uds} = (0.054 \pm 0.010(stat.))\,\%$, for tagging c and light quark hemispheres respectively, were predicted from the Monte Carlo. The correlation in tagging efficiency between the two hemispheres of an event was predicted to be $\rho_b = (3.74 \pm 0.25(stat.))\,\%$. Using Equations 4.1 and 4.2, the efficiency to tag b event hemispheres was calculated to be $(22.66 \pm 0.12(stat.) \pm 0.14(syst.))\,\%$, compared to a Monte Carlo prediction of $\epsilon_b = (22.86 \pm 0.02(stat.))\,\%$. Although ϵ_b is not used as an input for the derivation of R_b, it enters at second order into the prediction of the correlation, so that good agreement between data and Monte Carlo values of ϵ_b is a useful check.

With a cut at 1.9, the value of R_b was found to be:

$$\begin{array}{lll}
\boldsymbol{R_b = (21.72} & \boldsymbol{\pm 0.11} & \textbf{Data statistics} \\
 & \boldsymbol{\pm 0.05} & \textbf{Monte Carlo statistics} \\
 & \boldsymbol{\pm 0.10} & \textbf{Detector simulation uncertainties} \\
 & \boldsymbol{\pm 0.07} & \textbf{Non-B physics uncertainties} \\
 & \boldsymbol{\pm 0.04} & \textbf{B physics uncertainties} \\
 & \boldsymbol{\pm 0.10} & \textbf{Specific correlation uncertainties} \\
 & \boldsymbol{\pm 0.01} & \textbf{Event selection uncertainties} \\
 & \boldsymbol{-0.037 \times} & \boldsymbol{[R_c - 17.1])\,\%}
\end{array}$$

The last line above shows the dependence of the result on R_c (measured in percent). Fig 6.1 shows the variation of R_b as a function of the cut. Its value can be seen to be stable to within the variation allowed by the uncorrelated error.

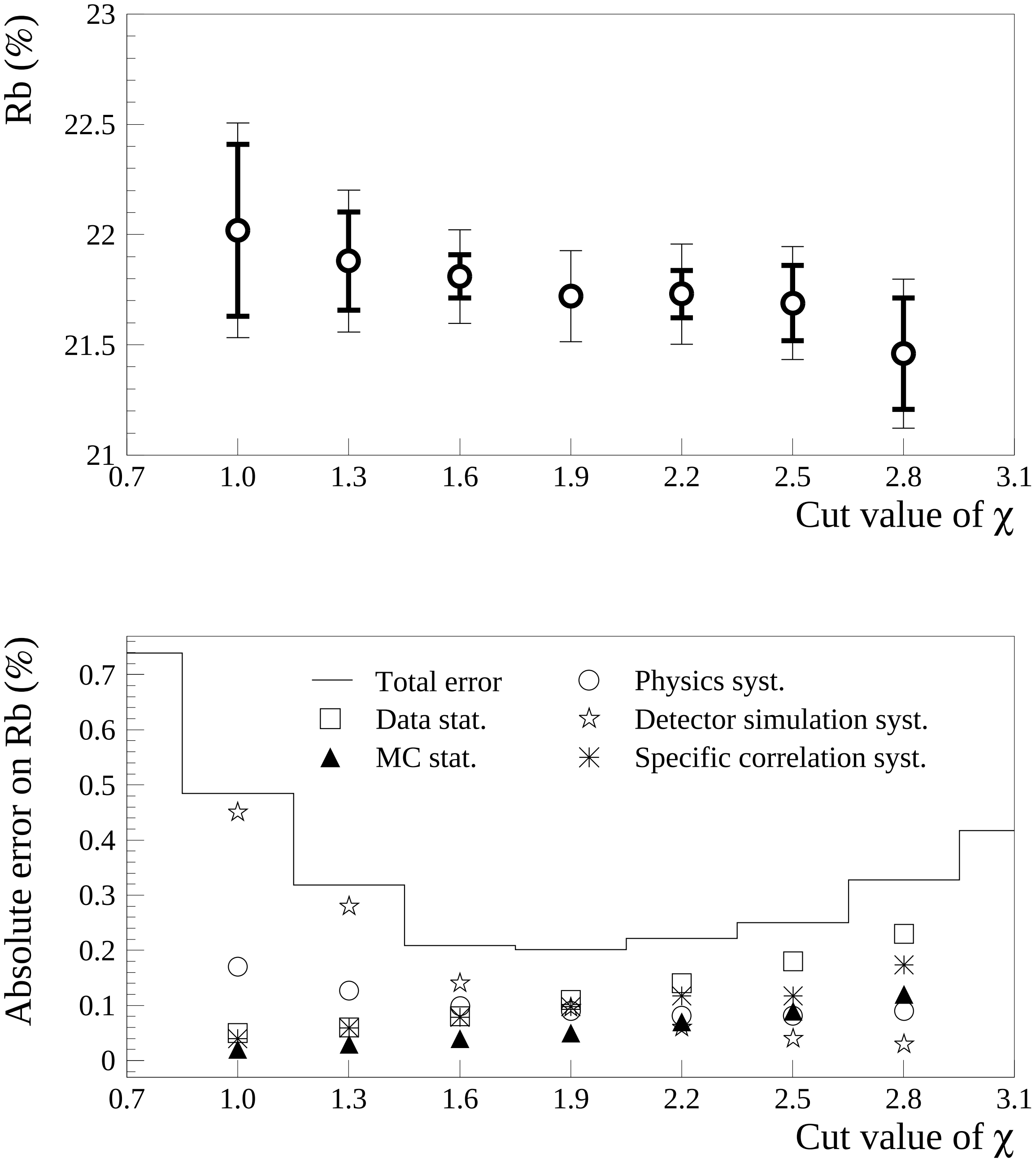

Figure 6.1: *Variation of R_b with b-tag cut (top plot). The thin lines show the total statistical plus systematic error, whilst the thick lines show the error relative to the measurement at a cut of* 1.9 *. The bottom plot shows the total error on R_b as a function of cut.*

Chapter 7

Systematic uncertainties

The principal sources of systematic error in the value of R_b arise from the use of Monte Carlo simulation to predict the charm and light quark efficiencies, ϵ_c and ϵ_{uds}, and the hemisphere-hemisphere correlation, ρ_b. Other sources of error are uncertainties in the amount of flavour bias in the selection of hadronic events and in the size of the non-hadronic background, which have much smaller effects. Another potential source of uncertainty is R_c, which in the analysis described here is taken from theoretical predictions. This chapter discusses the systematic uncertainties affecting the measurement of R_b and describes the methods used to estimate their size.

A good understanding of the detector simulation in the Monte Carlo is essential for prediction of the background efficiencies and the hemisphere-hemisphere correlation. Corrections were applied to the Monte Carlo events so that they more accurately reflected the detector resolution and efficiency found in the data. A systematic error due to uncertainties in these corrections was then derived, as described in Section 7.1 .

Our imperfect knowledge of the physics parameters which must be used as inputs for the Monte Carlo simulation affects the prediction of ϵ_c, ϵ_{uds} and ϵ_b. The estimated errors in the values of the first two quantities propagate directly into uncertainties in the value of R_b, according to Equations 4.5 and 4.6 . The Monte Carlo prediction of ϵ_b affects the value used for ρ_b, whose uncertainties propagate to R_b as shown by Equation 4.7 . The average values of parameters such as the relative production rates of charm hadrons were matched between the Monte Carlo and the best measurements we have from data by applying weights to the simulated events. Parameters can be divided into those which relate only to B physics and thus only affect R_b to second order via ρ_b, and those which also affect other flavours. Section 7.2 deals with the latter, including factors such as charm production and decay, gluon splitting to heavy quarks and the production of V^0's. The effects of uncertainties in B physics are discussed in Section 7.3 .

As mentioned in Chapter 4, there are additional uncertainties in the value of ρ_b which are not accounted for by the variation of B physics in the Monte Carlo. In Section 7.4, the effects of individual sources of correlation are compared between data and Monte Carlo. Any discrepancies are considered to be uncertainties in the value of ρ_b and propagated to give a systematic error in the value of R_b.

7.1 Detector simulation

The b-tag used in the analysis presented here is highly sensitive to the impact parameters of tracks and their associated errors. A good understanding of the tracking is therefore needed when using Monte Carlo to predict ϵ_c, ϵ_{uds} and ρ_b. Two discrepancies between data and Monte Carlo were found to be important here. In the Monte Carlo, about 5–10 % more tracks pass the tag's selection criteria than in the data. In addition, the resolution of track impact parameters is found to be better in Monte Carlo than in data.

To rectify these problems, corrections were applied to the Monte Carlo events. Tracks were randomly removed from each event, so that the average number of tracks used in the tag was the same as for the data. In conjunction with this, track impact parameters were smeared so that the spectrum in the Monte Carlo agreed with that obtained from the data. A systematic error remained due to uncertainties in these corrections. For example, the method just described assumes that the corrections are independent between tracks in an event. Uncertainties related to the detector simulation propagate to systematic errors in the value of R_b through their effect on ϵ_c, ϵ_{uds} and ρ_b. Together they contribute one of the largest sources of uncertainty in the measurement of R_b.

7.1.1 Track reconstruction efficiency

More tracks are used to construct the b-tag in Monte Carlo than in data, due to overestimation of VDET efficiency in the Monte Carlo. The efficiency for a track to record a VDET hit is simulated for Monte Carlo using a map that is derived from real events in the data, as outlined in Chapter 3. However, as explained in that chapter, the efficiency for associating a VDET hit to the track which caused it is not perfectly

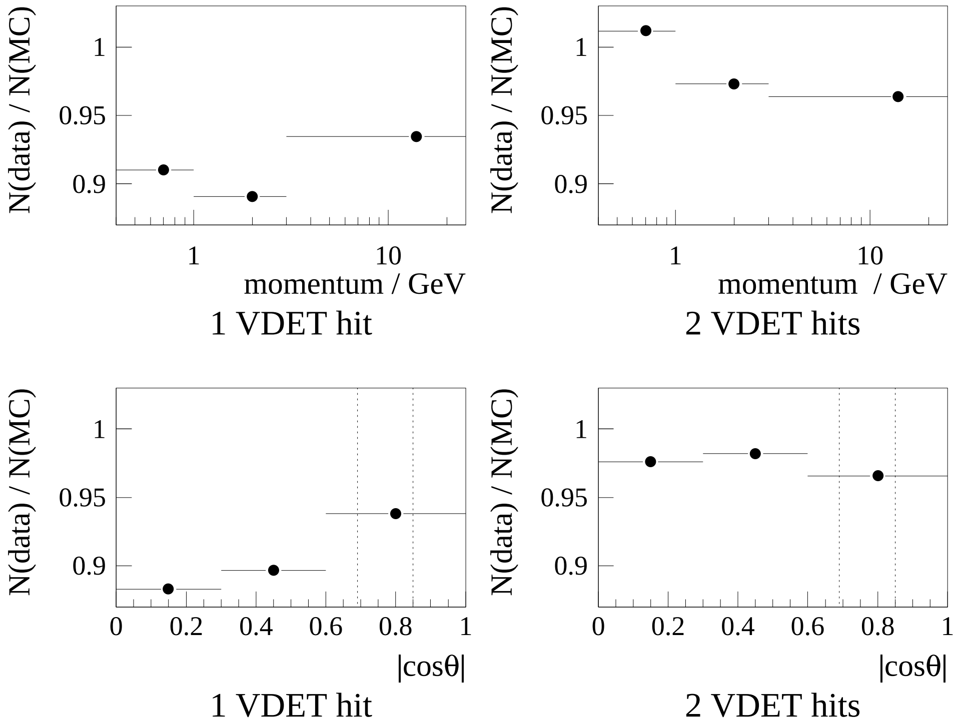

Figure 7.1: *Ratio (data/Monte Carlo) of the number of tracks used by the b-tag in 1993, normalized to the number of events. The left-hand plots show the ratio for tracks with one spacepoint hit in the VDET, as a function of momentum (top) and polar angle θ (bottom, where the dotted lines indicate the edges of each VDET layer). The right-hand plots show the same for tracks with two spacepoint hits in the VDET.*

reproduced. In addition, discrepancies can arise from the track selection procedure performed by the tag. To allow for this, some tracks were randomly removed from Monte Carlo events so that there was no longer an excess.

The probability for a track to be removed from a Monte Carlo event was determined by the ratio of the number of tracks in real and simulated data, as a function of the number of hits recorded in the VDET, polar angle and momentum. Since the VDET and its efficiency change from year to year, as modules become damaged and are repaired, the comparison was made separately for each year of data taking. Because the Monte Carlo overestimated the probability for a track to be associated with a VDET hit, it was only rarely the case that the Monte Carlo had fewer tracks than the data, and even then the excess was small. For these cases, no correction was made. The fraction of tracks removed was around 10 % for tracks with one spacepoint hit in the VDET and around 5 % for those with two. (About 25 % of the tracks used by the tag record a spacepoint hit in one layer of the VDET and about 70 % record spacepoint hits in both layers).

Figure 7.1 shows the ratio between the number of tracks used by the b-tag in data and Monte Carlo for one year of data taking and two classes of tracks — those with one or two spacepoint hits in the VDET. The dependence of the correction factor on the polar angle, θ, and momentum can be seen. Tracks with one VDET hit that fall inside the acceptance of the outer layer ($|\cos\theta\,| < 0.69$) require a different percentage correction from those outside. The latter would be expected to have just one hit, whereas the former have failed to record a hit in one layer due to inefficiency in associating tracks with VDET hits. Correctly reproducing this is important for the part of the hemisphere-hemisphere correlation which relates to the polar angle of the thrust axis (described in Section 4.3).

7.1.2 Impact parameter resolution

Another discrepancy between data and Monte Carlo affecting the b-tag arises from the impact parameter resolution. The tag algorithm uses tracks with positive impact parameters, ($S_D = D_{min}/\sigma(D_{min})) > 0$. The impact parameter significance distribution for such tracks cannot be directly compared between data and Monte Carlo, because the effects of imperfect detector simulation cannot be disentangled from the effects of imperfectly known parameters used as physics input for b and c events. However, the resolution function is expected to be symmetrical about zero, so that the negative impact parameter spectrum can be used to study the detector resolution. To reduce the contribution to the plots in Figures 7.2 and 7.3 of tracks with true lifetime but incorrectly signed S_D, the impact parameter tag was used to select a sample enriched in uds events. Tracks were only included in the plots if they lay opposite a hemisphere for which $P_H > 0.5$, where P_H, the impact parameter tag variable, is defined in Equation 5.2.

As described in Chapter 5, the b-tag is calibrated using the negative impact parameter significance spectrum, (S_D for tracks with $S_D < 0$), derived from tracks in the data. It can be seen from Figure 7.2 that the spectrum shows better resolution in Monte Carlo than in data, with the data having an excess of tracks at larger impact parameter significance. This discrepancy changes significantly as a function of momentum.

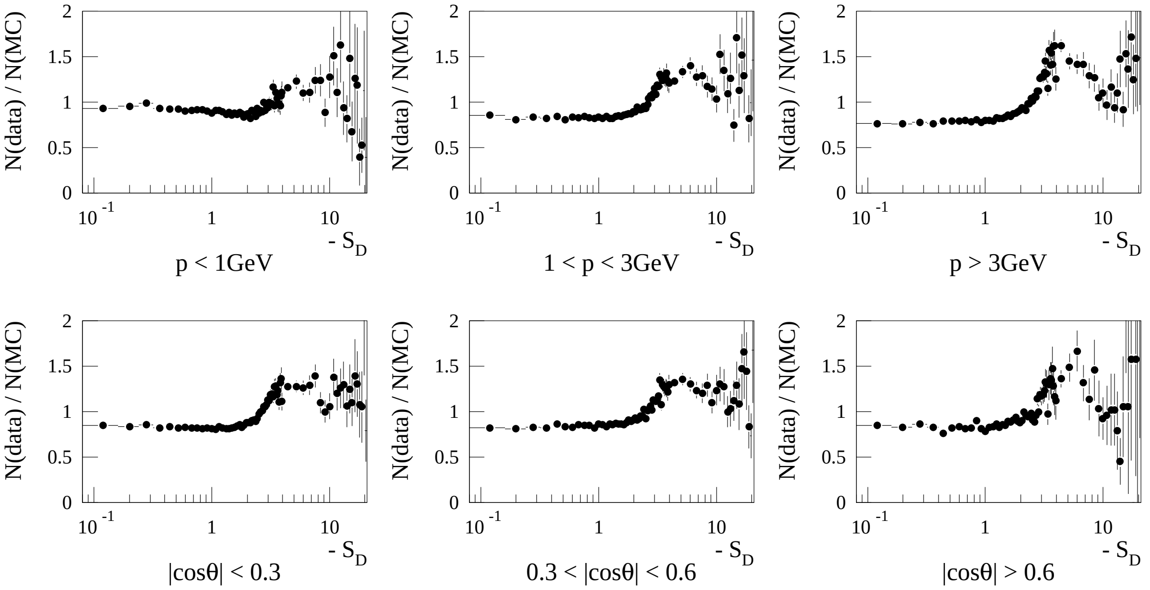

Figure 7.2: *Ratio (data/Monte Carlo) of negative impact parameter significance ($-S_D = -D_{min}/\sigma(D_{min})$) spectra, for tracks in 1993 with two space-point hits in the VDET. Tracks have been separated according to momentum p (top plots) and polar angle θ (bottom plots).*

The over-optimistic detector resolution in the Monte Carlo was compensated by smearing the impact parameters of some of the simulated tracks. This was done according to two exponential distributions. A fraction A_1 of tracks had their impact parameters shifted by a distance $k\sigma(D_{min})$, where $\sigma(D_{min})$ was the error on the impact parameter and k was a factor taken from an exponential probability distribution with decay constant λ_1. The process was repeated for a further fraction A_2 of tracks, using an exponential distribution with decay constant λ_2. In both cases, the shift was in a random direction. The remaining fraction $(1 - A_1 - A_2)$ of tracks were not affected.

Parameter	A_1	λ_1	A_2	λ_2
1 VDET hit	0.2298	0.731	0.0294	6.418
2 VDET hits	0.1894	0.629	0.0036	6.213

Table 7.1: *A typical set of smearing parameters. The effect of each parameter is described in the text.*

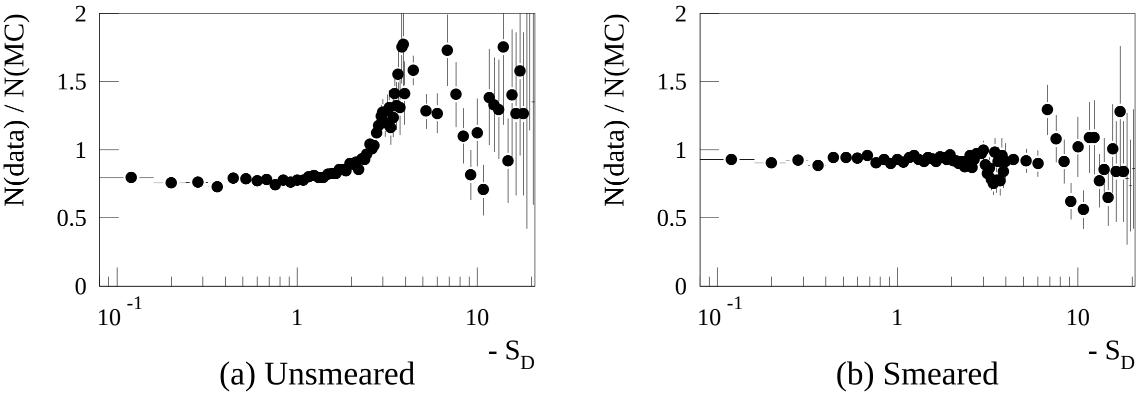

(a) Unsmeared (b) Smeared

Figure 7.3: *Ratio between data and Monte Carlo (MC) of negative impact parameter significance ($-S_D$) spectra, for tracks in 1993 with 2 spacepoint hits in the VDET and momentum greater than 3 GeV.*
a) Monte Carlo without impact parameter smearing.
b) Monte Carlo with impact parameter smearing.

This form of smearing was chosen to allow for both a mild effect caused by overestimation of VDET resolution by the Monte Carlo and a more severe effect due to pattern recognition errors in the track reconstruction, which would shift the impact parameters by a large amount. The parameters A_1, A_2, λ_1 and λ_2 used for smearing were determined by a fit between data and Monte Carlo, so that the χ^2 from comparing the negative impact parameter significance spectra in the data and the corrected Monte Carlo was minimal. Separate fits were done according to the number of hits recorded in the VDET, the momentum and the polar angle of the tracks and the year of data taking. The use of two exponential distributions resulted in good agreement between corrected Monte Carlo and data.

Table 7.1 shows a typical set of fit parameters for tracks with momentum greater than 3 GeV. The effect of applying smearing corrections with these parameters can be seen in Figure 7.3 . This shows the ratio of the negative impact parameter significance spectra in data and Monte Carlo before and after smearing, for the case of tracks with two spacepoint hits in the VDET.

7.1.3 Estimating the systematic error

There are two major uncertainties in the method described above. Firstly, there is no allowance for any dependence of the corrections on track properties other than number of VDET hits, momentum and polar angle, θ. To allow for this, smearing and track removal were performed first independently of the polar angle of the track and then independently of track momentum. The change in R_b in these cases was assumed to give an upper limit on the errors that could be present due to the neglect of other variables with less impact on the ALEPH tracking. The changes in R_b were added in quadrature to give the systematic error from this source — $\Delta R_b = 0.04\,\%$. The errors are shown in Table 7.2.

Secondly, tracks were treated independently, tuning the smearing and track removal parameters according to distributions of individual tracks. In calculating the tag variable, χ, information from many tracks is used. If the corrections ought to be correlated between tracks in an event, the Monte Carlo may still not accurately represent the data. For example, if the tracking was poorly simulated in one region of the detector (perhaps due to some fault in one module of the VDET), then if a jet fell in this region, smearing and track removal corrections should be applied in a correlated manner to a large proportion of the tracks in that jet. Conversely, corrections should be applied to a smaller proportion of the tracks that did not fall inside this region of the detector.

To obtain an estimate of the error from possible correlation effects between tracks, a negative hemisphere tag was used. For this, the sign of S_D is reversed for every track in the hemisphere. Then the negative-tag variable, χ_{neg}, is calculated from these reversed tracks in the same way as the standard tag variable, χ, is obtained from the original tracks. Because it is constructed using tracks with negative impact parameter, the negative-tag depends mainly on the detector resolution, without significant uncertainties from b and c physics. Counting the number of hemispheres which satisfy a cut on χ_{neg} at the same point as the cut on χ used in the measurement of R_b allows the negative hemisphere tag efficiency, ϵ_{neg}, to be calculated. This gives an estimate of the rate at which hemispheres containing no lifetime are tagged because of the imperfect detector resolution. The effects of the smearing and track removal corrections on the negative-tag efficiency give an indication of their effects on the standard tag.

Figure 7.4 shows the discrepancy in ϵ_{neg} between data and Monte Carlo, both with and without implementation of smearing and track removal corrections. These corrections have been tuned to match the distributions of individual track properties between data and Monte Carlo. Thus any disagreement in the values of ϵ_{neg}, once smearing and track removal corrections have been applied, can be interpreted as being

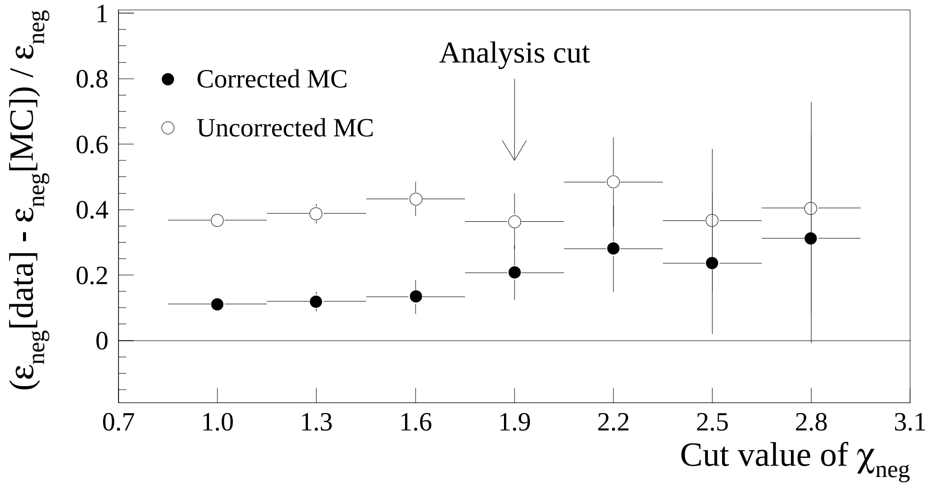

Figure 7.4: *Example of the difference in negative-tag efficiency, ϵ_{neg}, between data and Monte Carlo (MC), normalized to negative-tag efficiency in data and shown as a function of the cut on the negative-tag variable. Results without tracking corrections to the Monte Carlo are shown as white circles, results with corrections applied are shown as dark circles.*

the a result of combining information from individual tracks into a hemisphere tag variable. A scaling factor δ is defined:

$$\delta = \frac{\epsilon_{neg}(C) - \epsilon_{neg}(data)}{\epsilon_{neg}(\not{C}) - \epsilon_{neg}(data)} \tag{7.1}$$

where C and $\not{C}$ denote Monte Carlo with smearing and track removal corrections applied and not applied respectively. Where the statistical error on δ is larger than the value itself, δ is instead set equal to this error. At the cut $\chi = 1.9$ used for this analysis, a value of 0.5 was obtained for δ.

The systematic uncertainty in the value of R_b due to possible correlation effects between tracks in the smearing process was taken to be:

$$\Delta(R_b) = (R_b(S) - R_b(\not{S})) \cdot \delta\,, \tag{7.2}$$

where S and $\not{S}$ denote Monte Carlo with smearing corrections applied and not applied. An analogous expression was used to estimate the systematic uncertainty due to possible correlation effects in the track removal. The total systematic uncertainty in the value of R_b resulting from these estimations is $\Delta R_b = 0.09\,\%$.

Source	$\Delta R_b / \%$
Track removal θ dependence	0.012
Track removal momentum dependence	0.017
Track removal correlation effects	0.060
Smearing θ dependence	0.011
Smearing momentum dependence	0.026
Smearing correlation effects	0.066
Total error from detector simulation	0.10

Table 7.2: *Systematic errors on R_b due to uncertainties in the detector simulation.*

The contributions to the systematic error on the value of R_b from uncertainties in the detector simulation are shown in Table 7.2. A total error of $\Delta R_b = 0.10\,\%$ is estimated to result from uncertainties in the detector simulation. Almost all of this is due to possible correlation effects between tracks in the track removal and impact parameter smearing corrections.

7.1.4 Further studies

It is not ideal to perform the track removal and smearing corrections once the primary vertex has been reconstructed, since the resolution and error on the primary vertex position are important factors in the impact parameter significance. With a primary vertex-finding algorithm that reconstructs two vertices per event, it is possible to compare the distribution of their separation between data and Monte Carlo and check if this effect is significant (Figure 7.5).

One of the most intractable of the systematic errors in the value of R_b was connected with how well the Monte Carlo simulates the error on the reconstructed primary vertex position. In an attempt to reduce this uncertainty, the possibility of smearing track impact parameters before finding the primary vertex was investigated. This is more complicated than the ordinary procedure, since the b-tag uses only the 3-dimensional impact parameter significance of tracks, whilst the primary vertex reconstruction uses separately the impact parameters in the $r\phi$ plane and along the z axis, d_0 and z_0 respectively. In addition, more tracks are used in finding the primary vertex than in the tag, and for some of them only the component transverse to the jet direction is used, as described in Section 5.3.

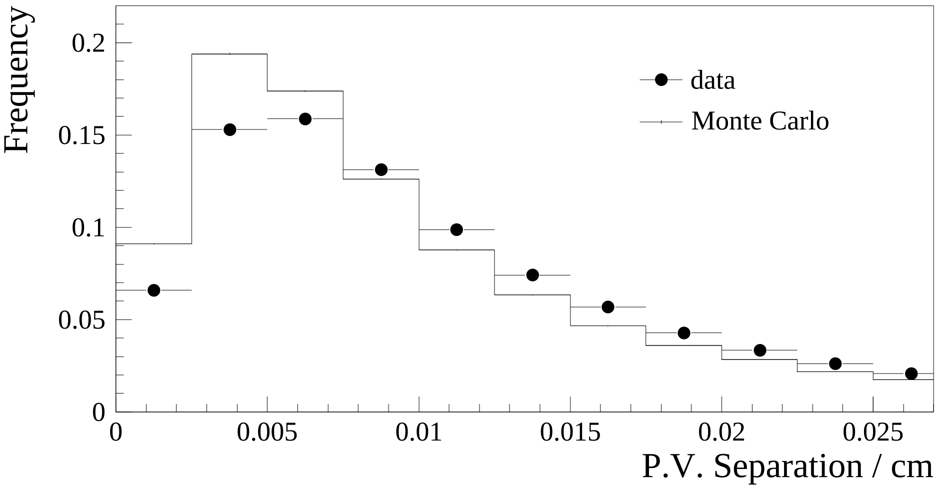

Figure 7.5: *Distribution of the separation between the two reconstructed primary vertices in an event, normalized to the number of events, for data (dark circles) and Monte Carlo (histogram).*

Smearing was applied to tracks using the same procedure and functions as described in Section 7.1.1, extended to two dimensions to cover both d_0 and z_0. This 2-dimensional smearing required a fit to eight parameters (two amplitudes and two exponential distributions for each dimension). A further two amplitudes were added to allow for correlated effects between d_0 and z_0. When a 2-dimensional plot of $d_0/\sigma(d_0)$ vs. $z_0/\sigma(z_0)$ was divided into 168 bins and compared between data and Monte Carlo, a χ^2 per degree of freedom of 18 was obtained. A χ^2 minimisation technique was used to obtain 10 smearing parameters which were then used to apply the 2-dimensional smearing corrections. The most significant part of the smearing to emerge from the fit were the amplitudes correlating the smearing between d_0 and z_0. After this, the χ^2 per degree of freedom obtained was 4. Although this was an improvement on the original situation, the Monte Carlo distribution still did not appear to give a good fit to the data.

There are several potential explanations for the failure of the 2-dimensional smearing procedure to result in a good fit between Monte Carlo and data. The choice of two exponential distributions in each dimension along with two correlating amplitudes may have been inappropriate. Alternatively, the problems of making a simultaneous fit to ten parameters may have resulted in a sub-optimal set of parameters.

Unfortunately, the timescale of the analysis did not permit further investigations into alternative forms of smearing or more appropriate fitting procedures. The systematic errors associated with the disagreement between data and Monte Carlo in the distribution of $d_0/\sigma(d_0)$ vs. $z_0/\sigma(z_0)$ are accounted for by the standard smearing procedure described in Section 7.1.1 and by the treatment of the correlation due to the error on the reconstructed primary vertex position described in Section 7.4 . However, the problems of the error on the measured primary vertex position and of the uncertainties associated with impact parameter smearing are two of the most significant in this analysis. Thus, the possibility of smearing track impact parameters before finding the primary vertex could be a useful suggestion for future work in this area.

7.2 Uncertainties in non-B physics

The most important systematic error to propagate through the predicted charm and light quark efficiencies is the uncertainty associated with detector resolution. However, it is also necessary to allow for our imperfect knowledge of the physics parameters used as input to the Monte Carlo simulation. In order to do this, weights were applied to the Monte Carlo events so that physics parameters such as the lifetimes of D hadrons were changed from the values used in producing the events to values that took into account the most recent experimental measurements. The uncertainties on these measurements were used to derive a systematic error by varying the parameters within their measured errors and noting the effect on R_b.

Almost all of the sources of uncertainty mentioned in this section propagate to R_b through ϵ_c and ϵ_{uds} alone. The uncertainties in the lifetimes of charm hadrons and in the rate of gluon splitting to heavy quarks also propagate through ρ_b, but contribute very little to the systematic error on R_b. The effects of all these sources of uncertainty are shown in Section 7.2.8 .

7.2.1 Production fractions in c events

The different lifetimes and decay multiplicities of D^0, D^+, $\mathrm{D_S}$ and Λ_C lead to different tag efficiencies, so that their relative abundances in c events strongly affect the overall value of ϵ_c.

In earlier analyses, the production fractions of the different species were taken from CLEO and ARGUS measurements [37] made below the $\Upsilon(4\mathrm{S})$ threshold. This assumed that those values were appropriate for the higher energy. Recently, direct measurements at LEP [38–41] have provided more precise values and removed the need for such an assumption. Table 7.3 shows the relative production rates of the different charm hadron species in the new LEP measurements.

	f_{D^0}	f_{D^+}	$f_{\mathrm{D_S}}$	$f_{\mathrm{D}_{\mathrm{baryon}}}$	R_c
Value	0.600	0.233	0.102	0.065	0.172
Error		0.028	0.037	0.029	0.017
Correlation matrix					
f_{D^+}		1.00	-0.36	-0.24	-0.19
$f_{\mathrm{D_S}}$		-0.36	1.00	-0.14	0.39
$f_{\mathrm{D}_{\mathrm{baryon}}}$		-0.24	-0.14	1.00	0.29
R_c		-0.19	0.39	0.29	1.00

Table 7.3: *Production rates of charmed hadrons, based on LEP measurements: values, errors and correlation matrix.*

In estimating the systematic uncertainty due to the charm production fractions, the total sample composition was parameterised in terms of f_{D^+}, $f_{\mathrm{D_S}}$ and $f_{\mathrm{D}_{\mathrm{baryon}}}$ — the fractions of charm hadrons which are $\mathrm{D}^{\pm}$, $\mathrm{D_S}$ and charmed baryons respectively. The fraction of D^0, $f_{\mathrm{D}^0} = N(\mathrm{D}^0)/N(\mathrm{D})$, was written as:

$$f_{\mathrm{D}^0} = 1 - f_{\mathrm{D}^+} - f_{\mathrm{D_S}} - f_{\mathrm{D}_{\mathrm{baryon}}} \tag{7.3}$$

This choice was purely technical, since all the uncertainties in the measured production rates were included by means of the correlation matrix.

The central values for these parameters, their errors and their correlation matrix, shown in Table 7.3, were derived from a combination of the LEP measurements. The resulting uncertainty in the value of R_b is $\Delta R_b = 0.023\,\%$.

7.2.2 Charm lifetimes

Since the probability to tag b or c events depends on the lifetime of the heavy quarks, knowledge of the charmed hadron lifetimes is essential for estimating ϵ_c and ρ_b. Events were reweighted so that the average charm lifetimes in the simulated events were equal to the latest Particle Data Group [9] values (see Table 7.4). The uncertainties in these values propagate to give an error on R_b through both ϵ_c and ρ_b. However, the lifetime measurements are very precise, keeping the corresponding uncertainty in the value of R_b small — $\Delta R_b = 0.010\,\%$.

Hadron type	Lifetimes / ps
D^0	0.415 ± 0.004
D^+	1.057 ± 0.015
$\mathrm{D_S}$	0.467 ± 0.017
Λ_C	0.206 ± 0.012

Table 7.4: *Lifetimes of charmed hadrons.*

7.2.3 Charm fragmentation

The impact parameter error, $\sigma(D_{min})$, and therefore the impact parameter significance, $S_D = D_{min}/\sigma(D_{min})$, depend on the track momentum. Thus, the fragmentation of the charm quark can affect the tag efficiency via the momentum spectrum of its decay products. The Peterson fragmentation parameter was varied by applying weights to the Monte Carlo events so that the mean energy of the weakly-decaying charmed hadron was $\langle E_C \rangle = (0.484 \pm 0.008) E_{CM}/2$, where E_{CM} is the centre of mass energy of the collision. This is the value recommended by the LEP Electroweak Working Group [41]. The resulting uncertainty in the value of R_b is small — $\Delta R_b = 0.003\,\%$.

7.2.4 Decay multiplicities

The different decay modes of a given hadron can have different tag efficiencies, depending on the number of decay products and how many of these are charged. However, there is no complete set of measurements of the exclusive branching ratios for any charmed hadron type. In addition, they decay into a large number of channels with very small branching ratios. To establish significant differences between the exclusive channel efficiencies in the Monte Carlo simulation, the statistics would need to be much larger than the sample currently available. Because of this, some assumptions are made.

Since the tag is principally based on information from charged tracks, decay modes are divided into topological channels according to the number of charged decay products. Most of the differences in tag efficiency between the different decay modes are expected to be accounted for in this manner. Inclusive topological branching ratios have been measured by MARK III [42] for D^0, D^+ and $\mathrm{D_S}$ and are shown in Table 7.5.

Hadron type	N of charged decay products	Branching ratios measured
D^0	0	0.054
	2	0.634
	4	0.293
	6	0.019
D^+	1	0.384
	3	0.541
	5	0.075
$\mathrm{D_S}$	1	0.37
	3	0.42
	5	0.21

Table 7.5: *Topological branching ratios of charmed hadrons.*

As with the production ratios, the sum of the topological branching ratios is constrained to be 1. Thus, the largest channel was again written in terms of the others, whose errors and correlation coefficients were used to propagate the error to R_b. The systematic error due to uncertainties in the topological branching ratios is $\Delta R_b = 0.014\,\%$.

The MARK III analysis included tracks from $\mathrm{K^0_S}$ decays in the number of charged tracks of the topological channels, without identifying their origins. However, $\mathrm{K^0_S}$ mesons in ALEPH often decay far from the primary vertex and are identified as long-lived neutral particles. Because of this, the rate of events containing $\mathrm{K^0_S} \rightarrow \pi^+\pi^-$ within each topological channel must be taken into account when estimating the charm efficiency. Table 7.6 shows the experimental values of the inclusive branching ratios $\mathrm{D} \rightarrow \mathrm{K^0_S X}$ used, which are those given by the Particle Data Group [9].

Branching ratio	Measured value
$\mathrm{BR(D^0 \rightarrow K^0_S}X)$	0.210 ± 0.025
$\mathrm{BR(D^+ \rightarrow K^0_S}X)$	0.295 ± 0.035
$\mathrm{BR(D_S \rightarrow K^0_S}X)$	0.195 ± 0.140

Table 7.6: $\mathrm{K^0_S}$ *rates in charm hadron decays.*

Weights were applied to events containing a $\mathrm{K^0_S}$ to make the branching ratio in the Monte Carlo match the value shown. Care was taken that the total branching ratios for each channel were kept constant, by applying appropriate weights to the exclusive channels which did not contain a $\mathrm{K^0_S}$. Experimental data on how the $\mathrm{K^0_S}$ production from a given charmed hadron is divided amongst the topological channels is not available, so the Monte Carlo predictions were used. The effect on the value of R_b due to uncertainty in the $\mathrm{K^0_S}$ rate in charm hadron decays is $\Delta R_b = 0.015\,\%$.

7.2.5 Further studies of charm decays

The major influences on the tag efficiency should be accounted for by the reweighting of topological decay channels and $\mathrm{K^0_S}$ production rates, as described in the previous section. However, it is necessary to check that details of the exclusive decay modes within each topological channel do not significantly affect the tag. Since the most likely reason for such an effect is the number of neutral particles, each topological channel, producing i charged tracks, was further split into four sub-channels according to the number of neutral decay products. As there are no experimental values available for the branching ratios to each of these sub-channels, they were taken from the Monte Carlo. If the branching ratio to j neutral particles within the i^{th} topological channel is designated η^i_j, where $\sum_j \eta^i_j = 1$, and the error on the value of the topological branching ratio B_i is σ_i, the error on η^i_j was arbitrarily taken to be $\sigma^i_j = \sqrt{\eta^i_j}\sigma_i/B_i$. The intention here was to simulate the fact that the larger exclusive branching ratios are more precisely known. As with the production rates and the topological branching ratios, the largest channel was written in terms of the others, which were varied independently so that the sum was constrained to be 1.

It is clear that this procedure does not give a quantitative estimate for the systematic error due to differences in efficiency between exclusive channels within one topological channel. However, it does provide a useful order of magnitude estimate for the size of the effect ($\Delta R_b = 0.019\,\%$) which, whilst not being negligible, is still small in comparison with other sources of uncertainty.

7.2.6 Gluon splitting to heavy quarks

The tag efficiency of c and uds events can be affected by the production rate of $b\bar{b}$ and $c\bar{c}$ pairs from radiated gluons. In order to evaluate the systematic uncertainty in R_b from $N(\mathrm{g} \to c\bar{c})$, the rate predicted by JETSET, $N(\mathrm{g} \to c\bar{c}) = 1.6 \times 10^{-2}$

per hadronic event was reweighted to the rate measured by OPAL [43] $N(\mathrm{g} \to c\bar{c}) = (2.38 \pm 0.48) \times 10^{-2}$. The rate of $\mathrm{g} \to b\bar{b}$ had not been measured at the time when the LEP Electroweak Working Group recommendations [41] were formulated. However, theoretical studies [44] suggest that $N(\mathrm{g} \to b\bar{b}) = (0.13 \pm 0.04) \times N(\mathrm{g} \to c\bar{c})$ and this was the value used. A subsequent preliminary measurement from DELPHI [45] gives a value of $N(\mathrm{g} \to b\bar{b}) = (0.22 \pm 0.13) \times 10^{-2}$, which is in agreement with this assumption.

The systematic errors in the value of R_b due to uncertainties in the rate of gluon splitting to heavy quarks are $\Delta R_b = 0.034\,\%$ from $N(\mathrm{g} \to c\bar{c})$ and $\Delta R_b = 0.054\,\%$ from $N(\mathrm{g} \to b\bar{b})/N(\mathrm{g} \to c\bar{c})$. These are the two largest systematic errors arising from uncertainties in non-B physics. The large impact of the uncertainty in the rate of gluon splitting to charm quarks is due to the effect it has on the value assumed for $N(\mathrm{g} \to b\bar{b})$.

7.2.7 Long-lived neutral particles

Aside from gluon splitting to heavy quarks, a *uds* events might tag due to the presence of V^0's — long-lived neutral particles, such as K^0_S or Λ^0, that decay into a pair of charged particles. A systematic uncertainty arises from our imperfect knowledge of the rate at which such particles are produced. In order to obtain an estimate of this error, events were reweighted according to the number of V^0's they contained, varying the average number by ±10 % from the central value predicted by the Monte Carlo. This variation is expected to be large enough to account for uncertainty in the production rate and momentum spectrum of such particles. In any case, the effect on R_b is small — $\Delta R_b = 0.004\,\%$.

Another source of uncertainty was the reconstruction of V^0's within the b-tag algorithm. In this, pairs of charged tracks consistent with being the decay products of a long-lived neutral particle are identified. Such tracks are eliminated from the tag and in some cases the reconstructed V^0 is used as a track. If the efficiency of this reconstruction process was poorly simulated in Monte Carlo, the prediction of ϵ_{uds} could be affected. In order to obtain an estimate of the systematic uncertainty arising from this source, the detection rate of V^0's was reduced by 20 % in the Monte Carlo. This was done by ignoring 20 % of V^0 reconstructions. The observed effect on the value of R_b was taken as the systematic uncertainty and was found to be small — $\Delta R_b = 0.009\,\%$.

7.2.8 Estimated systematic errors

Table 7.7 shows the systematic error in R_b resulting from uncertainties in non-B physics. It can be seen that the major sources of error are the uncertainties in the rates of gluon splitting to heavy quarks. The uncertainty in the relative production rates of charmed hadrons is also significant. The total systematic error from uncertainties in non-B physics is $\Delta R_b = 0.07\,\%$.

Source	$\Delta R_b/\%$
c hadron production rates	0.023
c hadron lifetimes	0.010
c fragmentation	0.003
c hadron topological branching ratios	0.014
$c \rightarrow \mathrm{K}^0_\mathrm{S}$ rate	0.015
No. of neutrals in c hadron decays	0.019
$\mathrm{g} \rightarrow c\bar{c}$ rate	0.034
Ratio $(\mathrm{g} \rightarrow b\bar{b})/(\mathrm{g} \rightarrow c\bar{c})$	0.054
V^0 production rate	0.004
V^0 tag rate	0.009
Total error from non-B physics	0.07

Table 7.7: *Systematic errors on R_b due to uncertainties in non-B physics parameters used as inputs to the Monte Carlo.*

7.3 Uncertainties in B physics

Since the efficiency for tagging b events is eliminated from the equations used by the double tag method, the only way for the Monte Carlo simulation of B physics to affect R_b is through the prediction of the hemisphere-hemisphere correlation. This section describes the estimation of the systematic uncertainty in the value of ρ_b due to uncertainties in B physics, whilst Section 7.4 outlines the means by which other correlation effects were quantified. The method used here is the same as that described in Section 7.2 — Monte Carlo events were weighted so that the average values of quantities such as B hadron lifetimes matched between data and Monte Carlo.

The uncertainties on the measured B physics parameters need to be propagated to give an uncertainty on R_b. This was done by altering the weights applied to Monte Carlo events so that the mean value of the parameter under consideration was shifted by its specified error. The resulting change in R_b is an indication of the systematic error due to the uncertainty in this parameter. However, the sources of uncertainty considered in this section propagate to R_b through their effect on ρ_b, whose statistical error depends mainly on the number of doubly-tagged events. Because this statistical error is comparatively large, it can be hard to distinguish between a genuine change in ρ_b, due to the shift in the mean value of the parameter under consideration, and a statistical fluctuation, due merely to the changing event weights. Thus, for each source, the mean value of the parameter was altered and both the shift in R_b and the statistical error on this shift were observed. The systematic uncertainty in R_b was assumed to be the larger of these two quantities.

As described in Section 4.3, efficiency correlations can arise through the orientation of the event in the detector or the residual effects of the shared beam-spot. In addition, the physics properties of the B hadrons can have an effect, either due to an intrinsic correlation between the hemispheres or through the impact which a change in ϵ_b might have on the average value of ρ_b.

7.3.1 B hadron fragmentation

The momentum spectrum of the weakly decaying B hadrons affects the hemisphere-hemisphere correlation, since high-momentum tracks undergo less multiple scattering and hence there is less uncertainty in the value of their impact parameters. The mean energy of the weakly decaying B hadron was adjusted so that it conformed with $\langle E_B \rangle = (0.702) E_{CM}/2$, where E_{CM} is the LEP centre of mass energy, by altering the ϵ parameter in the Peterson fragmentation function. It was then changed to vary the spectrum according to $\Delta \langle E_B \rangle = (\pm 0.008) E_{CM}/2$, the error on the measured mean energy. These were the values recommended by the LEP Electroweak Working Group [41]. The effect of the uncertainty in the mean energy of the B hadrons on the value of R_b is $\Delta R_b = 0.013\,\%$. This results from the statistical error on the shift in R_b, since the shift itself is compatible with zero.

Before the introduction of two reconstructed primary vertices for each event, the effect on R_b was of order $\Delta R_b = 0.1\,\%$. The reason for this large correlation is that when fragmentation is hard, the B hadron travels a long distance before decaying. This degrades the resolution of the shared primary vertex, so that the opposite hemisphere is unlikely to tag, creating a negative correlation. When two primary vertices are used, the B hadron fragmentation may still affect the average value of ρ_b through its effect on the tagging efficiency, ϵ_b.

7.3.2 B hadron production fractions

The different lifetimes and decay properties of the various B hadrons result in different tagging efficiencies, which can affect the average value of ρ_b. Because of this, the relative proportions of the different species in the Monte Carlo were tuned to reproduce those measured by ALEPH [46]. Table 7.8 shows these values.

In estimating the uncertainty associated with the errors on these proportions, the fact that the only independent measurements are the B_S and B baryon fractions must be taken into account. Thus, the fractions of B^+ and B^0 were assumed to be equal and the variations of the B_S and B baryon fractions were compensated by varying the B^+ and B^0 fractions. The resulting effect on R_b is $\Delta R_b = 0.015\,\%$.

Species	ALEPH measurement
B^+	0.382
B^0	0.382
B_S	0.122 ± 0.03
B baryons	0.115 ± 0.04

Table 7.8: *B hadron production fractions.*

7.3.3 B hadron lifetimes

The lifetime of a B hadron will affect its tagging probability and hence ρ_b. The B lifetimes were modified according to the values given in reference [46] and shown in Table 7.9. The systematic error on R_b from uncertainties in the B hadron lifetimes is $\Delta R_b = 0.013\,\%$.

Species	Lifetime/ps
B^0	1.58 ± 0.06
B^+	1.65 ± 0.06
B_S	1.55 ± 0.11
B baryons	1.20 ± 0.08

Table 7.9: *B hadron lifetimes.*

7.3.4 B hadron charged decay multiplicity

Following the prescriptions of the LEP Electroweak Working Group, the average charged decay multiplicity of the B hadrons was adjusted to match the measurements made by OPAL and DELPHI [41,47,48]: 5.73 ± 0.35. Clearly, the number of charged tracks produced in the decay of a B hadron will affect the tag probability. The resulting systematic error on R_b from this source is $\Delta R_b = 0.021\,\%$, one of the largest from uncertainties in B physics. Before the introduction of separate primary vertices for each hemisphere, the systematic error from this source was of order $\Delta R_b = 0.1\,\%$.

7.3.5 Hard gluon emission

In about $2\,\%$ of events, a hard gluon is emitted, forcing the two B hadrons into the same hemisphere. When this happens, the hemisphere containing the two B's will probably tag, whilst the opposite hemisphere is unlikely to do so. Thus, this source contributes a negative correlation in tagging efficiency. On comparing the Lund Parton Shower and Lund Matrix Element predictions for this process, a $30\,\%$ difference is found, which was taken as error. The central value was taken from the Parton Shower model. The systematic error on the value of R_b due to this source of uncertainty is $\Delta R_b = 0.023\,\%$, one of the larger errors from uncertainties in B physics.

7.3.6 Estimated systematic errors

Source	Shift in ρ_b with stat. error	Syst. error assumed for ρ_b	$\Delta R_b/\%$
B fragmentation	-0.022 ± 0.059	± 0.059	0.013
B_s fraction	-0.024 ± 0.035	± 0.035	0.008
Λ_b fraction	0.060 ± 0.045	± 0.060	0.013
B hadron lifetime	-0.060 ± 0.015	± 0.060	0.013
B multiplicity	-0.096 ± 0.065	± 0.096	0.021
Hard gluon emission	-0.106 ± 0.007	± 0.106	0.023
Total error from B physics			0.04

Table 7.10: *Systematic errors on ρ_b with statistical errors. The larger of the shift and its statistical error is taken as the contribution to the systematic error, which propagates to an error on R_b.*

Table 7.10 summarises the uncertainties on the value of R_b due to B physics. The major sources of uncertainty are the B hadron decay multiplicity and the rate of hard gluon emission, where both b quarks are forced into the same hemisphere. Note that the systematic error on ρ_b, propagated to R_b through Equation 4.7, is assumed to be the shift in ρ_b when the Monte Carlo is reweighted or the statistical error on this shift, whichever is the larger. The total systematic error on R_b due to uncertainties in B physics is $\Delta R_b = 0.04\,\%$.

7.4 Further studies of correlation

In the previous section, the effect on R_b of uncertainties in B hadron physics was discussed. These uncertainties can propagate to R_b only through the correlation, ρ_b. In addition, there are further uncertainties in ρ_b which arise from the interplay of detector effects and event shape characteristics, as mentioned in Section 4.3 . For example, the back-to-back nature of the events and the limited acceptance of the vertex detector in polar angle mean that tracks are likely to fall mainly in regions of good (or poor) VDET coverage. This effect causes a positive correlation in the b-tag for the two sides.

In order to study the contribution of these remaining effects to the uncertainty in the correlation, a method similar to that of reference [36] was used. This tries to isolate components of the correlation due to particular physical causes and compares the results for data and Monte Carlo. The variables, defined for each hemisphere, were chosen to be sensitive to the physical effects responsible for the b-tag correlation.

7.4.1 Correlation components

The correlation components were obtained using a method based on the combination of two distributions. The first of these, $E(\nu)$, is the efficiency of the tag as a function of ν, where ν is any variable which might affect ρ_b, such as the polar angle of the thrust axis. The variable ν is measured in the hemisphere in which the tag is applied. The second, $F(\nu)$, is the probability distribution of ν obtained after requiring a tag in the hemisphere opposite to that where ν is measured.

Figure 7.6 illustrates these distributions for the variable P_{jet} — the momentum of the leading jet in a hemisphere. Figure 7.6 a shows the 2-dimensional distribution of P_{jet} in the two hemispheres. There is a positive correlation of order 20 %. Figure 7.6 b

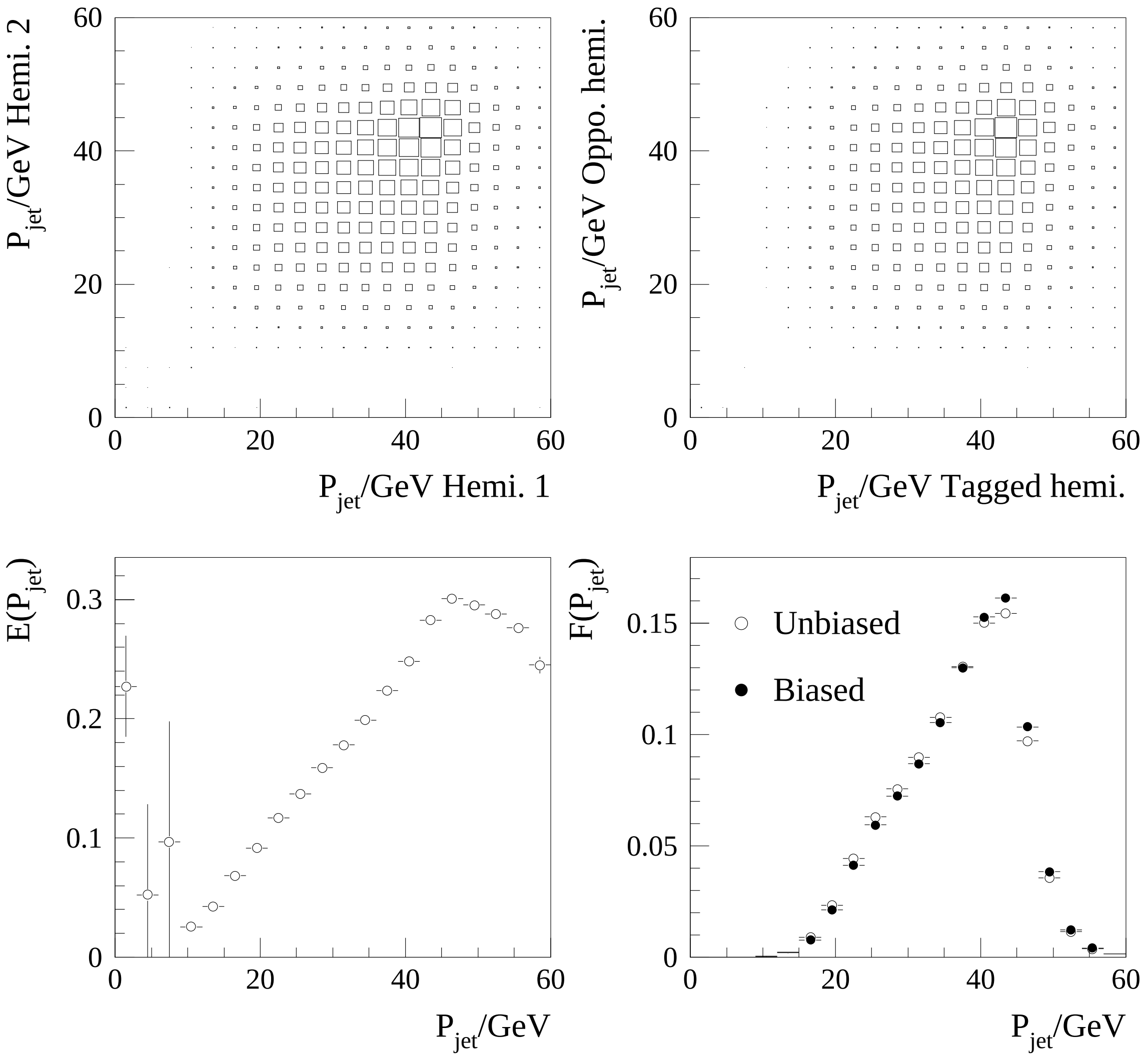

Figure 7.6: *Correlation of jet momentum, P_{jet}, in Monte Carlo b events.*
Top left: a) 2-dimensional distribution of P_{jet} in the two hemispheres.
Top right: b) 2-dimensional distribution of P_{jet} in a hemisphere passing the b-tag cut at $\chi = 1.9$ and P_{jet} in the opposite hemisphere.
Bottom left: c) Tag efficiency as a function of P_{jet}.
Bottom right: d) Distribution of P_{jet} unbiased (white circles) and biased by requiring that the opposite hemisphere passes the b-tag (dark circles).

shows the distribution after a b-tag cut requiring $\chi > 1.9$ has been applied to one hemisphere. Here, the value of P_{jet} in the hemisphere opposite to the tag is shown plotted against the value of P_{jet} in the tagged hemisphere. The tag efficiency as a function of P_{jet}, $E(P_{jet})$, varies as shown in Figure 7.6 c. Because of the correlation between values of P_{jet} in opposite hemispheres, the probability distribution in the hemisphere opposite to the one containing the tag is biased. The biased distribution is $F(P_{jet})$. Figure 7.6 d shows the probability distributions before and after a tag is applied in the opposite hemisphere. They differ by up to 10 %.

By combining the distributions $E(\nu)$ and $F(\nu)$, the efficiency, ϵ_ν, of tagging the second hemisphere after having tagged the first can be found as an integral over ν:

$$\epsilon_\nu \equiv \int E(\nu) \cdot F(\nu)\, d\nu\,. \tag{7.4}$$

The correlation component for the variable ν can then be computed, making use of the efficiency for tagging b hemispheres, ϵ_b:

$$\rho_\nu = \frac{\epsilon_\nu - \epsilon_b}{\epsilon_b} \tag{7.5}$$

This represents the fact that the presence of a tag in the opposite hemisphere can alter the distribution of a given variable. If the tag efficiency changes as a function of this variable and there is a correlation between values of this variable in the two hemispheres, a correlation in tagging efficiency is created. For the variable P_{jet}, the correlation in b events is $\rho(P_{jet}) = (1.27 \pm 0.03)\,\%$ for a cut at $\chi = 1.9$.

If a complete set of independent variables could be identified which described the sources of correlation, then the sum of their component correlations should be equal to the total b-tag correlation. However, this is only correct if the variables are totally uncorrelated amongst themselves, which is rarely the case. For example, seemingly unrelated variables such as the polar angle, θ, of the thrust axis and the error in the position of the primary vertex projected on the plane perpendicular to the thrust axis, σ_T, are correlated (Figure 7.7). This is because if the thrust axis is at a low polar angle, the poorer track resolution degrades the primary vertex error.

The effect of this connection between the variables can be studied by looking at the correlation component obtained directly for two variables from the corresponding 2-dimensional distribution. Figure 7.8 shows the sum of the correlation components for $\nu = \cos\theta$ and $\nu = \sigma_T$ as a function of the cut on the tag variable χ. This is compared to the correlation component $\rho_{\mu\nu}$ obtained by considering a 2-dimensional

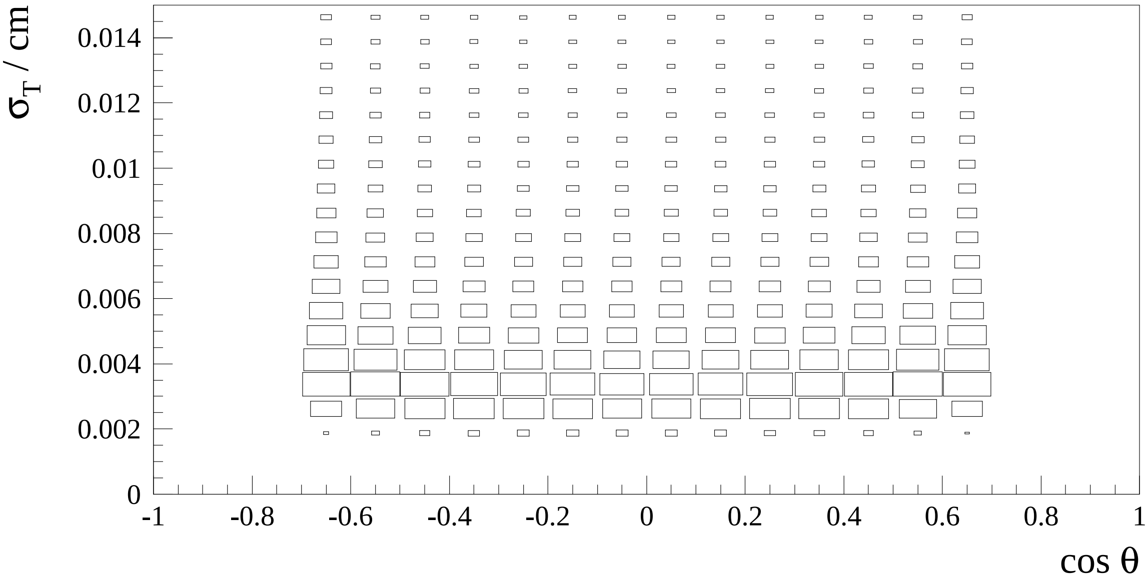

Figure 7.7: *Error on the position of the reconstructed primary vertex, projected transverse to the thrust axis, σ_T, as a function of the polar angle of the thrust axis, θ.*

distribution in $\mu = \cos\theta$ and $\nu = \sigma_T$:

$$\epsilon_{\mu\nu} \equiv \int E(\mu,\nu)\cdot F(\mu,\nu)\, d\mu\, d\nu\,, \tag{7.6}$$

$$\rho_{\mu\nu} = \frac{\epsilon_{\mu\nu} - \epsilon_b}{\epsilon_b}\,. \tag{7.7}$$

A further problem arises from the need to isolate b events in the data, in order to estimate the contribution of each of the components to the correlation. The quantity under investigation is the correlation of the tag between b hemispheres, so that the components are only meaningful when extracted from variable distributions in b events. If the distribution of ν was different for light quark events, then a sample containing a sizeable background of those events would yield an incorrect result for ρ_ν.

In order to reduce the contamination from *udsc* events in the data, a soft cut on the b-tag variable χ was applied. Both hemispheres were required to satisfy the soft cut, to avoid introducing an artificial hemisphere-hemisphere correlation. In addition to this, it was necessary to apply a correction to the data to allow for the remaining *udsc* background. There are two ways in which this correction can be made. The first

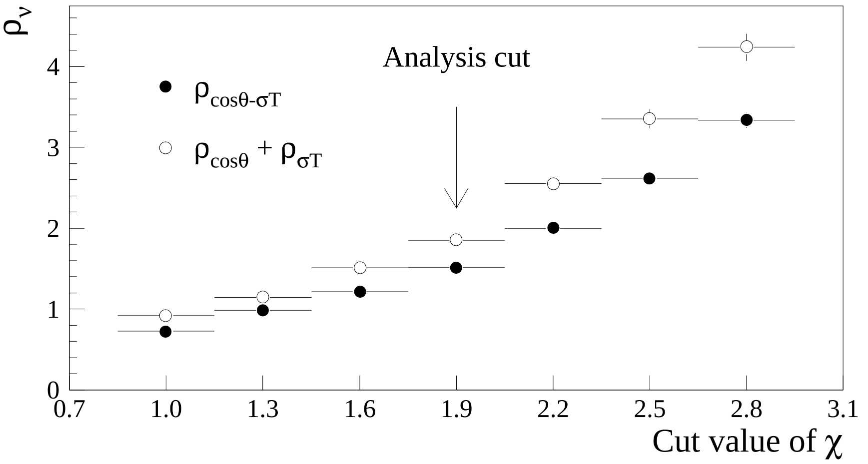

Figure 7.8: *Comparison between the sum of two individual correlation components (for* $\cos\theta$ *and* σ_T*) and the correlation component obtained using a 2-dimensional distribution.*

is performed in bins of the variable ν from the ratio of observed $Z^0 \to b\bar{b}$ to $Z^0 \to q\bar{q}$ events:

$$N_b^{\mathrm{data}}(\nu) \simeq N_q^{\mathrm{data}}(\nu) \times \frac{N_b^{\mathrm{MC}}(\nu)}{N_q^{\mathrm{MC}}(\nu)} \,. \tag{7.8}$$

For the second correction method, the number of *udsc* events observed in the Monte Carlo is subtracted from the number of events observed in the data, bin by bin, normalizing to the total number of events in data and Monte Carlo:

$$N_b^{\mathrm{data}}(\nu) \simeq N_q^{\mathrm{data}}(\nu) - (N_{udsc}^{\mathrm{MC}}(\nu) \times \frac{N_q^{\mathrm{data}}}{N_q^{\mathrm{MC}}}) \,. \tag{7.9}$$

In this way, it is possible to compare the component correlations due to a particular variable in Monte Carlo and data. The systematic uncertainty associated with the background subtraction process was estimated from the difference in the results obtained with the two correction methods. The central value of the correlation component in the data was taken to be average of the two.

The difference between the single variable correlation in $b\bar{b}$ Monte Carlo and in data, with a soft cut and background subtraction applied, was used to estimate a systematic uncertainty on the total correlation ρ_b. This process was repeated for several variables chosen to represent the different possible sources of correlation. However, because the soft cut selectively removes events, it biases the value of the correlation

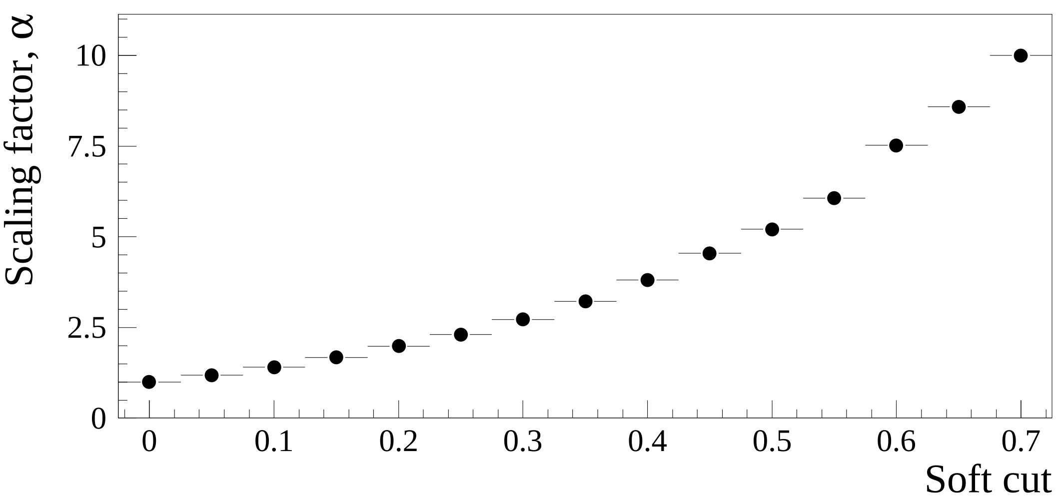

Figure 7.9: *Scaling factor α for the variable P_{jet}, as a function of soft cut.*

obtained, so that ρ_ν tends towards zero as the soft cut approaches the working cut used for tagging. Thus, if a strong soft cut was applied to improve the b-purity of the data sample used, the difference between data and Monte Carlo would be artificially reduced. Figure 7.10 shows single variable correlations in Monte Carlo b events and data as a function of soft cut. Background subtraction has been applied to the data. For each, it can be seen that the correlation, ρ_ν, approaches zero as the soft cut increases. It can also be seen that the uncertainty associated with background subtraction in the data decreases as a stronger soft cut results in a purer sample.

The bias introduced by the soft cut was taken into account by use of a scaling factor, α. This was defined as the ratio between the correlation obtained without and with the soft cut in place, as measured in Monte Carlo b events:

$$\alpha = \frac{\rho_\nu(b\bar{b},\ no\ soft\ cut)}{\rho_\nu(b\bar{b},\ soft\ cut)}\,. \tag{7.10}$$

For the example of P_{jet}, the scaling factor is shown in Figure 7.9 as a function of soft cut.

The scaling factor was applied to the data-Monte Carlo discrepancy observed at a given soft cut (or to the error on this discrepancy if larger), in order to give an estimate of the true discrepancy in an unbiased set of events:

$$\text{error} = \alpha \cdot (\rho_\nu(data,\ soft\ cut) - \rho_\nu(MC,\ soft\ cut))\,. \tag{7.11}$$

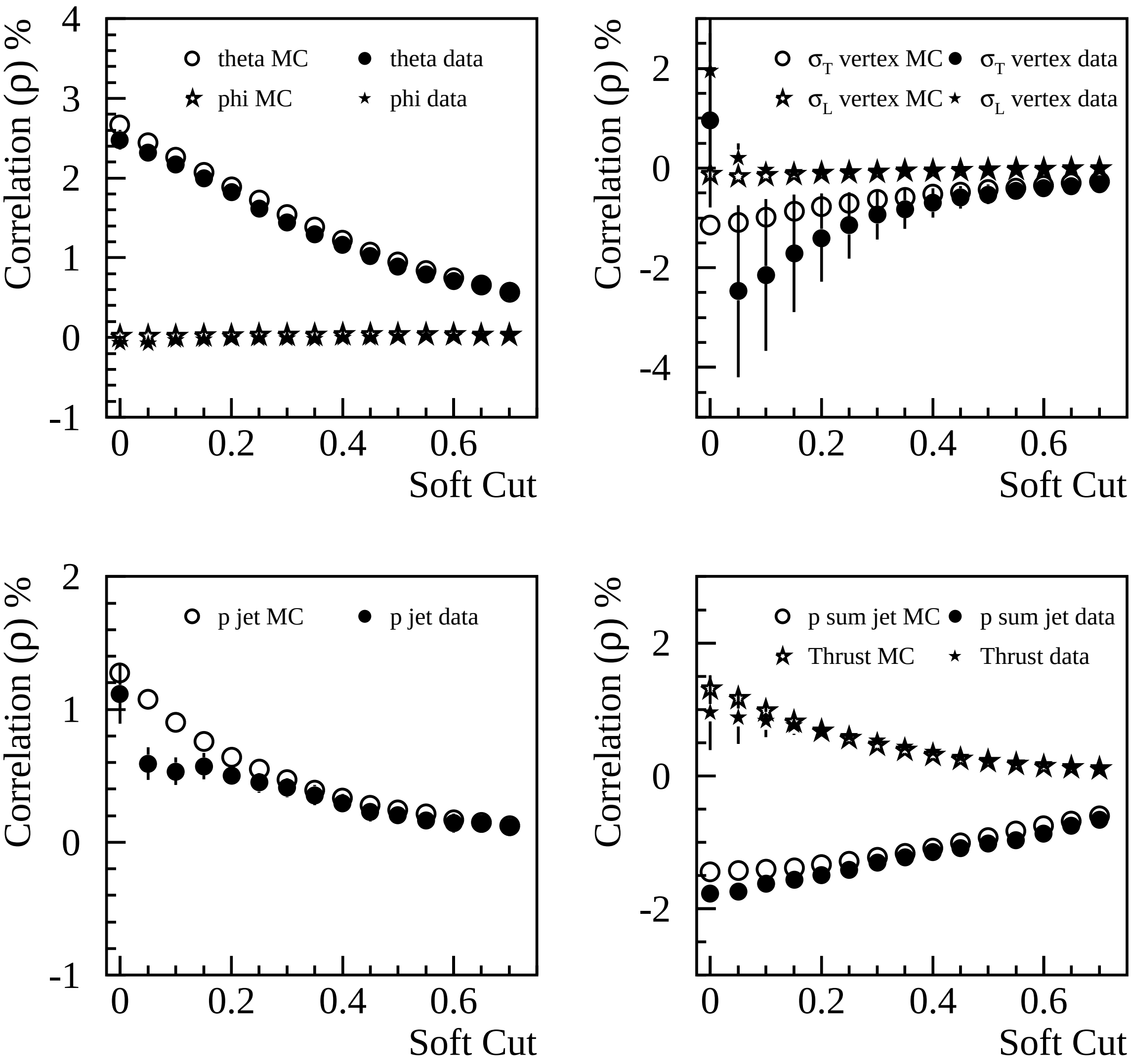

Figure 7.10: *Correlation components for data and Monte Carlo (MC) as a function of soft cut. The points for the data are the average of the results obtained with the two methods of background subtraction. The first plot shows the polar angle, θ, and the azimuthal angle, ϕ, of the thrust axis. The second plot shows the error on the position of the reconstructed primary vertices, projected along (σ_L) and perpendicular to (σ_T) the thrust axis. The third plot shows the jet momentum, P_{jet}. The fourth plot shows the vector sum of the jet momenta (p sum) and the value of the thrust.*

The error on the data-Monte Carlo discrepancy derives from statistics and background subtraction and generally decreases as the soft cut becomes stronger. However, at strong soft cuts, the scaling factor by which the discrepancy must be multiplied increases. Thus, the choice of soft cut must take both these factors into account.

7.4.2 Estimated systematic error

Using the method described above, the systematic uncertainty associated with a specific source of correlation can be estimated from the observed difference between data and Monte Carlo. However, this was only done for those sources which had not been accessed by the weighting procedures described in Section 7.3 .

The variables were chosen because they represented potential sources of correlation. In order to compare data and Monte Carlo, only variables which could be measured in data, based on reconstructed tracks and energy, were considered. The following variables were used, and the results are shown in Table 7.11 .

- Cosine of the thrust axis polar angle, $\cos\theta$, which quantifies the effects of the detector acceptance and dead regions.

- Azimuthal angle, ϕ, of the thrust axis, for non-uniformities in the azimuthal detector track efficiency and resolution due to dead regions.

- Errors on the position of the primary vertex, projected along and perpendicular to the thrust axis (σ_L and σ_T respectively). The primary vertex was re-

Correlation component	Soft cut	$\lvert\rho_{\mathrm{Data}} - \rho_{\mathrm{MC}}\rvert(\%)$	Scaling factor	Systematic in ρ_b (%)
Thrust polar angle ($cos\theta$)	0.05	0.11 ± 0.10	1.1	0.12
Thrust azimuthal angle (ϕ)	0.0	0.04 ± 0.02	1.0	0.04
σ vertex along thrust	0.15	0.05 ± 0.04	1.0	0.05
σ vertex $\perp$ to thrust	0.6	0.04 ± 0.14	3.2	0.36
Jet momentum	0.2	0.14 ± 0.07	2.0	0.22
Total systematic uncertainty in ρ_b				0.44
Total systematic uncertainty in R_b, $\Delta R_b/\%$				0.10

Table 7.11: *Difference in the variable correlation components for Monte Carlo b events and data with background subtraction at the b-tag cut* $\chi = 1.9$.

constructed independently for each hemisphere, but there was still a residual correlation due to the beam spot envelope.

- Vector sum of the track momenta in the leading jet of a hemisphere (jet momentum, P_{jet}). This describes the effect of gluon radiation. If a gluon is emitted, the leading jets both have lower momenta, implying lower tagging probabilities and causing a positive correlation.

These variables were used to estimate the systematic uncertainty in the value of the correlation. Further variables, such as those listed below, provided information about some sources of correlation, but were strongly linked to variables already studied, or to the effects of the variation of B physics parameters described in Section 7.3. They were therefore only used as a check that the systematic error was under control. The comparatively small discrepancies in ρ_b for these variables, shown in Table 7.12 indicate that this is indeed the case.

- Vector sum of the momenta of the two leading jets, given opposite signs for the two hemispheres. This quantity is sensitive to hard gluon radiation, which forces both B hadrons into the same hemisphere and induces a negative correlation.
- Thrust value, which is sensitive to the shape of 3-jet events and provides a cross-check of jet momentum.

Correlation component	Soft cut	$\lvert\rho_{\mathrm{Data}} - \rho_{\mathrm{MC}}\rvert$(%)	Scaling factor	Discrepancy in ρ_b (%)
Jet momentum sum	0.15	0.18 ± 0.06	1.1	0.19
Thrust value	0.3	0.07 ± 0.03	2.8	0.18

Table 7.12: *Difference in the variable correlation components for Monte Carlo b events and data with background subtraction at the b-tag cut* $\chi = 1.9$ *for the variables used as cross-checks.*

A further quantity, the displacement of the two reconstructed primary vertices from the true one, was studied in the Monte Carlo. The correlation from this source was found to be -0.2 %, about an order of magnitude smaller than the effect due to the primary vertex error.

The total systematic error in the value of R_b arising from the specific correlation uncertainties in Table 7.11 is $\Delta R_b = 0.10\,\%$. Together with the systematic error due to uncertainties in the detector simulation, this forms one of the largest sources of error in the measurement. Most of the error is due to uncertainty in the effect of the primary vertex transverse error, σ_T.

7.5 Other sources of systematic error

There remain some minor systematic errors due to uncertainties in the amount of background in the hadronic event sample and the flavour bias. These were estimated from the Monte Carlo and contribute a systematic error of $\Delta R_b = 0.01\,\%$. There is also an error from the Monte Carlo statistics, due to statistical errors on the predicted values of ϵ_c, ϵ_{uds} and ρ_b. The resulting uncertainty in the value of R_b is $\Delta R_b = 0.05\,\%$ and is almost entirely due to the statistical error on the value of ρ_b.

In addition, there is a systematic uncertainty due to the value of R_c used. The central value was fixed to $R_c = 17.1\,\%$. The change in R_b due to variation of R_c was then calculated according to Equation 4.8. The resulting systematic error in R_b is $\Delta R_b = (-0.037 \times [R_c - 17.1])\,\%$.

7.6 Summary

The largest sources of error in the value of R_b are the simulation of the detector in the Monte Carlo and uncertainties in the prediction of the hemisphere-hemisphere correlation in tagging efficiency.

Uncertainties in the simulation of the vertex detector have an impact on the background efficiencies ϵ_c and ϵ_{uds} and on the correlation, ρ_b. Corrections were applied to Monte Carlo events, so that the average number of tracks and the distribution of their impact parameter significance matched between data and Monte Carlo. A systematic error results from uncertainty about the accuracy of these corrections, due to possible dependence on tracking variables not considered and to ignoring any possible correlation effects between tracks in an event.

The effects of imperfectly known physics in uds, c and b events are also significant. Weights were applied to Monte Carlo events so that the average values of physics parameters in the simulation matched the best experimental results available. The uncertainties in these results were propagated to R_b by varying the event weights appropriately and noting the shift in the value.

There are further uncertainties in the value of the correlation, ρ_b, that are not accounted for by the reweighting of b events. The correlation due to a specific physical source was derived using a variable which reflected the source. The discrepancy between data and Monte Carlo leads to an estimate of the systematic error from the correlation due to that source.

A small systematic uncertainty results from correcting of the value of R_b for background and acceptance bias amongst the event flavours. A further uncertainty derives from the statistical error due to predicting the correlation, ρ_b, from a Monte Carlo sample of limited size. Finally, a systematic error results from the value chosen for R_c. When all sources of systematic error are included, the total systematic uncertainty in the measurement of R_b is $\Delta R_b = (\pm 0.17 - 0.037[R_c - 17.1])\,\%$. Table 7.13 summarises the constituent parts of this total along with the statistical uncertainty in R_b.

Source	Uncertainty in $R_b/\%$
Data statistics	± 0.11
Monte Carlo statistics	± 0.05
Detector simulation uncertainties	± 0.10
Non-B physics uncertainties	± 0.07
B physics uncertainties	± 0.04
Specific correlation uncertainties	± 0.10
Event selection uncertainties	± 0.01
Variation with R_c	$-0.037[R_c - 17.1]$

Table 7.13: *Sources of systematic and statistical uncertainty in the measurement of R_b.*

Chapter 8

Conclusions

Using 2.3 million Z^0 events collected with the ALEPH detector at LEP during the period 1992–95, the ratio $R_b = \Gamma_{Z^0 \to b\bar{b}} / \Gamma_{Z^0 \to hadrons}$ has been measured and found to be:

$$R_b = (21.72 \pm 0.11(stat.) \pm 0.17(syst.) - 0.037[R_c - 17.1])\,\%\,.$$

This lies within one standard deviation of the Standard Model prediction [49]:

$$R_b^{SM} = 21.58\,\%\,.$$

Along with the measurement of R_b presented here, another ALEPH measurement [4] was presented at the Warsaw conference. This depended principally on the lifetime-mass tag used here, but also included other b-tags and tags designed to select charm and light quark events in a multivariate approach. The preliminary result of that analysis was:

$$R_b^{multivariate} = (21.61 \pm 0.09(stat.) \pm 0.11(syst.))\,\%\,.$$

This is highly correlated to the result of the single-tag analysis presented here, so that only one could be used in calculating the world average measured value of R_b. The more precise multivariate analysis was chosen for this. The measurements and the resulting average R_b are shown in Figure 8.1 along with the result of the analysis presented here. There is reasonable agreement between the updated measurement and the Standard Model prediction — the 3.1σ discrepancy reported at the 1995 summer conferences has been reduced to 1.8σ.

When the world average value of R_b is combined with other precision electroweak data from LEP and SLD, a fit can be made to predict the top quark mass [50]. The resulting value is $m_t = 177^{+7+17}_{-8-19}\,\mathrm{GeV}$. Here, the central values and the first errors quoted assume a Higgs mass of 300 GeV and the second errors correspond to the change in the central value as the Higgs mass is varied within the interval $60\,\mathrm{GeV} < m_H < 1000\,\mathrm{GeV}$. This prediction for the mass of the top quark can then be compared to the direct measurement from CDF and D0 [49] of $m_t = 175 \pm 6\,\mathrm{GeV}$. The good agreement between the two is further evidence in support of the Standard Model.

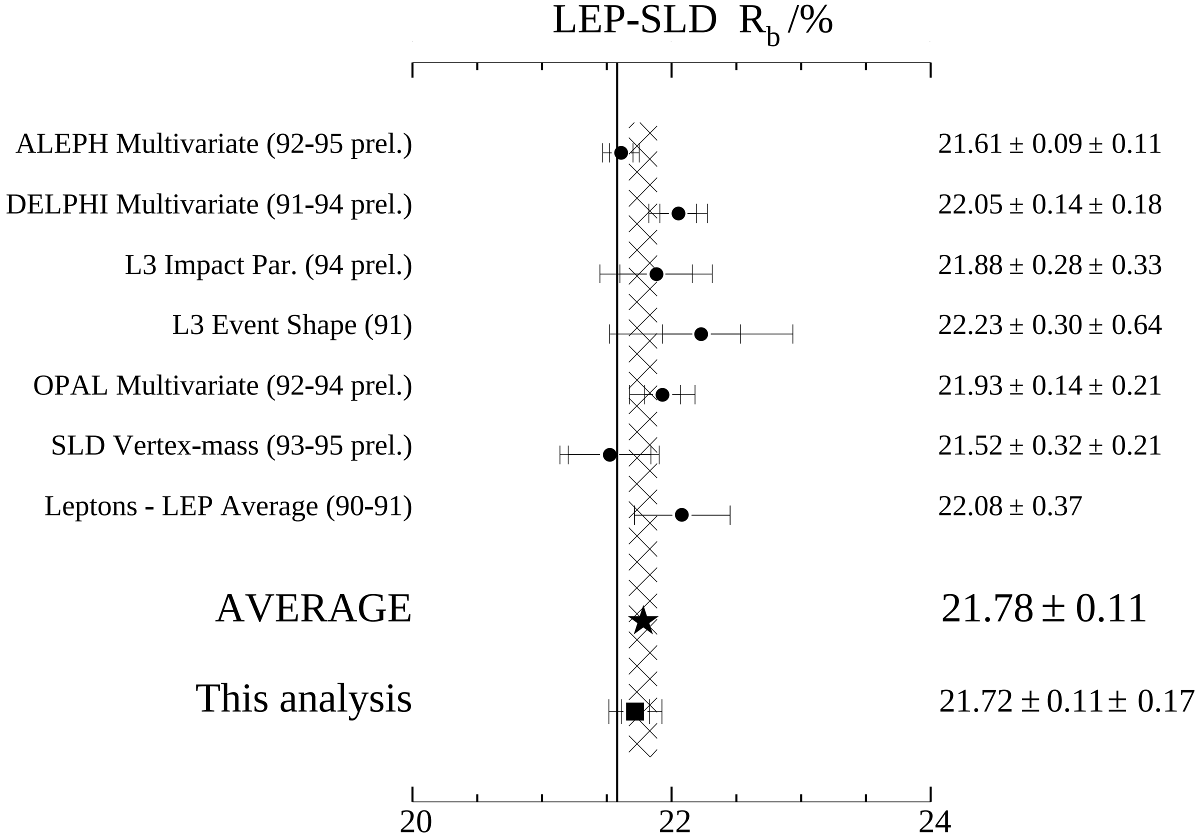

Figure 8.1: *World average value of R_b at the time of the ICHEP'96 conference in Warsaw, including some preliminary measurements. The world average is marked by a star and the shaded area shows the region within one standard deviation of the average. The vertical line indicates the Standard Model prediction. Where two errors are given, the first is statistical and the second systematic. R_c has been fixed to the Standard Model value.*

Bibliography

[1] D.G. Charlton, *Measurements of R_b using Lifetime Tags*, Talk given at the EPS-HEP-95 conference, Brussels, 1995

[2] A. Olchievski, *Precision Tests of the Standard Model*, Talk given at the EPS-HEP-95 conference, Brussels, 1995

[3] ALEPH Coll., *A Measurement of R_b using a Lifetime-Mass Tag*, Paper submitted to the ICHEP'96 conference, Warsaw, pa10-014

[4] ALEPH Coll., *A Measurement of R_b using Mutually Exclusive Tags*, Paper submitted to the ICHEP'96 conference, Warsaw, pa10-015

[5] I.J.R. Aitchison, A.J.G. Hey, *Gauge Theories in Particle Physics*, pub. Adam Hilger

[6] F. Halzen, A.D. Martin, *Quarks and Leptons*, pub. Wiley

[7] D. Griffiths, *Introduction to Elementary Particles*, pub. Wiley

[8] A. Pich, *The Standard Model of Electroweak Interactions*, Lectures presented at the XXII International Winter meeting on Fundamental Physics, Jaca, 1994, FTUV/94-62, hep-ph/9412274

[9] Particle Data Group, R.M. Barnett *et al.*, Phys. Rev. **D54** (1996) 1

[10] G. Altarelli *et al., Z Physics at LEP I, Vol.1: Standard Physics*, CERN 89-08

[11] T. Sjöstrand, Computer Physics Commun. **39** (1986) 347

[12] T. Sjöstrand, M. Bengtsson, Computer Physics Commun. **43** (1987) 435

[13] C. Peterson *et al.*, Phys. Rev. **D27** (1983) 105

[14] J. Ellis, *The Very Early Universe and Particle Physics*, Lectures presented at the Les Houches Summer School, CERN-TH 7083/93

[15] M. Drees, S.P. Martin, *Implications of SUSY Model Building*, Report of Subgroup 2 of the DPF Working Group on 'Electroweak symmetry breaking and beyond the Standard Model', MAD-PH-879 (1995), hep-ph/9504324

[16] ALEPH Coll., D. Buskulic *et al., Mass Limit for the Standard Model Higgs Boson with the full LEP I ALEPH data sample*, CERN-PPE/96-079, submitted to Phys. Lett.

[17] M. Martinez, *Precision Tests of the Standard Model*, Lectures given at NATO Advanced Study Institute, Cargese, 1994, IFAE-UAB-95-01

[18] X. Wang *et al.*, Phys. Rev. **D52** (1995) 4116

[19] J.D. Wells *et al.*, Phys. Lett. **B338** (1994) 219

[20] J. Ellis *et al., Supersymmetry and Rb in the light of LEP 1.5*, CERN-TH/95-314, hep-ph/9512288

[21] S. Myers, E. Picasso, Contemporary Physics **31** (1990) 387

[22] ALEPH Coll., *The ALEPH Handbook 1989*, ALEPH 89-077

[23] ALEPH Coll., D. Decamp *et al.*, Nucl. Instr. Meth. **A294** (1990) 121

[24] ALEPH Coll., D. Buskulic *et al.*, Nucl. Instr. Meth. **A360** (1995) 481

[25] ALEPH Coll., D. Buskulic *et al.*, Z. Phys **C55** (1992) 209

[26] J.E. Campagne, R. Zitoun, Z. Phys **C43** (1989) 469

[27] ALEPH Coll., D. Buskulic *et al.*, Z. Phys **C62** (1994) 179

[28] R. Brun *et al., GEANT3*, CERN-DD/EE/84-1 (1987)

[29] ALEPH Coll., *Proposal for a new Vertex Detector for ALEPH*, CERN/LEPC 93-8

[30] P. Coyle. *et al., Test Beam Results from Prototypes for the Upgraded ALEPH Vertex Detector*, Talk presented at the 6th Pisa meeting on Advanced Detectors, Isola d'Elba, 1994, CERN-PPE/94-153

[31] ALEPH Coll., D. Decamp *et al.*, Z. Phys **C 53** (1992) 1

[32] ALEPH. Coll., D. Buskulic *et al.*, Z. Phys. **C60** (1993) 71

[33] ALEPH Coll., D. Buskulic *et al.*, Phys. Lett. **B313** (1993) 549

[34] OPAL Coll., R. Akers *et al.*, Z. Phys. **C65** (1995) 17

[35] JADE Coll., S. Bethke *et al.*, Phys. Lett. **B213** (1988) 235

[36] ALEPH Coll., D. Buskulic *et al.*, Phys. Lett. **B313** (1993) 535

[37] The LEP experiments: ALEPH, DELPHI, L3 and OPAL *Combining Heavy Flavour Electroweak Measurements at LEP*, CERN-PPE/96-017, to be published in Nucl. Instr. Meth.

[38] OPAL Coll., G. Alexander *et al., A Study of Charm Hadron Production in* $Z \to c\bar{c}$ *and* $Z \to b\bar{b}$ *Decays at LEP*, CERN-PPE/96-051, submitted to Z. Phys.

[39] ALEPH Coll., D. Buskulic *et al.*, Z. Phys. **C69** (1996) 585

[40] DELPHI Coll., P. Abreu *et al.*, Z. Phys. **C59** (1993) 533

[41] The LEP Electroweak Working Group, *Presentation of LEP Electroweak Heavy Flavour Results for Summer 1996 Conferences*, LEPHF/96-01

[42] MARK-III Coll., D. Coffman *et al.*, Phys. Lett. **B263** (1991) 135

[43] OPAL Coll., R. Akers *et al.*, Phys. Lett. **B353** (1995) 595

[44] M.H. Seymour, Nucl. Phys. **B436** (1995) 163

[45] DELPHI Coll., P. Branchini, E. Graziani, *Measurement of Gluon Splitting Probability to Bottom Quark pairs* $g_{b\bar{b}}$ *in Hadronic* Z^0 *Decays*, Paper submitted to ICHEP'96 conference, Warsaw, pa01-035

[46] V. Sharma, *Recent Measurements of b Lifetimes*, Talk presented at 6th International Symposium on Heavy Flavours, Pisa, 1996

[47] OPAL Coll., R. Akers *et al.*, Z Phys. **C61** (1994) 209

[48] DELPHI Coll., P. Abreu *et al.*, Phys. Lett. **B347** (1995) 447

[49] A. Blondel, *Status of the Electroweak Interaction: Experimental Aspects*, Talk presented at the ICHEP'96 conference, Warsaw

[50] The LEP experiments: ALEPH, DELPHI, L3 and OPAL, *A Combination of Preliminary Electroweak Measurements and Constraints on the Standard Model*, Paper in preparation